THE UNIVERSITY OF CHICAGO

DIRECTED SELF-ASSEMBLY OF SYMMETRIC BLOCK COPOLYMER WITH DENSITY MULTIPLICATION FOR NANOPATTERNING APPLICATIONS

A DISSERTATION SUBMITTED TO
THE FACULTY OF THE INSTITUTE FOR MOLECULAR ENGINEERING
IN CANDIDACY FOR THE DEGREE OF
DOCTOR OF PHILOSOPHY

BY
XUANXUAN CHEN

CHICAGO, ILLINOIS
AUGUST 2017

Table of contents

List of tables

List of figures

Acknowledgements

To start, I am truly grateful for the endless love and support from my parents as well as the freedom they gave me all along the way I grew up.

Over my past six years of PhD life, I am very fortunate to meet many people who have inspired, accompanied, helped and supported me in different ways, and a simple “thank you” may fail to convey my gratitude.

First and foremost, I am really thankful for my advisor, Professor Paul Nealey, for guiding, enlightening and supporting me from the very first day I joined the group. He provides me great opportunities to collaborate with different people around the world. He never fails to encourage and enlighten me whenever I encounter bottlenecks in research. He always shares good things with us, not only polymer knowledges and presentation skills, but also life stories and yummy bakeries.

I would like to thank all the members in the Nealey group. Some of them I have never met, but taught me a lot about directed self-assembly with their published work. Some of them I worked daily with in lab, office and beamlines to go through all the ups and downs. A special thanks to Dr. Jiaxing Ren, my friend and peer student, for his help both in and outside of the lab over the past six years. Dr. Paulina Rincon is my best pal to work in the cleanroom, go for conferences and hang out for a beer in Europe. Future doctorates, Jiajing and Chun, are best companies to work in lab and go for shopping as well. Moshe is the most passionate “timer” to motivate my graduation. Dr. Chris Thode, Dr. Hyo Seon Suh, Dr. Shisheng Xiong, Dr. Lance Williamson and Dr. Robert Seidel taught me basics of block copolymers and the experimental details from back in Madison.

My dissertation work would not have been possible without all the collaborations. I would like to first thank Dr. Roel Gronheid and Dr. Paulina Rincon who have given me tremendous help and support during my 1.5 year in imec, Belgium – it was the smoothest transition from Chicago to

Leuven that I could ever expect, both in research work and personal life. Thank you for all the intellectual stimulations as well as the great time we spent together both in the fab and bar. Besides, I would like to thank all my collaborators from TOK, Japan for providing the materials and discussing on the projects, especially Takehito Seo and Tasuku Matsumiya. Boon Teik Chan from imec is greatly acknowledged for helping with the etching processes in my work. Prior to the time in Europe, a significant part of my PhD work applied X-ray scattering and was conducted on different synchrotron beamlines. I would also like to thank Professor. Manolis Doxastakis, Dr. Zhang Jiang, Dr. Daniel Sunday, Dr. Joe Kline, Dr. Wei Chen, Dr. Jin Wang and Dr. Joseph Strzalka for all the insightful discussions and great help with data collection.

The list extends to more names out of direct collaboration, including Abelardo, Daman, Grant and Alec from de Pablo group; Arjun, Jan, Hari, Marina, Nadia, and Carolien from DSA team in imec; Dries, Paul and Ainhoa from Tokyo Electron and many others.

Last but definitely not the least, I would like to thank my husband, as well as my best travel mate, for his constant support from Leuven to Chicago, and for all the wonderful memories we shared in past, which will be extended far into the future.

Abstract

Block copolymers (BCPs) are a group of fascinating materials that self-assemble into highly-uniform nanoscale structures. With precise control of interfacial properties on both interfaces, these nanostructures can be directed to form user-defined periodic patterns. The directed self-assembly (DSA) of BCPs offers a cost-effective solution to complement the conventional lithography with the capability of density multiplication and pattern rectification. This dissertation mainly focuses on the chemoepitaxial DSA of symmetric BCP into line patterns.

The chemoexpitaxy approach of DSA is developed by Liu and Nealey, in which the geometrical and chemical boundary conditions of the chemical pattern could be individually controlled. As the foundation to build up all the nanostructures, the guiding stripe pattern is fully characterized in both real and reciprocal spaces, and we locally and statistically analyze the trapezoid shape and line roughness. With optimized pattern conditions to minimize the interfacial energy, we investigate the DSA of poly(styrene-b-methyl methacrylate) (PS-b-PMMA) in the context of 3X density multiplication and reveal a different assembly mechanism in thicker film regime (> 2-3 L_0). Grain growth is decoupled from both interfaces at early assembly stage, and a faster defect annihilation process is visualized by X-ray scattering on the free surface compared to the film bulk.

With the current trend of device miniaturization, further evolution of DSA technology now faces challenges to realized sub-10 nm features. As the leading material for DSA applications for past decades, PS-b-PMMA can only form lamellas above ~12 nm in half pitch as limited by a low Flory-huggins interaction parameter, χ. We illustrate a simple strategy to scale down its intrinsic resolution limit by blending in selective ionic liquid additive to enhance the segregation strength in between blocks. By carefully controlling the volume fraction of ionic liquid additive, we maintain the favorable attributes of PS-b-PMMA and demonstrate successful sub-10 nm DSA with

thermal annealing and a free surface. More importantly, this PS-b-PMMA based high-χ material facilitates us to explore the fundamental and practical impacts of χ increase on interfacial width between polymer blocks, line edge roughness of DSA patterns as well as the kinetics of assembly.

The scope of this work is to gain fundamental understanding in the assembly mechanism of density multiplication based on the maturing platform of first generation material. Then the material research is extended to next-generation high-χ BCP. On the one hand, it provides a potential solution to access smaller dimension. On the other hand, it also brings about new challenges of DSA technology for current and future generations of low-cost, high-resolution nanopatterning applications.

Chapter 1

Introduction

1.1 Self-assembly of block copolymers

Block copolymers consist of two or more different homopolymer chains that are covalently bonded together. These chemically disparate components usually are not miscible with each other and go through macrophase separation when being mixed. Tethered by the covalent bonds, these polymer units in the block copolymer systems, instead, microphase separate into periodic microdomains with a length scale of 3 – 50 nm.[1] Block copolymers can be configured into various architectures based on the number of monomer types (e.g. diblock, triblock, or multi-block) and the molecular topology (e.g. linear, branched or star-shaped). The simplest one is linear diblock copolymer comprising two different homopolymers, which is the focus of this dissertation.

The phase behavior of diblock copolymer has been extensively studied over the past decades from both experimental and theoretical perspectives.[2–4] Governed by several key parameters including the Flory-Huggins interaction parameter χ, the total number of monomer units in the block copolymer N, and the volume fraction of each block f, the phase diagrams of AB diblock copolymer are presented in Figure 1, where theory[5] and experiment[6] reach good agreement. Note that the theoretically stable region of double-gyroid phase was further extended to higher $\chi N \sim 100$ by Cochran *et al.*[7] When χN exceeds a critical value of 10.5 for symmetric diblock copolymer ($f_A \approx f_B$), a wide range of morphologies such as spheres, cylinders, lamellas and gyroid can occur depending on the block ratio. The dimension of each morphology is a result of the interplay between a minimization of enthalpic free energy owing to A-B contacts and a maximization of conformational entropy of chains. When $\chi N < 10.5$, the order-disorder transition (ODT) occurs and no phase separation exists. Considering the effect of composition fluctuations at a finite molecular weight, an even larger critical value of $(\chi N)_{\mathrm{ODT}}$ is predicted by Fredrickson and Helfand.[8]

There are two efficient ways to facilitate high chain mobility and thus the self-assembled morphologies in block copolymer films - thermal annealing and solvent vapor annealing. In thermal annealing, the temperature is set between glass transition temperature of both building blocks and ODT temperature so that the chains are mobile and capable of achieving the equilibrium conformation upon time ($T_g < T < T_{\mathrm{ODT}}$). On the other hand, solvent vapor annealing is usually carried out at room temperature. It is the exposure to solvent environment, either selective[9] or non-selective[10], that enhances the polymer chain mobility and enables the reorganization of microdomains. While pros and cons exist for both processes, only thermal annealing is applied for all the studies hereafter.

1.2 Orientation control of block copolymer self-assembly

The orientation of block copolymer microdomains relative to the substrate in thin films is determined by the interfacial energy at the BCP/substrate interface,[11,12] the surface energies at the top surface,[13,14] film thickness,[15] and the morphology/architectures of the BCPs.[16,17] In the case of lamellar block copolymer, parallel wetting occurs when the free surface and bottom substrate are preferential to either component block. It is featureless at $t = \mathrm{n}\times L_0$ when the same block wets both interfaces (symmetric wetting), and $\mathrm{t} = (\mathrm{n}+0.5)\times L_0$ when different blocks wet both interfaces (asymmetric wetting), where t is film thickness, L_0 is the natural domain spacing to block copolymer and n is an integer. At other incommensurate film thicknesses, the parallel wetting becomes topographical and forms “hole” or “island” structures of $1L_0$ in height depending on the exact t value after annealing.[18–20] If either top surface or bottom substrate favors both blocks equally, the presence of one neutral and one preferential interface generates similar structures but of $0.5L_0$ topography.[21] Further investigation reveals that this $0.5L_0$ “hole” or “island” is thermodynamically stable only with the presence of perfectly neutrality of one interface and a slight deviation may lead to the 1 L_0 topography.[22] When both interfaces are perfectly or nearly neutral, as the chain conformation prefers parallel to the substrate to reduce the entropic cost,[23,24] the lamellar structures are perpendicularly aligned regardless of the quantization of film thickness in thin film regime.

Various approaches have been developed to obtain the vertical alignment of block copolymers, which is most desirable for their applications ranging from nanopatterning to membrane filtration. One approach is to apply external fields such as electric field[25] and solvent evaporation field.[26,27] Another approach is to balance the surface energy at the polymer-air interface, for example with the addition of low molecular weight surfactant[28] or surface active random copolymer.[29] Alternatively, the interfacial energies at the bottom interface are efficiently adjusted by surface modifications of the substrate, which could be achieved by self-assembled monolayers,[30,31] random copolymer brush or mat materials.[11,12,32,33] The use of random copolymer has been recognized as a simple and robust way to tune the interfacial interactions in between the substrate and the overlaying polymer film. In most cases, the random copolymer comprises the same components from the block copolymer of interest. Huang *et al.* also discussed other scenarios in which one or both components of the random and block copolymer are chemically distinct.[34] In most cases, a combination of these approaches is necessary to control both the surface and interfacial energy for achieving perpendicular through-film structures.[29,35,36]

1.3 Directed self-assembly (DSA) of block copolymers

Self-assembling block copolymers, when applied in combination with traditional optical lithography methods, have shown significant promise for the patterning of FinFET transistors,[37,38] bit-patterned media,[39,40] and contact holes[41,42] for integrated circuits. Long-range ordering and accurate placement control are required for block copolymer lithography. To provide long-range ordering, numerous methods have been proposed including shear alignment,[43] electric[25] and magnetic[44] fields. To further facilitate the placement accuracy, graphoepitaxy and chemoepitaxy are two foremost patterning schemes of block copolymer lithography for practical semiconductor device fabrication with pre-patterns defined by conventional lithography.

First introduced by Segalman *et al.*,[45] the concept of "graphoepitay" utilizes the topographical feature of the pre-pattern to guide the self-assembly of block copolymers into highly-ordered structures of various morphologies ranging from spheres,[46,47] cylinders[48,49] to lamellas.[50] The spatial control of microdomains has been systematically studied as a function of film thickness, interfacial interactions as well as the geometry of the topographical pattern.[50–52] With great potential to fabricate line-space patterns with enhanced density, graphoepitaxy faces other challenges such as loss of guiding patterns and issues of coating conformity. On the contrary, it offers a simple and attractive route to enable smaller dimension for contact hole patterning, which has attracted great research interests towards its integration with fabrication process in very large scale integrated (VLSI) circuits.[53–56]

Instead of the topographical confinement, chemical contrast of the pre-pattern is utilized in the chemoepitaxy method to guide the assembly by tuning the interfacial energy between the polymer and substrate. Nanoperiodic, heterogeneous surfaces, which are shallow grooves of alternating oxide and metal stripes, were first used by Rockford *et al.* to align the orientation of poly(styrene-b-methyl methacrylate) (PS-b-PMMA) lamellas in 1999.[57] Later in 2003, Kim et al. demonstrated the first defect-free epitaxial assembly of the same block copolymer on the line-space pattern fabricated from extreme-ultraviolet interference lithography (EUV-IL).[58] By alternating the chemical affinity of adjacent stripes on the chemical patterns to favor different blocks, the long-range ordering of the microdomains is greatly enhanced by the lateral control of domain registration. Apart from regular structures, Stoykovich *et al*. further demonstrated more complex pattern geometries such as bends, jogs, T-junctions and isolated features, using ternary blends of block copolymer and homopolymer.[59,60] The most significant breakthrough of the chemoepitaxy approach was the density multiplication of DSA that enables the resolution enhancement below the limit of conventional lithography. Dense arrays of sphere-,[61] cylinder-[62] and lamellae-forming[63] PS-b-PMMA were successfully assembled on sparse lithographic pattern with the pattern density of block copolymer lithography efficiently multiplied. It is noteworthy that the self-healing property of block copolymers also contributes to rectifying poorly-defined chemical patterns with significant line roughness,[64] patterning non-uniformity[61] and defects.[63]

With the above advantages of lateral ordering control, customized morphology, density multiplication and pattern rectification, chemical epitaxy method is used for DSA patterning in this dissertation based on the following process flow first proposed by Liu and Nealey *et al.* as schematized in Figure 1.2.[65] This Liu-Nealey (LiNe) process flow makes the following improvements: 1) a trim etch step is added to reduce the width of guiding stripes beyond the resolution limit of previous lithography step so that pattern geometry (e.g. pitch and width of guiding lines) is precisely controlled; 2) random copolymer brush is grafted onto the interspatial region in between adjacent guiding stripes to fine tune the chemical condition, and the ideal brush composition is identified as a function of density multiplication factor.[66] While Figure 1.2 only depicts the specific implementation of the process to assemble symmetric PS-b-PMMA lamellas, which is the system used in this dissertation, the fabrication method to produce chemically patterned substrates could be generalized for DSA of other morphologies[67] and block copolymer systems,[68–70] or other DSA approaches than thermal annealing, such as solvent vapor annealing.[10]

Successful implementation of DSA would require perfect, defect-free morphology and thus the optimal guiding pattern conditions, there has been some recent research progress in characterizing and understanding the geometry and chemistry of chemical patterns fabricated by LiNe flow using manufacturing tools.[71] Suh and Chen *et al.* provided a quantitatively analysis of the shape and line edge roughness of the guiding stripes using atomic force microscopy (AFM) and grazing-incidence small-angle X-ray scattering (GISAXS),[72] and detailed results and discussions are available in Chapter 2. Williamson and Seidel *et al.* further revealed the three-tone chemistry of the pattern instead of the simplified dual-tone model presented in Figure 1.2.[73]

1.4 DSA from lab to fab

The idea of using self-assembling block copolymers as patterning templates was first proposed in 1995,[74] while the first demonstration of “block copolymer lithography” that transfers patterns down to underlying substrates was introduced by Park *et al.* in 1997.[75] The past two decades witnessed not only a burgeoning growth in publications to build up the fundamental understanding of polymer self-assembly, but also considerable research efforts to demonstrate its capability in the fabrication of various functional devices. Black *et al.* fabricated shallow-trench-array capacitor with > 300% increase in the accumulation capacitance compared to planar devices by enhancing the surface area using block copolymer templates.[76] Guarini *et al.* precisely defined the nanocrystal size, density and uniformity via polymer self-assembly in the fabrication of nanocrystal flash memory that allows lower voltage operations.[77] Block copolymer materials were also reported to generate air-gap structures in inter-layer dielectric (ILD) materials and thus to reduce the delay time in interconnections.[78] While self-assembly alone is sufficient for the above applications in semiconductor microelectronics, directed self-assembly (DSA) provides a lithography alternative for which accurate pattern registration and long-range ordering are required.

The critical leap for the DSA technology from lab to fab is enabled by its integration with 193 immersion lithography for resolution enhancement.[79,80] This high volume manufacturing (HVM) compatibility provides a unprecedented platform to determine whether DSA is a viable solution for next-generation patterning. Based on the survey results of DSA symposium in 2015 and 2016, graphoepitaxy single hole shrink and chemoepitaxy line-space patterning are considered the top two DSA processes that would be most likely applied in IC manufacturing. Here we mainly focus on the latter case of chemoepitaxy line-space patterning, for which many research explorations have been made to address such key challenges as defectivity, integration, pattern fidelity and line roughness. Rincon *et al*. systematically analyzed the origin of defects and optimized the materials and processes for defectivity reduction.[81] Liu and Sayan *et al*. demonstrated the integration of chemoepitaxy DSA to the fin patterning with excellent control of pitch and CD uniformity, as well as flexibility in active areas.[82,83] Singh *et al.* incorporated metal into DSA lines based on sequential infiltration synthesis (SIS) to enhance etch contrast and reduce line-edge roughness for the pattern transfer.[84] Apart from the above experimental progresses, more effort is anticipated meet other technology needs, for example, dimension shrinking, in-line metrology and yield in order to qualify the next transition of DSA from pilot to production line.

1.5 High-χ block copolymers

Over the past few decades, PS-b-PMMA has been the prototype of first generation DSA material owing to numerous reasons: the surface energies of the two building blocks are close at the temperature of annealing,[11] random copolymer brush or mat materials are available and easily pattern for control of the interfacial interactions, and selective removal of PMMA domains via dry or wet processing offers ease of pattern transfer.[39,85] While the polymer physics governing the thermodynamics and kinetics of DSA process is well understood through extensive studies of PS-b-PMMA, unfortunately, the relatively low segregation strength between the PS and PMMA blocks as characterized by the Flory-Huggins interaction parameter, χ (~0.036[86] at 200 °C), restricts the minimum feature size of PS-b-PMMA, which no longer satisfies the competition of resolution scaling with other technologies such as multiple patterning and extreme ultraviolet (EUV) lithography. As predicted by strong segregation theory and empirically measured, the domain spacing of lamellar block copolymers scales as $L_0 \propto \chi^{1/6}N^{2/3}$, where N is the degree of polymerization. Although diminishing χ or N may therefore be used to reduce the feature sizes accessible to BCPs, a side-effect is that the driving force for phase separation is concomitantly reduced. From mean-field theory, the phase separation of symmetric diblock copolymers requires the product χN to exceed 10.495,[3] and, in practice, systems with even higher χN are required to avoid fluctuation effects[8] and issues in pattern transfer[87] near the order-to-disorder transition (ODT).

High-χ and low-N BCP materials provide an opportunity to achieve smaller feature sizes than that accessible to PS-b-PMMA.[88] Examples of high-χ BCPs that have been developed include PS-b-PLA, PS-b-PDMS and PTMSS-b-PMOST which have χ values of 0.095,[89] 0.181,[90] and 0.398[91] at 200 °C, respectively. As most of such materials have considerably dissimilar surface energies, the orientation control becomes more challenging since the block of lower surface energy easily segregates to the free air surface. Various approaches have been developed to circumvent this problem and align high-χ BCPs perpendicularly to the substrate. The first one is to introduce a neutral top layer to balance the interfacial energy difference, which could be accomplished by spin-coating,[36] printing,[14] or chemical vapor deposition.[69] An alternative to apply top coat without introducing extra steps is to incorporate surface active additive into high-χ BCP that segregates to the top of the film and balance the surface tensions while maintaining the strong segregation strength.[92,93] The third approach that may involve more processing changes is solvent vapor annealing (SVA), in which the exposure to adequate solvent balances the surface energy and maintains the chemical recognition of underlaying template.[35,94–96] The last approach is to molecularly engineer high-χ materials with less extreme differences in surface energies and that will be compatible with thermal annealing at a free surface. Pairs of monomers are designed to have high χ as well as moderate difference in surface energies.[68,97,98] Alternatively, other high-χ materials have tunable surface and interfacial energies with random copolymer as one component block.[99–101]

In Chapter 3 and 4 of this dissertation, we proposed a conceptually different role of ionic liquid as an additive to enhance the phase segregation of PS-b-PMMA, and studied the blends of PS-b-PMMA and ionic liquid as a high-χ drop-in replacement of PS-b-PMMA. While HVM-compatible research is available in several DSA consortiums based on the traditional PS-b-PMMA material over the world,[102] a majority of research work on high-χ BCPs is still in lab environment. Here we endeavored to apply material research to production practice by demonstrating the sub-10 nm DSA of PS-b-PMMA/IL blends at 300 mm-wafer scale on the pilot line in imec, Belgium, and further investigated the impact of ionic liquid additive and thus the χ increase on the material properties and DSA process.

1.6 Thesis outline

Chapter 2 presents a detailed analysis of the guiding stripe gratings, which define the geometry of the chemical pattern fabricated by the LiNe flow. Grazing-incidence small-angle X-ray scattering (GISAXS) and atomic force microscopy (AFM) are used to quantitatively characterize the trapezoid shape and line-edge roughness of the guiding stripe pattern, providing a foundation for further studies on the three-dimensional structures in directed self-assembly processes.

In the context of 3X density multiplication, Chapter 3 investigates the grain growth and defect annihilation in the DSA process over a wide range of film thickness. We observe a critical film thickness over which the rotational GISAXS measurement qualitatively and quantitatively reveals faster defect annihilation on the free surface than in the film bulk.

In order to scale down the intrinsic resolution limit of the first generation block copolymer material, ionic liquid is introduced as an additive to enhance the segregation strength of the block copolymer while maintaining its favorable attributes. In Chapter 4, we demonstrate successful sub-10 nm DSA of the blends of block copolymer and ionic liquid based on the same chemoepitaxy method that is capable with thermal annealing and free of top coats. The blending system is proposed as a drop-in replacement of the first generation material to access smaller features in wafer-scale DSA patterning. Chapter 5 further discusses the impact of ionic liquid additive and the increase in segregation strength of the block copolymer on its interfacial width, post-etch line edge roughness and assembly kinetics from both the fundamental and practical perspectives. Since the LiNe flow adopted in this thesis has been successfully integrated with 193 immersion lithography and implemented with manufacturing tools, the content in Chapter 4 and 5 was conducted in HVM-compatible research environment on imec’s 300 mm scale production line in Belgium.

1.7 References

(1) Bates, F. S.; Fredrickson, G. H. *Annu. Rev. Phys. Chern* **1990**, *41*, 525–557.

(2) Helfand, E.; Tagami, Y. *J. Chem. Phys.* **1972**, *56* (7), 3592–3601.

(3) Leibler, L. *Macromolecules* **1980**, *13* (6), 1602–1617.

(4) Bates, F. S.; Fredrickson, G. H. *Annu. Rev. Phys. Chem* **1990**, *41*, 525–557.

(5) Matsen, M. W.; Schick, M. *Phys. Rev. Lett.* **1994**, *72* (16), 2660–2663.

(6) Khandpur, A. K.; Foerster, S.; Bates, F. S.; Hamley, I. W.; Ryan, A. J.; Bras, W.; Almdal, K.; Mortensen, K. *Macromolecules* **1995**, *28* (26), 8796–8806.

(7) Cochran, E. W.; Garcia-Cervera, C. J.; Fredrickson, G. H. *Macromolecules* **2006**, *39* (7), 2449–2451.

(8) Fredrickson, G. H.; Helfand, E. *J. Chem. Phys.* **1987**, *87* (1), 697–705.

(9) Wan, L.; Ji, S.; Liu, C.-C.; Craig, G. S. W.; Nealey, P. F. *Soft Matter* **2016**, *12* (11), 2914–2922.

(10) Xiong, S.; Wan, L.; Ishida, Y.; Chapuis, Y. A.; Craig, G. S. W.; Ruiz, R.; Nealey, P. F. *ACS Nano* **2016**, *10* (8), 7855–7865.

(11) Mansky, P.; Liu, Y.; Huang, E.; Russell, T. P.; Hawker, C. *Science* . **1997**, *275*, 1458–1460.

(12) Han, E.; Stuen, K. O.; La, Y. H.; Nealey, P. F.; Gopalan, P. *Macromolecules* **2008**, *41* (23), 9090–9097.

(13) Bates, C. M.; Seshimo, T.; Maher, M. J.; Durand, W. J.; Cushen, J. D.; Dean, L. M.; Blachut, G.; Ellison, C. J.; Willson, C. G. *Science* **2012**, *338* (6108), 775–779.

(14) Yoshida, H.; Suh, H. S.; Ramírez-hernández, A.; Lee, J. I.; Aida, K. **2013**, *C*, 55–58.

(15) Suh, H. S.; Kang, H.; Nealey, P. F.; Char, K. *Macrmolecules* **2010**, *43*, 4744–4751.

(16) Vu, T.; Mahadevapuram, N.; Perera, G. M.; Stein, G. E. *Macromolecules* **2011**, *44* (15), 6121–6127.

(17) Lo, T.-Y.; Dehghan, A.; Georgopanos, P.; Avgeropoulos, A.; Shi, A.-C.; Ho, R.-M. *Macromolecules* **2016**, *49* (2), 624–633.

(18) Coulon, G.; Russell, T. P.; Deline, V. R.; Green, P. F. *Macromolecules* **1989**, *22* (6), 2581–2589.

(19) Russell, T. P.; Coulon, G.; Deline, V. R.; Miller, D. C. *Macromolecules* **1989**, *22* (12), 4600–4606.

(20) Coulon, G.; Ausserre, D.; Russell, T. P. *J. Phys.* **1990**, *51* (8), 777–786.

(21) Kim, S.; Bates, C. M.; Thio, A.; Cushen, J. D.; Ellison, C. J.; Willson, C. G.; Bates, F. S. *ACS Nano* **2013**, *7* (11), 9905–9919.

(22) Maher, M. J.; Self, J. L.; Stasiak, P.; Blachut, G.; Ellison, C. J.; Matsen, M. W.; Bates, C. M.; Willson, C. G. *ACS Nano* **2016**, *10* (11), 10152–10160.

(23) Matsushita, Y.; Mori, K.; Mogi, Y.; Saguchi, R.; Noda, I.; Nagasawalc, M.; Chang, T.; Glinka, C. J.; Han, C. C. *Macromolecules* **1990**, *23*, 4317–4321.

(24) Pickett, G. T.; Witten, T. A.; Nagel, S. R. *Macromolecules* **1993**, *26*, 3194–3199.

(25) Morkved, T. L.; Lu, M.; Urbas, A. M.; Ehrichs, E. E.; Jaeger, H. M.; Mansky, P.; Russell, T. P. *Science* . **1996**, *273* (5277), 931–933.

(26) Sidorenko, A.; Tokarev, I.; Minko, S.; Stamm, M. *J. Am. Chem. Soc.* **2003**, *125* (40), 12211–12216.

(27) Kim, S. H.; Misner, M. J.; Xu, T.; Kimura, M.; Russell, T. P. *Adv. Mater.* **2004**, *16* (3), 226–231.

(28) Jeong, B.; Son, G.; Bulliard, X.; Kang, H.; Nealey, P. F.; Char, K. *Adv. Mater.* **2008**, *20*, 3643–3648.

(29) Huang, E.; Russell, T. P.; Harrison, C.; Chaikin, P. M.; Register, R. A.; Hawker, C. J.; Mays, J. *Macromolecules* **1998**, *31* (22), 7641–7650.

(30) Peters, R. D.; Yang, X. M.; Kim, T. K.; Nealey, P. F. *Langmuir* **2000**, *16* (24), 9620–9626.

(31) Albert, J. N. L.; Baney, M. J.; Stafford, C. M.; Kelly, J. Y.; Epps, T. H. *ACS Nano* **2009**.

(32) Ryu, D. Y.; Shin, K.; Drockenmuller, E.; Hawker, C. J.; Russel, T. P. *Science* . **2005**, *308* (5719), 236–238.

(33) In, I.; La, Y.-H.; Park, S.-M.; Nealey, P. F.; Gopalan, P. *Langmuir* **2006**, *22* (18), 7855–7860.

(34) Huang, E.; Pruzinsky, S.; Russell, T. P.; Mays, J.; Hawker, C. J. *Macromolecules* **1999**, *32* (16), 5299–5303.

(35) Gotrik, K. W.; Hannon, A. F.; Son, J. G.; Keller, B.; Alexander-Katz, A.; Ross, C. A. *ACS Nano* **2012**, *6* (9), 8052–8059.

(36) Bates, C. M.; Seshimo, T.; Maher, M. J.; Durand, W. J.; Cushen, J. D.; Dean, L. M.; Blachut, G.; Ellison, C. J.; Willson, C. G. *Science* . **2012**, *338* (6108), 775–779.

(37) Tsai, H.; Pitera, J. W.; Miyazoe, H.; Bangsaruntip, S.; Engelmann, S. U.; Liu, C.-C.; Cheng, J. Y.; Bucchignano, J. J.; Klaus, D. P.; Joseph, E. A.; Sanders, D. P.; Colburn, M. E.; Guillorn, M. A. *ACS Nano* **2014**, *8* (5), 5227–5232.

(38) Tsai, H.; Miyazoe, H.; Vora, A.; Magbitang, T.; Arellano, N.; Liu, C.-C.; Maher, M. J.; Durand, W. J.; Dawes, S. J.; Bucchignano, J. J.; Gignac, L.; Sanders, D. P.; Joseph, E. A.; Colburn, M. E.; Willson, C. G.; Ellison, C. J.; Guillorn, M. A. In *Proc. SPIE*; 2016; p 977910.

(39) Ruiz, R.; Dobisz, E.; Albrecht, T. R. *ACS Nano* **2011**, *5* (1), 79–84.

(40) Albrecht, T. R.; Bedau, D.; Dobisz, E.; Gao, H.; Grobis, M.; Hellwig, O.; Kercher, D.; Lille, J.; Marinero, E.; Patel, K.; Ruiz, R.; Schabes, M. E.; Wan, L.; Weller, D. *IEEE Trans. Magn.* **2013**, *49* (2), 773–778.

(41) Bao, X.; Yi, H.; Bencher, C.; Chang, L.; Dai, H.; Chen, Y.; Chen, P. J.; Wong, H. P. In *Electron Devices Meeting (IEDM)*; 2011; p 7.7.1-7.7.4.

(42) Yi, H.; Bao, X. Y.; Zhang, J.; Bencher, C.; Chang, L. W.; Chen, X.; Tiberio, R.; Conway, J.; Dai, H.; Chen, Y.; Mitra, S.; Wong, H. S. P. *Adv. Mater.* **2012**, *24* (23), 3107–3114.

(43) Angelescu, D. E.; Waller, J. H.; Adamson, D. H.; Deshpande, P.; Chou, S. Y.; Register, R. A.; Chaikin, P. M. *Adv. Mater.* **2004**, *16* (19), 1736–1740.

(44) Gopinadhan, M.; Majewski, P. W.; Choo, Y.; Osuji, C. O. **2013**, *78301* (February), 1–5.

(45) Segalman, R. A.; Yokoyama, H.; Kramer, E. J. *Adv. Mater.* **2001**, *13* (15), 1152–1155.

(46) Cheng, J. Y.; Ross, C. A.; Thomas, E. L.; Smith, H. I.; Vancso, G. J. *Appl. Phys. Lett.* **2002**, *4* (19), 3657–3659.

(47) Cheng, J. Y.; Mayes, A. M.; Ross, C. A. *Nat. Mater.* **2004**, *3* (11), 823–828.

(48) Sundrani, D.; Darling, S. B.; Sibener, S. J. *Nano Lett.* **2004**, *4* (2), 273–276.

(49) Black, C. T.; Bezencenet, O. *IEEE Trans. Nanotechnol.* **2004**, *3* (3), 412–415.

(50) Han, E.; Kang, H.; Liu, C. C.; Nealey, P. F.; Gopalan, P. *Adv. Mater.* **2010**, *22* (38), 4325–4329.

(51) Park, S.-M.; Stoykovich, M. P.; Ruiz, R.; Zhang, Y.; Black, C. T.; Nealey, P. F. *Adv. Mater.* **2007**, *19* (4), 607–611.

(52) Ruiz, R.; Ruiz, N.; Zhang, Y.; Sandstrom, R. L.; Black, C. T. *Adv. Mater.* **2007**, *19* (16), 2157–2162.

(53) Li, W.-K.; Yang, S. *J. Vac. Sci. Technol. B Microelectron. Nanom. Struct.* **2007**, *25* (6), 1982.

(54) Yuriko Seino; Yonemitsu, H.; Sato, H.; Kanno, M.; Kato, H.; Kobayashi, K.; Kawanishi, A.; Azuma, T.; Muramatsu, M.; Nagahara, S.; Kitano, T.; Toshima, T. *J. Micro/Nanolithography, MEMS, MOEMS* **2013**, *12* (3), 33011.

(55) Doise, J.; Chan, B. T.; Hori, M.; Gronheid, R. In *SPIE Advanced Lithography*; 2017; Vol. 101460, p 101460R.

(56) Chi, C.; Liu, C.-C.; Meli, L.; Guo, J.; Parnell, D.; Mignot, Y.; Schmidt, K.; Sanchez, M.; Farrell, R.; Singh, L.; Furukawa, T.; Lai, K.; Xu, Y.; Sanders, D.; Hetzer, D.; Metz, A.; Burns, S.; Felix, N.; Arnold, J.; Corliss, D. In *SPIE Advanced Lithography*; 2017; Vol. 10146, p 101460Q.

(57) Rockford, L.; Liu, Y.; Mansky, P.; Russell, T. P.; Yoon, M.; Mochrie, S. G. J. *Phys. Rev. Lett.* **1999**, *82* (12), 2602–2605.

(58) Kim, S. O.; Solak, H. H.; Stoykovich, M. P.; Ferrier, N. J.; Pablo, J. J. De; Nealey, P. F. *Nature* **2003**, *424*, 411–414.

(59) Stoykovich, M. P.; Müller, M.; Kim, S. O.; Solak, H. H.; Erik, W.; Pablo, J. J. De; Nealey, P. F. *Science* . **2012**, *308* (5727), 1442–1446.

(60) Stoykovich, M. P.; Kang, H.; Daoulas, K. C.; Liu, G.; Liu, C. C.; De Pablo, J. J.; Müller, M.; Nealey, P. F. *ACS Nano* **2007**, *1* (3), 168–175.

(61) Ruiz, R.; Kang, H.; Detcheverry, F. a; Dobisz, E.; Kercher, D. S.; Albrecht, T. R.; de Pablo, J. J.; Nealey, P. F. *Science* . **2008**, *321* (5891), 936–939.

(62) Tada, Y.; Akasaka, S.; Yoshida, H.; Hasegawa, H.; Dobisz, E.; Kercher, D.; Takenaka, M. *Macromolecules* **2008**, *41* (23), 9267–9276.

(63) Cheng, J. K.; Rettner, C. T.; Sanders, D. P.; Kim, H. C.; Hinsberg, W. D. *Adv. Mater.* **2008**, *20* (16), 3155–3158.

(64) Stoykovich, M. P.; Daoulas, K. C.; Müller, M.; Kang, H.; De Pablo, J. J.; Nealey, P. F. *Macromolecules* **2010**, *43* (5), 2334–2342.

(65) Liu, C.; Han, E.; Onses, M. S.; Thode, C. J.; Ji, S.; Gopalan, P.; Nealey, P. F. **2011**, 1876–1885.

(66) Liu, C.; Ramirez-Hernandez, A.; Han, E.; Craig, G. S. W.; Tada, Y.; Yoshida, H.; Kang, H.; Ji, S.; Gopalan, P.; de Pablo, J. J.; Nealey, P. F. *Macrmolecules* **2013**, *46*, 1415–1424.

(67) Singh, A.; Nam, J.; Lee, J.; Chan, B. T.; Wu, H.; Yin, J.; Cao, Y.; Gronheid, R. In *SPIE Advanced Lithography*; 2016; Vol. 9777, p 97770P.

(68) Yang, G.-W.; Wu, G.-P.; Chen, X.; Xiong, S.; Arges, C. G.; Ji, S.; Nealey, P. F.; Lu, X.-B.; Darensbourg, D. J.; Xu, Z.-K. *Nano Lett.* **2017**, *17* (2), 1233–1239.

(69) Suh, H. S.; Kim, D. H.; Moni, P.; Xiong, S.; Ocola, L. E.; Zaluzec, N. J.; Gleason, K. K.; Nealey, P. F. *Nat. Nanotechnol.* **2017**.

(70) Kim, S.; Nealey, P. F.; Bates, F. S. *Nano Lett.* **2013**, 12–16.

(71) Delgadillo, P. A. R.; Gronheid, R.; Thode, C. J.; Wu, H.; Cao, Y.; Neisser, M.; Somervell, M.; Nafus, K.; Nealey, P. F. *J. Micro/Nanolithography, MEMS, MOEMS* **2012**, *11* (3), 31302.

(72) Suh, H. S.; Chen, X.; Rincon-Delgadillo, P. A.; Jiang, Z.; Strzalka, J.; Wang, J.; Chen, W.; Gronheid, R.; De Pablo, J. J.; Ferrier, N.; Doxastakis, M.; Nealey, P. F. *J. Appl. Crystallogr.* **2016**, *49*, 823–834.

(73) Williamson, L. D.; Seidel, R. N.; Chen, X.; Suh, H. S.; Rincon Delgadillo, P.; Gronheid, R.; Nealey, P. F. *ACS Appl. Mater. Interfaces* **2016**, *8* (4), 2704–2712.

(74) Mansky, P.; Chaikin, P.; Thomas, E. L. *J. Mater. Sci.* **1995**, *30*.

(75) Park, M.; Harrison, C.; Chaikin, P. M.; Register, R. A.; Adamson, D. H. *Science* . **1997**, *276* (5317), 1401–1404.

(76) Black, C. T.; Guarini, K. W.; Zhang, Y.; Kim, H.; Benedict, J.; Sikorski, E.; Babich, I. V; Milkove, K. R. *IEEE Electron Device Lett.* **2004**, *25* (9), 622–624.

(77) Guarini, K. W.; Black, C. T.; Zhang, Y.; Babich, I. V.; Sikorski, E. M.; Gignac, L. M. *IEEE Int. Electron Devices Meet. 2003* **2003**, *0* (c), 22.2.1-22.2.4.

(78) Ponoth, S.; Horak, D.; Nitta, S.; Colburn, M.; Breyta, G.; Huang, E.; Sucharitaves, J.; Landis, H.; A.Lisi; Liu, X.; Vo, T.; Johnson, R.; Li, W.; Purushothaman, S.; Cohen, S.; Hu, C.-K.; Kim, H.-C.; Clevenger, L.; Fuller, N.; Nogami, T.; Spooner, T.; Edelstein, D. In *214th ECS Meetings Abstract*; 2008.

(79) Cheng, J. Y.; Sanders, D. P.; Truong, H. D.; Harrer, S.; Friz, A.; Holmes, S.; Colburn, M.; Hinsberg, W. D. *ACS Nano* **2010**, *4* (8), 4815–4823.

(80) Liu, C.-C.; Nealey, P. F.; Raub, A. K.; Hakeem, P. J.; Brueck, S. R. J.; Han, E.; Gopalan, P. *J. Vac. Sci. Technol. B, Nanotechnol. Microelectron. Mater. Process. Meas. Phenom.* **2010**, *28* (6), C6B30-C6B34.

(81) Delgadillo, P. R.; Suri, M.; Durant, S.; Cross, A.; Nagaswami, V. R.; Heuvel, D. Van Den; Gronheid, R.; Nealey, P. *J. Micro/Nanolithography, MEMS, MOEMS* **2013**, *8680*, 86800L.

(82) Liu, C.-C.; Estrada-Raygoza, C.; He, H.; Cicoria, M.; Rastogi, V.; Mohanty, N.; Tsai, H.; Schepis, A.; Lai, K.; Chao, R.; Liu, D.; Guillorn, M.; Cantone, J.; Mignot, S.; Kim, R.-H.; Cheng, J.; Tjio, M.; Ko, A.; Hetzer, D.; Somervell, M.; Colburn, M. In *SPIE Advanced Lithography*; 2014; Vol. 9049, p 904909.

(83) Sayan, S.; Chan, B. T.; Marzook, T.; Vandenbroeck, N.; Sanchez, E. A.; Gronheid, R.; Singh, A.; Delgadillo, P. R. In *SPIE Advanced Lithography*; 2015; Vol. 9425, p 94250R.

(84) Singh, A.; Knaepen, W.; Sayan, S.; el Otell, Z.; Chan, B. T.; Maes, J. W.; Gronheid, R. In *SPIE Advanced Lithography*; 2015; Vol. 9425, p 94250N.

(85) He, C.; Stoykovich, M. P. *Adv. Funct. Mater.* **2014**, *24* (45), 7078–7084.

(86) Russell, T.; Jr, R. H.; Seeger, P. *Macromolecules* **1990**, *23*, 890–893.

(87) Wan, L.; Ruiz, R.; Gao, H.; Patel, K. C.; Albrecht, T. R.; Yin, J.; Kim, J.; Cao, Y.; Lin, G. **2012**, *20* (3), 5–6.

(88) Sinturel, C.; Bates, F. S.; Hillmyer, M. A. *ACS Macro Lett.* **2015**, *4* (9), 1044–1050.

(89) Andrew S. Zalusky; Roberto Olayo-Valles, †; Johanna H. Wolf, A.; Hillmyer*, M. A. *J. Am. Chem. Soc.* **2002**, *124*, 12761–12773.

(90) Eric W. Cochran; David C. Morse, A.; Bates*, F. S. *Macrmolecules* **2003**, *36*, 782–792.

(91) Cushen, J. D.; Bates, C. M.; Rausch, E. L.; Dean, L. M.; Zhou, S. X.; Willson, C. G.; Ellison, C. J. *Macromolecules* **2012**, *45* (21), 8722–8728.

(92) Zhang, J.; Clark, M. B.; Wu, C.; Li, M.; Trefonas, P.; Hustad, P. D. *Nano Lett.* **2016**, *16* (1), 728–735.

(93) Vora, A.; Schmidt, K.; Alva, G.; Arellano, N.; Magbitang, T.; Chunder, A.; Thompson, L. E.; Lofano, E.; Pitera, J. W.; Cheng, J. Y.; Sanders, D. P. *ACS Appl. Mater. Interfaces* **2016**, *8* (43), 29808–29817.

(94) Kim, S. H.; Misner, M. J.; Xu, T.; Kimura, M.; Russell, T. P. *Adv. Mater.* **2004**, *16* (3), 226–231.

(95) Park, S.; Lee, D. H.; Xu, J.; Kim, B.; Hong, S. W.; Jeong, U.; Xu, T.; Russell, T. P. *Science* **2009**, *323* (February), 1030–1033.

(96) Zhang, J.; Posselt, D.; Smilgies, D.-M.; Perlich, J.; Kyriakos, K.; Jaksch, S.; Papadakis, C. M. *Macromolecules* **2014**, *47*, 5711–5718.

(97) Vora, A.; Wojtecki, R. J.; Schmidt, K.; Chunder, A.; Cheng, J. Y.; Nelson, A.; Sanders, D. P. *Polym. Chem.* **2016**, *7* (4), 940–950.

(98) Seshimo, T.; Maeda, R.; Odashima, R.; Takenaka, Y.; Kawana, D.; Ohmori, K.; Hayakawa, T. *Sci. Rep.* **2016**, *6* (1), 19481.

(99) Kim, S.; Nealey, P. F.; Bates, F. S. *ACS Macro Lett.* **2012**, *1* (1), 11–14.

(100) Kim, S.; Nealey, P. F.; Bates, F. S. *Nano Lett.* **2014**, *14*, 148–152.

(101) Zhou, S. X.; Janes, D. W.; Kim, C. Bin; Willson, C. G.; Ellison, C. J. *Macromolecules* **2016**, acs.macromol.6b01382.

(102) Jeong, S.-J.; Kim, J. Y.; Kim, B. H.; Moon, H.-S.; Kim, S. O. *Mater. Today* **2013**, *16* (12), 468–476.

Chapter 2

Characterization of the shape and line-edge roughness of polymer gratings with grazing incidence small-angle X-ray scattering and atomic force microscopy

2.1 Abstract

Grazing-incidence small-angle X-ray scattering (GISAXS) is increasingly used for the metrology of substrate-supported nanoscale features and nanostructured films. In the case of line gratings, where long objects are arranged with a nanoscale periodicity perpendicular to the beam, a series of characteristic spots of high-intensity (grating truncation rods, GTRs) are recorded on a two- dimensional detector. The intensity of the GTRs is modulated by the three- dimensional shape and arrangement of the lines. Previous studies aimed to extract an average cross-sectional profile of the gratings, attributing intensity loss at GTRs to sample imperfections. Such imperfections are just as important as the average shape when employing soft polymer gratings which display significant line-edge roughness. Herein are reported a series of GISAXS measurements of polymer line gratings over a range of incident angles. Both an average shape and fluctuations contributing to the intensity in between the GTRs are extracted. The results are critically compared with atomic force microscopy (AFM) measurements, and it is found that the two methods are in good agreement if appropriate corrections for scattering from the substrate (GISAXS) and contributions from the probe shape (AFM) are accounted for.

2.2 Introduction

Gratings consist of regularly spaced arrays of shapes arranged in parallel, with features over a range of length scales depending on the application considered. For example, gratings are used as filters to control the movement of particles with dimensions from millimetres to micrometres, as optical components to split and diffract light with wavelengths of several hundreds of nanometres, and as part of the basic line and space patterns for integrated-circuit (IC) design layouts extending a few tens of nanometres. The dimensions of a grating affect the device performance, so accurate characterization is critical to the manufacturing process. In the case of nanometre-scale gratings for ICs, where lithographic processes are near the resolution limit, dimensional control is particularly challenging. Therefore, there is a demand for metrology that can quantitatively probe these length scales and extract both the average structure and statistical variation.

The structure of nanoscale gratings can be evaluated by direct observation using microscopy techniques. Top-down scanning electron microscopy (SEM) measurements provide lateral information, such as the width and pitch of the lines, and deviations along the main direction of each shape within the grating (line-edge profile). Cross-sectional SEM and transmission electron microscopy (TEM) measurements, on the other hand, probe the vertical profile of the gratings (height, width and side-wall angle). Atomic force microscopy (AFM), tilted cross-sectional SEM and TEM tomography provide combined information (both lateral and vertical). All the above-mentioned techniques are capable of recording detailed structural information (approaching ~ 1 nm) within a limited area of a sample.

In contrast with imaging methods, metrology based on X-ray scattering probes nanostructures over large areas, without compromising resolution and within a short acquisition time. One of the most actively used X-ray techniques to analyze a lithographically defined grating structure is critical-dimension small-angle X-ray scattering (CD-SAXS).[1–5] A grating sample is aligned normal to the X-ray beam and parallel to the rotation axis. A series of transmission scattering images are collected over a wide range of sample rotation angles and the reciprocal-space map

(RSM) is reconstructed from these images. The detailed structural information of an average profile is determined quantitatively by fitting the recorded scattering intensity in the RSM with the scattering profiles calculated from a model.[5–7] In order to collect scattering data with sufficient intensity transmitted through the substrate (typically a silicon wafer), a relatively high energy X-ray beam is required in this technique. In addition, CD-SAXS requires continuous collection of scattering images from a single spot on the sample to expand the momentum transfer range probed and to access vertical structural information. Hard gratings with stable materials (Si and SiO_x) are clearly suitable for CD-SAXS measurements, while a limited number of studies have addressed soft gratings such as photoresist patterns and nanoimprint polymer gratings.[1,3,6,8] A recent different X-ray scattering technique records transmission at the edge of the sample while keeping the incident beam at grazing angle.[9] This method has several distinct advantages, such as probing surface-normal scattering vectors continuously without the need to reconstruct reciprocal space. Another frequently used X-ray method is grazing-incidence small-angle X-ray scattering (GISAXS).[10–13] This is a reflection-mode technique where the surface of the sample is exposed to a focused X-ray beam at a grazing incidence angle. The intensity is dramatically enhanced by the large area probed, owing to the projection of the X-ray beam at a shallow incident angle, resulting in short measurement times at a synchrotron facility. Moreover, a single GISAXS image contains information on the full three- dimensional characteristic features of the sample probed, eliminating the step of reconstructing the RSM. Because of these significant advantages in data collection, GISAXS is a suitable and attractive metrology technique for both soft and hard gratings. Several studies in recent years have used reflection-mode

X-ray scattering measurements to study grating structures.[14–17] Yan and Gibaud *et al.* performed experiments with hard silicon gratings and measured high- intensity spots (grating truncation rods, GTRs) following a characteristic arc defined by the Ewald sphere. The in-plane separation of these spots reflects the period of the grating studied. The actual intensity at these spots depends on both the in-plane (i.e. the shape of the grating) and the out-of-plane characteristics of the sample (i.e. the multilayer structure of the substrate). Soltwisch *et al.* employed parallel finite-element calculations to extract an average two-dimensional shape based on the intensity variation along GTRs.[18,19] In the case of polymer-based soft gratings, a significant component of the recorded intensity consists of diffuse scattering far from the specific angular coordinates of GTRs. This component of the pattern could be associated with variations from the mean shape considered in the analysis of related scattering experiments.[20–22] Rueda and co-workers employed models of short rods in a first attempt to characterize the fidelity of nanoscale polymer gratings with GISAXS.[23,24] It was found that the quality of the grating controls the magnitude of the recorded GISAXS intensity. However, the agreement between modeled intensity and experimental data was rather qualitative, emphasizing the need for an improved methodology. In this study, we describe a systematic effort to characterize polymer grating structures quantitatively using GISAXS. In order to develop a simple but realistic GISAXS model, a series of GISAXS experiments at different incident angles were performed on a crosslinked polystyrene (XPS) nanoscale grating fabricated by 193 nm immersion (193i) lithography.[25] Such gratings serve as essential components of chemical patterns for a directed self-assembly (DSA) process that employs block copolymer films to enhance the feature density in the patterns produced.[26] Since the final DSA features are significantly sensitive to the geometry of the chemical patterns, a careful characterization of this grating structure, referred to as a PS guiding stripe, is crucial for optimization of the DSA process. We compare our analysis with independent characterization methods such as AFM and find good agreement between the two techniques. Our results unequivocally support the ability of GISAXS to probe important three-dimensional characteristics of the samples employed. Therefore, the present study provides significant promise for future metrology and inspection of buried morphologies in directed self-assembled block copolymer patterns.

2.3 Experimental section

2.3.1 Sample preparation

The polymer gratings studied herein are made of XPS line-and-space patterns which are employed as guiding stripes for a 3X density multiplication DSA process implemented on an all-track 300 mm wafer process.[25] First, a layer of SiN (thickness approximately 13 nm) was deposited on 300 mm Si wafers via chemical vapor deposition (CVD) as an inorganic anti-reflective coating. Next, an XPS thin film of approximately 8 nm thickness was spin-coated and annealed at 315°C for 5 min in an N_2 atmosphere. After resist coating, an ASML XT:1950Gi scanner was used to fabricate line-space patterns. In the subsequent etch step, the exposed XPS was removed by plasma etching, whilst the remaining XPS lines were further trimmed down to obtain an optimized line width for DSA, thus creating XPS gratings with 84 nm pitch and ~ 20 nm line width spanning a 5 × 7.5 mm area. A schematic of the guiding stripes is shown in Figure 2.1.

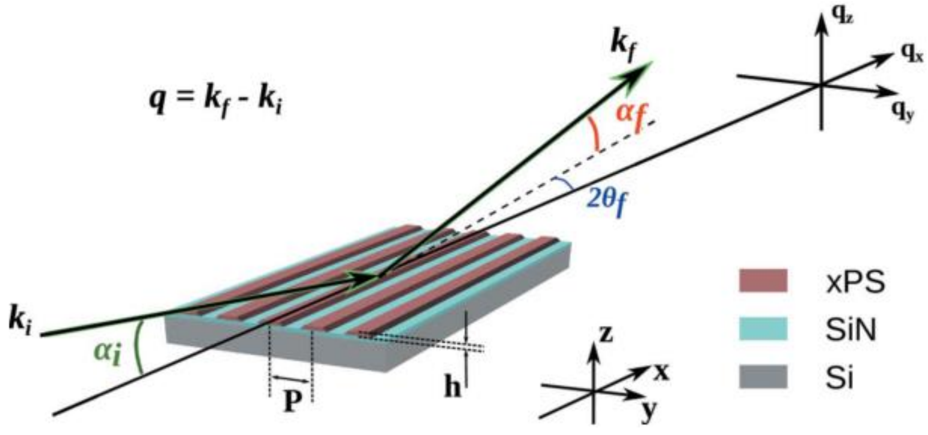

Figure 2.1. Schematic illustration of a PS guiding stripe and the geometry of a GISAXS experiment.

2.3.2 Atomic force microscopy

A Bruker 3A Multimode 5AFM was used to image the PS guiding stripe sample in tapping mode. To a first approximation, the shape of the gratings can be described as parallel trapezoidal-like shapes along two dimensions (y and z in the notation of this study), extending throughout the sample along x.[27]

2.3.3 X-ray scattering experiments

GISAXS experiments were performed on the beamline Sector 8-ID-E at the Advanced Photon Source, Argonne National Laboratory.[28] The samples were measured under vacuum with an incident X-ray beam of 7.35 keV energy (λ = 0.1687 nm). The X-ray beam was 20 mm in height and 100 mm in width. The sample-to-detector distance was 552 mm, allowing the collection of scattering images over a wide q range [$q = (4\pi/\lambda)\sin(\theta)$, where θ is half the scattering angle and λ is the wavelength of the incident radiation]. The sample originally prepared on a 300 mm wafer was cleaved into an approximately 5 by 7.5 mm (x versus y) sized piece which was fully covered by an XPS grating. The azimuthal rotation angle, defined as the angle between the incident X-ray beam and the PS guiding stripe direction, was set to zero by carefully aligning the grating to the incident beam. The geometry of the measurement is presented in Figure 2.1. Each GISAXS two-dimensional pattern was the result of summing 30 images of 1 s exposure scans to obtain a desirable signal-to-noise ratio. A fresh area was exposed to the X-ray beam for each incident angle. The angular coordinates can be transformed to momentum transfer coordinates as follows:

$$\begin{pmatrix} q_x \\ q_y \\ q_z \end{pmatrix} = \frac{2\pi}{\lambda} \begin{bmatrix} \cos(2\theta_f)\cos(\alpha_f) - \cos(\alpha_i) \\ \sin(2\theta_f)\cos(\alpha_f) \\ \sin(\alpha_f) + \sin(\alpha_i) \end{bmatrix}, \qquad (1)$$

where $2\theta_\mathrm{f}$, α_f and α_i are the in-plane scattering angle, out-of-plane scattering angle and incident angle, respectively.[29] A total of eight different scattering images at nominal incident angles of 0.5, 0.8, 1.0, 1.2, 1.5, 1.8, 2.0 and 2.5° were collected. Small corrections to the above values were determined, based on the sample-to-detector distance, the specular position detected on the image and the direct-beam position.

Prior to the GISAXS experiments, the specular X-ray reflectivity for the sample was recorded to characterize electron-density changes perpendicular to the sample plane. These data have already been presented elsewhere,[27] where we noted two important aspects: (i) a dispersion profile that increases gradually with depth as we move from the grating top surface to the substrate; and (ii) a rough SiN layer of ~13 nm between the polymer and the silicon substrate. The significant roughness of the underlying substrate layer probed by X-ray scattering can be attributed either to physical roughness or to electron-density changes due to a thin oxide layer which can be further amplified by the plasma etch process.

In this work, we will use a five-layer description to characterize the electric field intensity as a function of depth, following the Parrat formalism[30] and based on information from reflectivity profiles. The characteristics of these layers are presented in Table 1. The parameters h and σ_h represent the height and the deviation in height for the PS grating model considered, and c corresponds to the coverage, calculated from the pitch and profile modeled during a step in the GISAXS optimization procedure.

Table 2.1. Characteristics of the media involved in the five-layer description.

Material	Thickness (nm)	δ	β	σ (nm)
Air	0.0	0.0	0.0	σ_h
Polymer (xPS)	h	$c \times 4.353 \times 10^{-6}$	$c \times 7.47 \times 10^{-9}$	0.4
SiO_2	1.9	8.55×10^{-6}	7.5×10^{-7}	0.2
SiN	10.7	1.08×10^{-5}	9.0×10^{-7}	0.4
Si	∞	9.107×10^{-6}	2.467×10^{-7}	0.0

2.3.4 Modeling of scattering from polymer gratings

A general expression for the scattering intensity of an X-ray experiment with a sample of N shapes is

$$I = \frac{1}{V} \sum_{J=1}^{N} \sum_{K=1}^{N} \mathcal{F}_J(\mathbf{q}) \mathcal{F}_K^*(\mathbf{q}) \exp(i\mathbf{q}\Delta\mathbf{R}), \qquad (2)$$

where $\Delta\mathbf{R}$ denotes the separation between shapes J and K. F symbolizes the form factor within the distorted-wave Born approximation to account for multiple scattering effects at low incident angles:[29,31,32]

$$\begin{aligned} \mathcal{F}(\mathbf{q}) &= \mathcal{F}(q_x, q_y, q_z) \\ &= \mathcal{F}(q_x, q_y, k_i^z, k_f^z) \\ &= T(\alpha_i)T(\alpha_f)F(q_x, q_y, k_f^z - k_i^z) \\ &\quad + T(\alpha_f)R(\alpha_i)F(q_x, q_y, k_f^z + k_i^z) \\ &\quad + T(\alpha_i)R(\alpha_f)F(q_x, q_y, -k_f^z - k_i^z) \\ &\quad + R(\alpha_i)R(\alpha_f)F(q_x, q_y, -k_f^z + k_i^z), \qquad (3) \end{aligned}$$

where F is the Fourier transform of the shape function, k_i^z and k_f^z are wavevectors corrected for refraction at the polymer–air interface, and T and R are transmission and reflection coefficients, respectively, calculated at specific angles for the polymer layer (second medium, Table 2.1).

While microscopy experiments typically resolve areas of ~ 1 mm^2, GISAXS probes millimetre-long samples along x and several tens of micrometres along y with nanometre resolution. To analyze the data recorded, it is necessary to employ a reduced model relative to equation (2) by introducing approximations. We describe the sample by defining a unit cell with a size equal to the pitch distance P along y, and an interference function $S(\mathbf{q})$ describes the amplification of intensity at the Bragg peaks, $q_y = 2n\pi/P$, where n is an integer. We chose to model the intensity in between the Bragg peaks following the 'decoupling approximation',[33] which assumes that shape fluctuations are decoupled from their spatial location. Considering the manufacturing procedure, we expect that each side wall should display fairly independent fluctuations (an assumption tested in the Results section). Therefore

$$\begin{aligned} I &= \frac{1}{V}\sum_{J=1}^{N}\sum_{K=1}^{N}\langle \mathcal{F}_J(\mathbf{q})\mathcal{F}_K^*(\mathbf{q})\rangle \exp(i\mathbf{q}\Delta\mathbf{R}) \\ &= \frac{1}{V}\left\{N\left[\langle \mathcal{F}(\mathbf{q})^2\rangle - \langle \mathcal{F}(\mathbf{q})\rangle^2\right] + N\langle \mathcal{F}(\mathbf{q})\rangle^2 S(\mathbf{q})\right\} \\ &= A\left[\Phi(\mathbf{q}) + \langle \mathcal{F}(\mathbf{q})\rangle^2 S(\mathbf{q})\right], \end{aligned} \tag{4}$$

where A is a proportionality constant,

$$S(\mathbf{q}) = \frac{1}{N}\sum_{J=1}^{N}\sum_{K=1}^{N}\exp(i\mathbf{q}\Delta\mathbf{R}) \tag{5}$$

And

$$\Phi(\mathbf{q}) = \langle \mathcal{F}(\mathbf{q})^2\rangle - \langle \mathcal{F}(\mathbf{q})\rangle^2. \tag{6}$$

In practice, A will depend on parameters such as the exposure time and illuminated area. An additional complication in determining A arises from the fact that $S(\mathbf{q})$ displays peak intensities that depend on the sample size, defects and beam characteristics (length and coherence), and is convoluted with the detector resolution. It is therefore challenging to calculate a priori the contributions of $\Phi(\mathbf{q})$ and $\langle F(\mathbf{q})\rangle^2 S(\mathbf{q})$ in absolute intensities. In our study, we wish to formulate these contributions when reducing the shape description to a two-dimensional profile along the y and z directions (see Figure 2.2), with both height fluctuations and line-edge roughness presenting as side-wall displacements along x. We argue that a simple rule for their relative contributions should be determined to minimize the fitting parameters.

A simple approach to modeling shape fluctuations in a grating is to approximate each long shape with n fluctuating elementary segments aligned along the main direction of each line (x herein), each with a length equal to a characteristic correlation length λ_x.[3] For each of these segments, the two-dimensional shape profile (along y and z) remains constant, and therefore

$$\mathcal{F}(\mathbf{q}) = \sum_{j=1}^{n} \lambda_x \frac{\sin(0.5\lambda_x q_x)}{0.5\lambda_x q_x} \mathcal{F}_{2D}(q_y, q_z) \exp\left[iq_x \Delta r_j(x)\right], \quad (7)$$

where F_{2D} is the Fourier transform of the two-dimensional shape profile within the distorted-wave Born approximation [see equation (3)]. If we focus on reciprocal-space coordinates where $q_x = 0$,

$$\langle \mathcal{F}(\mathbf{q}) \rangle^2 = \left[n\lambda_x \langle \mathcal{F}_{2D}(q_y, q_z) \rangle\right]^2 = L_0^2 \langle \mathcal{F}_{2D}(q_y, q_z) \rangle^2, \quad (8)$$

where L_0 is the total length of the grating probed by the beam. Beyond a distance λ_x along x, the segments fluctuate independently. Therefore the variance of the shapes can be modeled as the sum of the variances of the segments. As a result,

$$\Phi(\mathbf{q}) = n\lambda_x^2 \Phi_{2D}(q_y, q_z) = \lambda_x L_0 \Phi_{2D}(q_y, q_z), \quad (9)$$

and $\Phi(\mathbf{q}) \propto \lambda_x L_0$ and $\langle F(\boldsymbol{q}) \rangle^2 \propto L_0^2$. Therefore, we write equation (4) as

$$I = A\left[\lambda_x L_0 \Phi_{2D}(q_y, q_z) + L_0^2 \langle \mathcal{F}_{2D}(q_y, q_z) \rangle^2 S(q_y)\right], \quad (10)$$

where

$$S(q_y) = \sum_{q_y = g = 2\pi n/P} G(g, \Lambda), \quad (11)$$

and $G(g, \Lambda)$ is a Gaussian with mean position g and standard deviation Λ. The significance of this simple scaling is that the length of the grating and the characteristic length of the fluctuations contribute to the intensity of the scattering at GTRs and in between, along the arcs. If the length probed at different incident angles α_{i} is related to the beam height T (or, more appropriately, the coherence length of the beam) as the footprint $L_0 = T/\sin(\alpha_{\mathrm{i}})$, then the above equation is written as

$$I = \frac{A'}{\sin(\alpha_{\mathrm{i}})}\Phi_{2\mathrm{D}}(q_y, q_z) + \frac{B'}{\sin^2(\alpha_{\mathrm{i}})}\langle\mathcal{F}_{2\mathrm{D}}(q_y, q_z)\rangle^2 S(q_y), \quad (12)$$

where A' and B' are now constants throughout measurements at different incident angles. We anticipate deviations from this scaling due to imperfections in the model of independently fluctuating shapes of length λ_x i.e. stitching effects in the mask employed in photolithography when patterning with the resist. We also note that since the intensity of the Bragg peaks $S(\mathbf{q})$ depends on parameters relating to sample characteristics along y, the actual value of A' cannot be employed to determine λ_x.

We found that the above expression suffices to provide a good description of our data. However, the model was overestimating the height fluctuations in our polymer gratings to capture scattering close to $q_{\mathrm{y}} = 0$. Our hypothesis is that such surface scattering originates partly from the substrate rather than the polymer.

Summarizing, we described the intensity along the arcs q_x=0 for experiments at different incident angles α_i where i=1,…,M, using:

$$I = \frac{A'}{\sin(\alpha_{\mathrm{i}})}\Phi_{2\mathrm{D}}(q_y, q_z) + \frac{B'}{\sin^2(\alpha_{\mathrm{i}})}\langle\mathcal{F}_{2\mathrm{D}}(q_y, q_z)\rangle^2 S(q_y) + \frac{C'}{\sin(\alpha_{\mathrm{i}})}I_{\mathrm{S}}. \quad (13)$$

The parameters of $S(q_y)$ where kept the same for all α_i since the locations are dictated by the gratings' periodicity while Λ is determined by detector resolution and beam profile. A', B' and C' are constants kept same throughout all arcs. $F_{2D}(q_y,q_z)$ is determined by a number of parameters that describe the two dimensional profile of the gratings while given the average shape, $\Phi_{2\mathrm{D}}(q_{\mathrm{y}}, q_{\mathrm{z}})$ is calculated based on estimated standard deviations for sidewall displacements and height fluctuations. I_S is modeled using three additional parameters. All modeling was performed with in-house developed software taking advantage of parallel computations using OpenMP.[34] In practice, representative samples of shape distributions are drawn and averages of $F(\mathbf{q})$ and $|F(\mathbf{q})|^2$ are calculated on separate threads. The model parameters are determined by standard non-linear optimization algorithms.[35]

2.4 Results and discussion

2.4.1 Atomic force microscopy

A three-dimensional image of the recorded data from AFM is presented in Figure 2.2. The height of the gratings is 7 - 8 nm, the top width ≈ 20 - 25nm while the bottom width appears to be 50 - 60 nm. This is in agreement with a sloped sidewall forming an angle of ≈ 60° with the normal to the surface. The pitch of the gratings is ≈ 84 nm. Fluctuations along x can be characterized using the concept of line edge roughness (LER) and can be readily visualized by plotting contour lines at a fixed height. The 18 contour lines calculated fluctuate around a mean position with a standard deviation σ_y of approximately 1.5 nm; note that line edge roughness (LER) commonly refers to $3\sigma_y$. To further illustrate the concept, Figure 2.3 presents a top-down view of contour lines drawn at different heights over a region of the area probed. It is clear that contour lines from the same sidewall present similar fluctuations. In order to quantify the degree of covariance we can calculate the mean of the product $\langle (y_1(x) - \mu_1)(y_2(x) - \mu_2) \rangle$, where $y_1(x)$, $y_2(x)$ are coordinates of two selected contours on the same sidewall and μ_1, μ_2 their mean values. The ratio of the covariance to the product of the standard deviations of $y_1(x)$ and $y_2(x)$ (Pearson correlation coefficient) provides a normalized measure of coupled variations of the contours along the lateral coordinate y. The Pearson correlation coefficient is above 0.9 between contour lines on the same sidewall and heights between 3 - 7 nm. We conclude therefore, that a one-dimensional roughness (along x, ignoring a potential z-dependence) is a fairly reasonable approximation in our analysis. Thus, we can calculate the deviation of the top width of the gratings as $\sigma_T = \sqrt{2}\sigma_y$, where σ_y is the standard deviation describing fluctuations a sidewall along y.

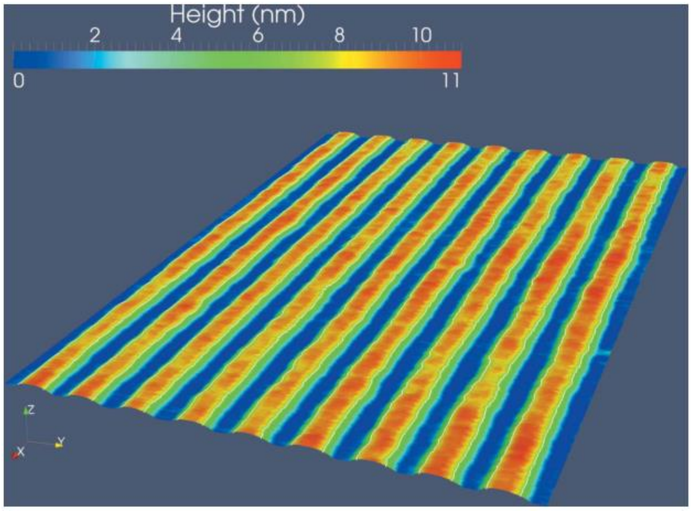

Figure 2.2. AFM measurement of a small part of the sample studied, approximately 1 by 1 mm.

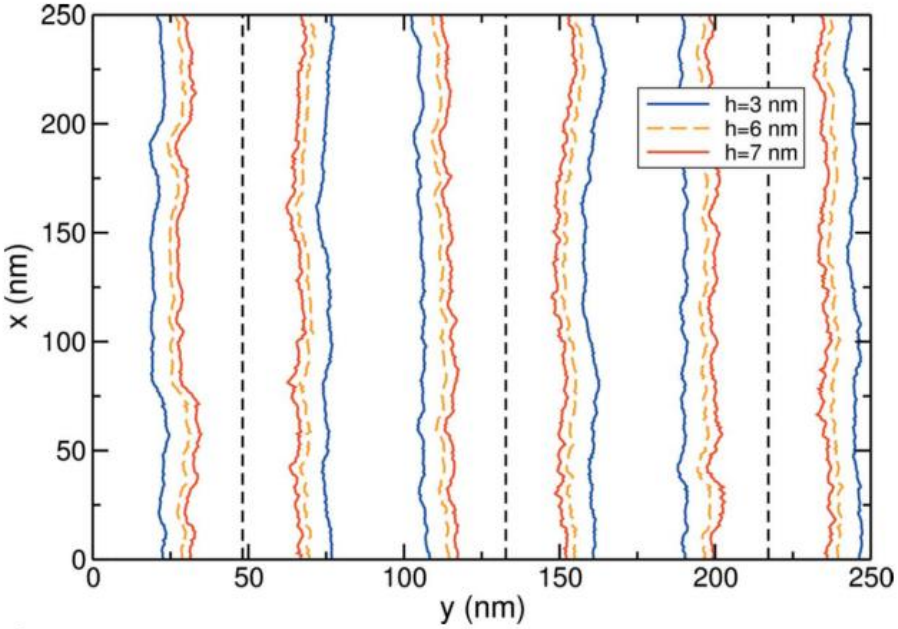

Figure 2.3. Contour lines of AFM data along the x direction (Figure 2.2) at specific height values (h) over the probed region of 250 by 250 nm. The dashed line represents the average position of the center of each shape.

We proceeded in further analysis of the AFM image by extracting the standard deviation of each of the contour lines at *h* = 6 nm and present these results in Figure 2.4. While an average value of σ_y of around 1.5 nm is present in our sample, the analysis of each line individually provides a measure of the error involved in such calculations; as it is observed values between 1 - 2 nm can be found based on calculations with the full image (length equal to 1μm). We also quantified the extent of height fluctuations at the centerline position (at dashed lines in Figure 2.3) and plot the corresponding deviations in the inset. We note that the accuracy of the AFM in probing shape fluctuations in these nanoscale-sized objects is limited; the total area probed is small and the LER is approaching the lateral image resolution (pixel size ≈ 1 nm^2). Furthermore, data are affected by acquisition parameters, tip radius and aspect ratio and potential damage induced during measurement. We will expand on these issues when comparing to the X-ray scattering results.

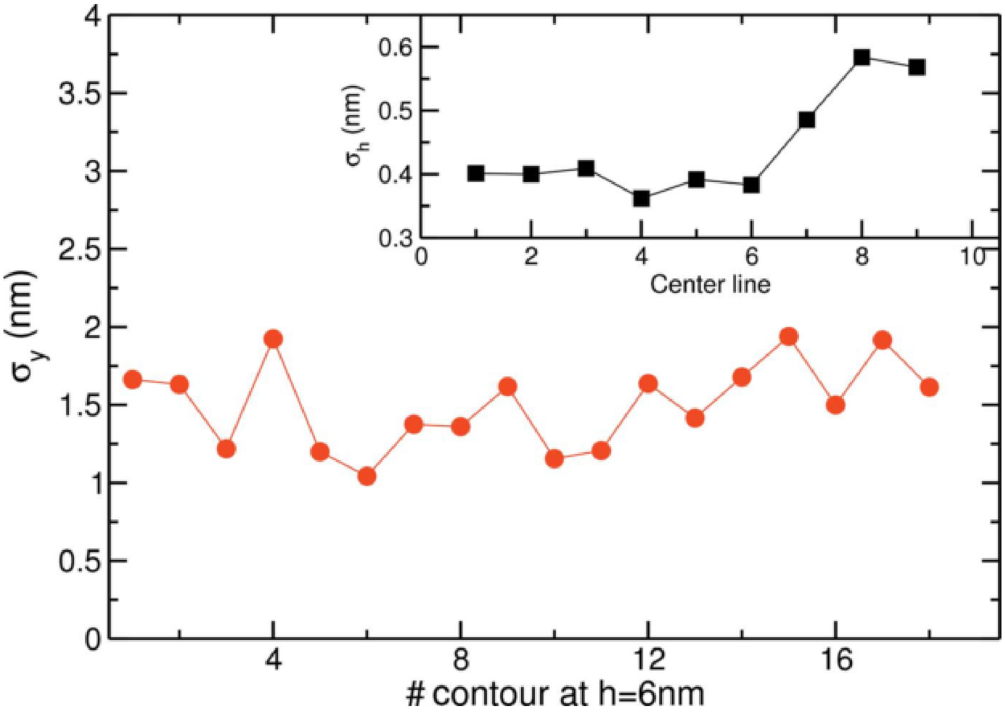

Figure 2.4. Standard deviations of fluctuations around a mean position along x extracted from 18 different lines at *h* = 6 nm over a length of 1 mm. The inset provides similar data for height fluctuations along 1 mm for nine different lines determined at the center of each shape.

Beyond fluctuations, we can extract an estimate of the average profile along *y* and *z* from the AFM data. We integrated the shape along the *x* direction and present the outcome from one shape in Figure 2.5. using a colormap. The continuous line depicts a contour line as an indicator of the average shape. We observe that there is significant rounding in all edges, a result that is in part due to the convolution of the actual structure with the tip shape.

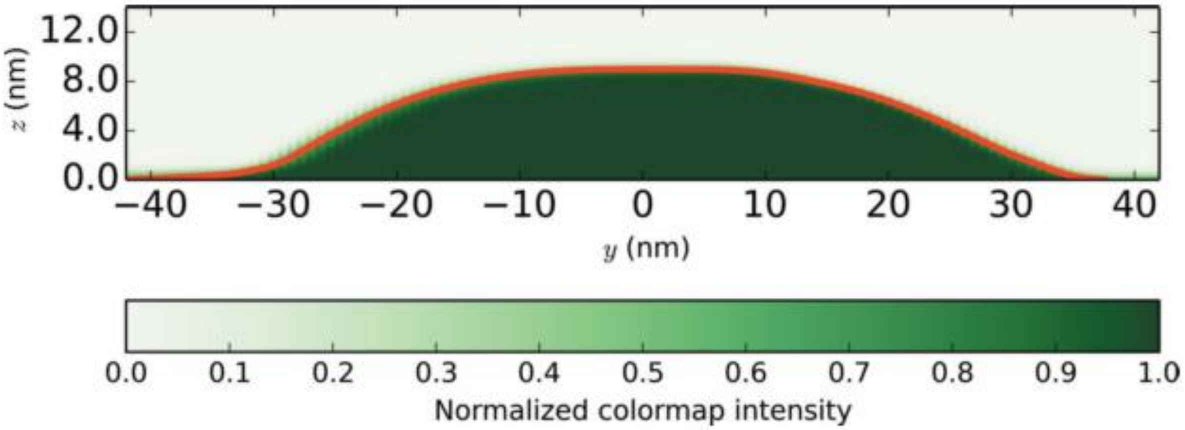

Figure 2.5. A two-dimensional profile extracted from the AFM image by integrating along the x direction. The red line depicts a contour at 2/3 of the normalized colormap intensity.

2.4.2 GISAXS experiments

Figure 2.6 presents three GISAXS experiments with the gratings sample at different incident angles. Several features that have been previously reported are directly discernible. First, a series of high intensity spots or grating truncation rods (GTRs)[14] are periodically placed on an arc that has its highest point at $\alpha_f=\alpha_i$. The origin of these high intensity GTRs is the effective "infinite" dimension of the gratings along x and their repeated placement at every pitch distance P along y. These effects, produce scattering along the $q_x = 0$ arc and at every $q_y = 2\pi n/P$ Bragg peak where n an integer. The intensity at GTRs depends both on the beam and grating structures. We note that hard gratings were reported to present intensity only at specific angular coordinates that correspond to these spots[14,18,19] while polymer gratings often present diffuse scattering throughout the image and a lack of GTRs.[23,24] Our data are distinct from past studies since they combine both effects reported: a clear set of GTRs combined with a low intensity background scattering. The broad tilted truncation rods in the background scattering are indicative of a sloped sidewall that a rudimentary analysis would confirm to be at an angle of ≈ 60 - 65 degrees with respect to the substrate normal direction.[29] By performing measurements at different incident angles we found that while the GTRs are shifting to higher angles (highest point of arc at $\alpha_f=\alpha_i$), the background scattering appears to be independent of this change in the momentum transfer center of coordinates (arc corresponds always to $q_x \approx 0$).

The intensity along the GTRs (corresponding to $q_x=0$) can be extracted from each of these measurements as a function of momentum transfer using equation (1). A representative plot for α_i =2.0 degrees is shown in the bottom right panel of Figure 2.6. Features symmetric around $q_y=0$ are indicative of good alignment to the beam. Data can be analyzed as a function of q_y and the two angular coordinates α_i (constant for each measurement) and α_f (which varies along the GTRs) using equation (13). We avert from employing a single 2D shape and introduce a population of polygons that obey specific distributions for height and the location of each sidewall. Each polygon is assigned a height based on a Gaussian distribution $N(h, \sigma_h)$ by extrapolating or contracting the topmost segment of the sidewall profile. The shape of the sidewall is described by a series of linear segments defined by slope changes in a similar context to past X-ray scattering studies.[6] The overall width of the two-dimensional shape (and its coordinate center) is determined by adding a displacement to the left and right sidewalls, each selected independently from a Gaussian distribution $N(0, \sigma_y)$. Within this approach the top width fluctuates with a variance $\sigma_T^2 = 2\sigma_y^2$. The Fourier transformation of each shape is performed based on analytic calculations described in the literature.[36–38]

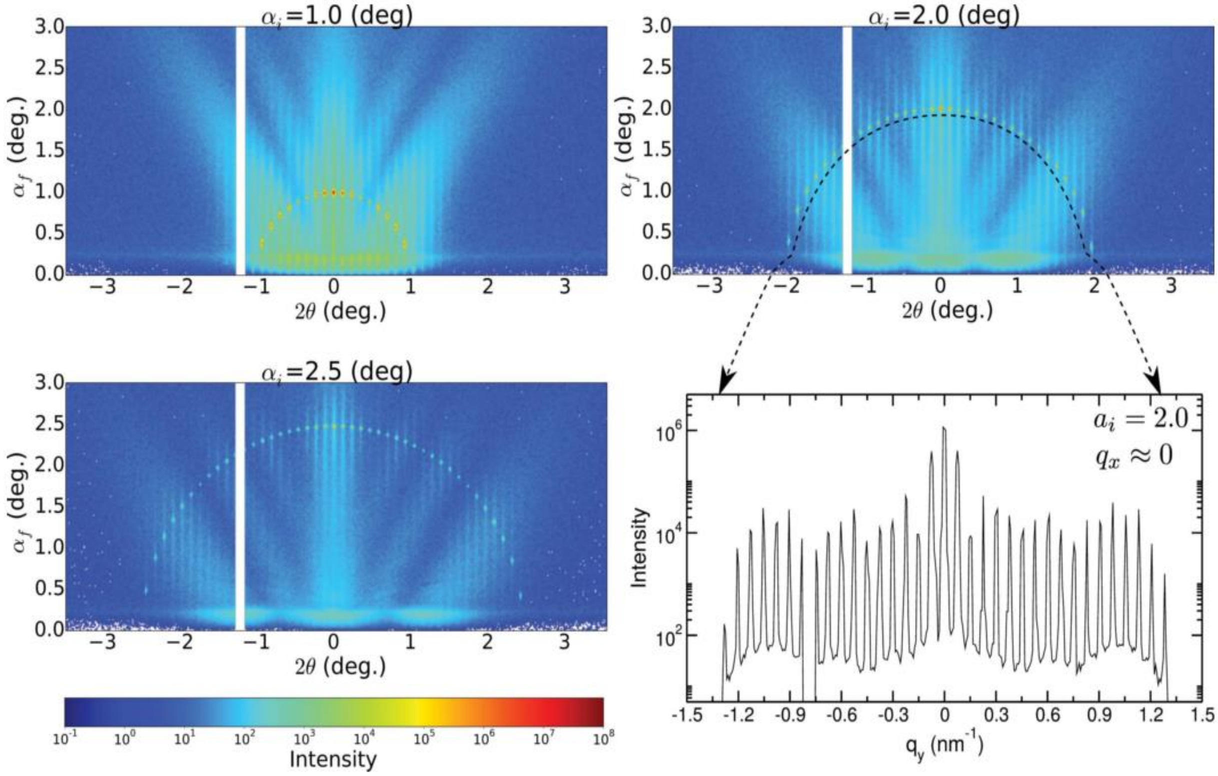

Figure 2.6. GISAXS data at incident angles $\alpha_i = 1.0$, 2.0 and 2.5°. The bottom right-hand image displays the intensity along the arc $q_x = 0$ for $\alpha_i = 2.0°$.

As an example of our model, Figure 2.7 presents the form factor of a trapezoid that approximates our gratings together with the variances $\Phi_{2D}(q_y,q_z)$ calculated when σ_y=1.5 nm and σ_h=0.6 nm. For clarity, in this specific figure, calculations are performed within the Born approximation [contrary to the actual fits performed employing equation (3)] and no refraction for k_z components is taken into account. This simple 2D Fourier form factor calculation suffices to underline an important aspect of the analysis procedure. Each arc drawn on the left panel represents the collection of points in the (q_y,q_z) space probed by performing the GISAXS experiment at different incident angles. It is evident, that a simultaneous fit on data from multiple incident angles assists greatly the determination of the underlying form factor and fluctuations present since specific features characteristic of the shape in question can be examined.

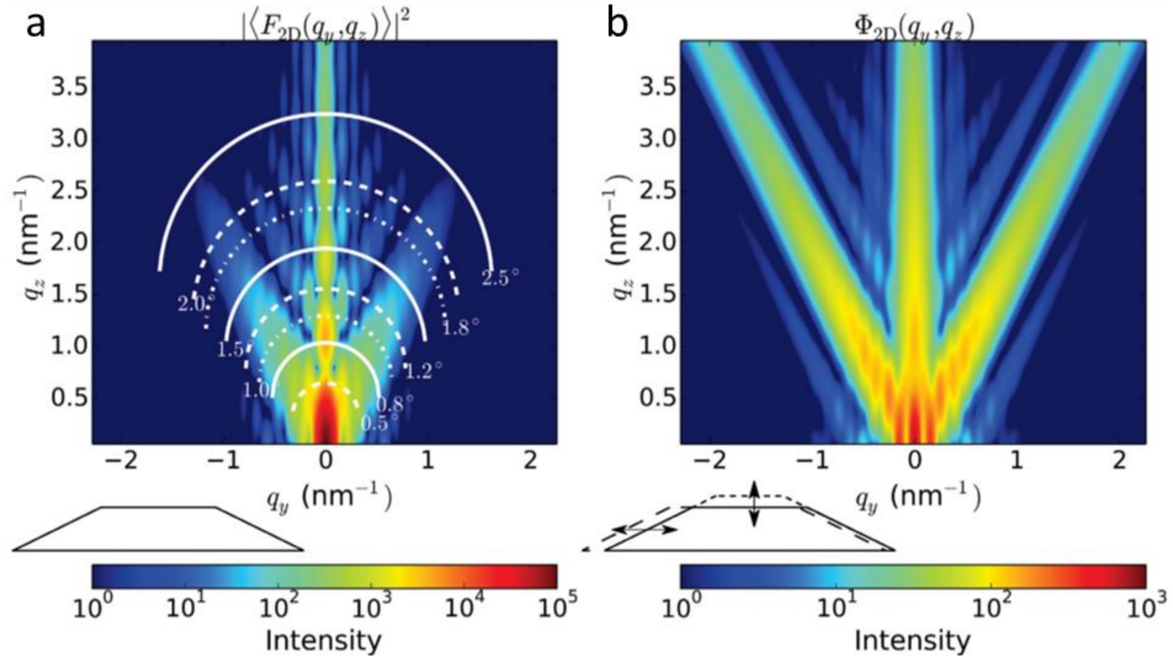

Figure 2.7. (a) The average form factor $F_{2D}(q_y, q_z)$ within the Born approximation of a trapezoid with a top width of 21.8 nm and a bottom width of 54.4 nm. The arcs drawn in white indicate the ensemble of points probed by each measurement at different incident angles. Each side wall fluctuates independently around a mean position with σ_y = 1.5 nm, while the top exhibits height fluctuations σ_h of 0.6 nm. (b) The resulting variance in the form factor $F_{2D}(q_y, q_z)$.

The population of 2D shapes was optimized in order to best reproduce the intensities recorded along the arcs $q_x = 0$ following equation (13). It is important to identify sources of errors present in the procedure before discussing any results from our model. First, direct selection of pixels that correspond to one arc is not straightforward; none has exactly q_x=0 and this is inevitable irrespective of the resolution of the detector. The sharp intensity drop with q_x departing from zero introduces a challenge. Similar challenges are present along the q_y component; the high intensity at GTRs (to some extent due to the high accuracy of the manufacturing process) resulted in Bragg peaks defined by detector resolution. Despite these challenges, a trapezoid-like shape with dimensions close to what anticipated provided a satisfactory description of the intensity at all incident angles using equation (13). Before examining the actual best fits, we note that using several nodes for the sidewalls (beyond the simple trapezoid shape) improved the agreement between model and experiment significantly; this was attributed to the ability to introduce a "footing" in our shape as explicitly depicted in Figure 2.8. Extension to models of higher resolution (i.e. 8 nodes per sidewall) did not result to improved fits. This is not surprising given the upper limit of our resolution defined by the range of the momentum transfers probed. Along z, as can be readily deducted from Figure 2.7, $q_{z,\max} \approx 3.25\ \mathrm{nm}^{-1}$ limiting our resolution to $\approx$ 2 nm. The sidewalls of the best model (5 slope changes) presented fluctuations along y by $\sigma_y = 1.4$ nm and the heights $\sigma_h = 0.4$nm. Both values are in excellent agreement with the AFM experiment. If we omit contributions to the background scattering by the substrate (I_S) then the optimization procedure was driven to a model with similar sidewall but unphysical height fluctuations (σ_h = 1.5nm) in order to capture the intensity at low angles and close to the specular rod.

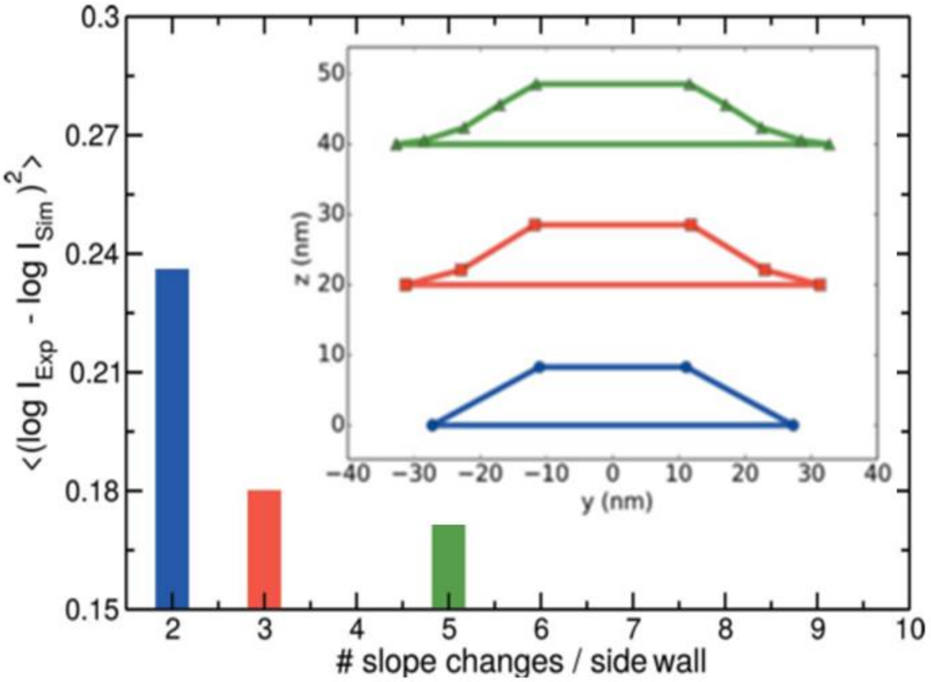

Figure 2.8. The objective function describing the agreement (lower is better) between the model and recorded intensity as a function of slope changes describing the side walls of the grating. The inset provides the optimal average shapes determined by the optimization procedures (displaced vertically for visualization).

The intensity along the arcs that results from the optimal model calculated is presented in Figure 2.9 for different incident angles. We remind the reader that while data are plotted along q_y, there is a monotonic decrease of q_z as we move from the left side of each figure towards the Yoneda peaks present at the maximum q_y value for each α_i. The best data to compare are between α_i=0.8−1.8° where substantial recorded intensity reveals oscillations characteristic of the form factor. We observed that the model described by equation (13) is in good agreement to experimental data both in terms of intensity at Bragg peaks corresponding to $P = 83.3 \pm 0.3$ nm as well as to the baseline modeled by the variances $\Phi(\mathbf{q})$ scaled by the procedure described earlier. A more rigorous approach would require the dissection of the shapes into different layers, calculation of the transmission and reflection coefficients in each layer, and then assembly of a form factor from individual slices.[39] As a final test of our method, in the next section we will attempt to directly compare the shape determined by fits on X-ray data to the one measured by microscopy in real space.

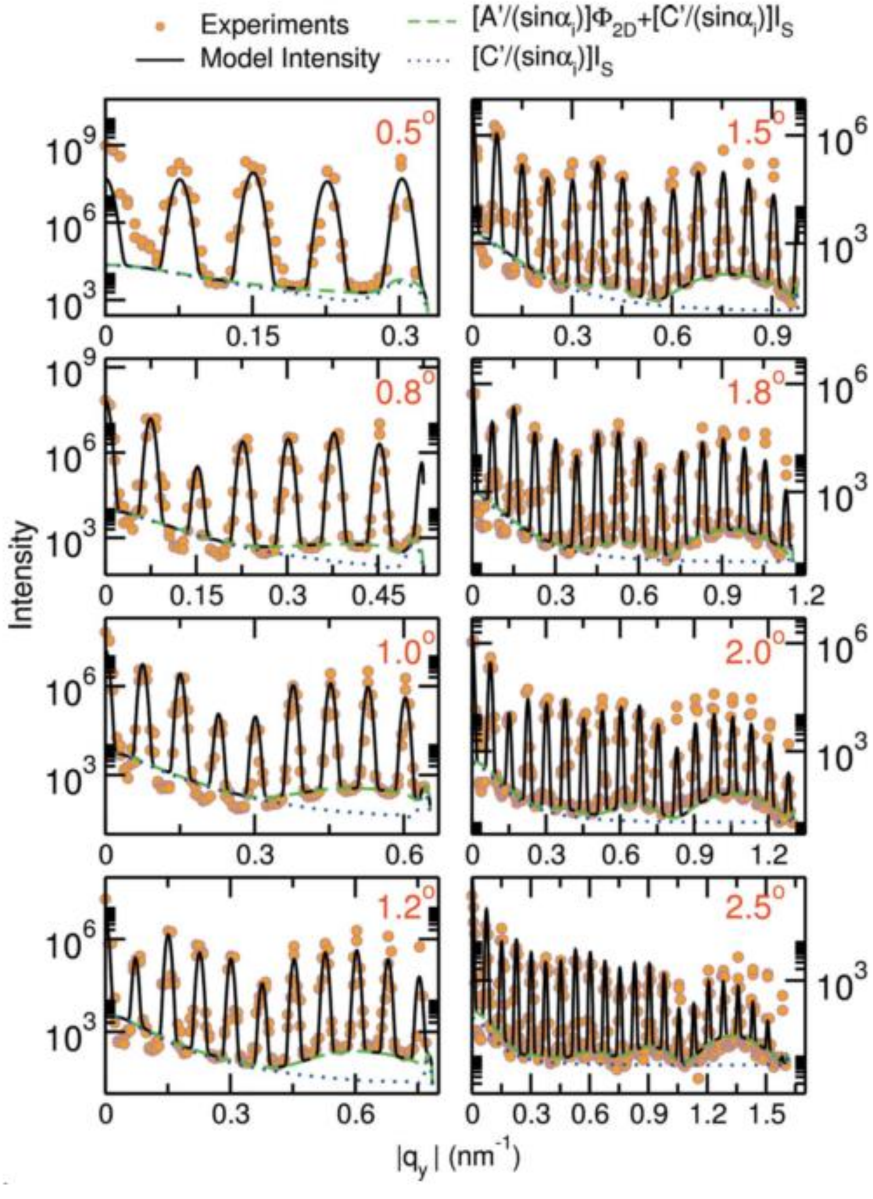

Figure 2.9. Arcs of intensity over $q_x \approx 0$ for different incident angles (points) from 0.5 to 2.5°. Continuous lines indicate the modeled scattered intensity from a distribution of two-dimensional shapes (with five slope changes) that vary in width and height. The dashed green lines denote the contribution from fluctuations calculated using $\Phi(\boldsymbol{q})$ and I_S following equation (13). The modeled intensity *versus* I_S is plotted as a dotted blue line. All calculations were performed within the distorted-wave Born approximation.

2.4.3 Comparison of GISAXS with AFM

The last part of this section aims to compare the profile extracted by X-ray scattering to the AFM measurement shown in Figure 2.2. We already mentioned in the previous section that GISAXS results are in quantitative agreement to AFM with regards to shape fluctuations; an LER of σ_y=1.5 nm is determined by both techniques. However, such an agreement is not true for the average cross-section profile determined by the two techniques. AFM provides high accuracy data regarding the height of the gratings but lacks significantly in determining the side wall profile. This partly a consequence of the lateral image resolution but mostly to contributions of the tip shape.

The top left panel in Figure 2.10 provides an example of a two-dimensional model for the shape of the probe used in AFM with a rounded tip and a sidewall angle. We can employ such models to simulate the interaction between the tip and the extracted shape from GISAXS data using procedures reported recently in the literature.[40] According to the manufacturer, the tip employed in our measurements should present a radius r of ≈ 10nm and an angle γ of 10 - 15 degrees. This is in agreement with our own imaging using SEM on a fresh tip; however repetitive use induces significant damage that renders both the radius and the angle larger. This is demonstrated in the images on the top right panel of Figure 2.10.

We proceeded performing calculations for two extreme cases of tip shape; first one with a r = 10 nm and $\gamma = 15°$ and a second case with r = 20 nm and $\gamma = 30°$. Figure 2.10 presents in the lower panel a critical comparison between the predicted shapes from GISAXS convoluted with the two tip profiles against the contour line extracted directly from the AFM data (Figure 2.5). We find that the comparison between GISAXS and AFM is nearly quantitative if a radius closer to 20 nm is considered. In practice, this large value is more of an "effective" radius since the profile measured by such a tip would be affected by the neighboring shape centered at ± 84 nm apart. Therefore, we conclude that while both techniques are consistent in terms of the LER probed, the average shape determined by GISAXS offers a more accurate representation of the sample structure.

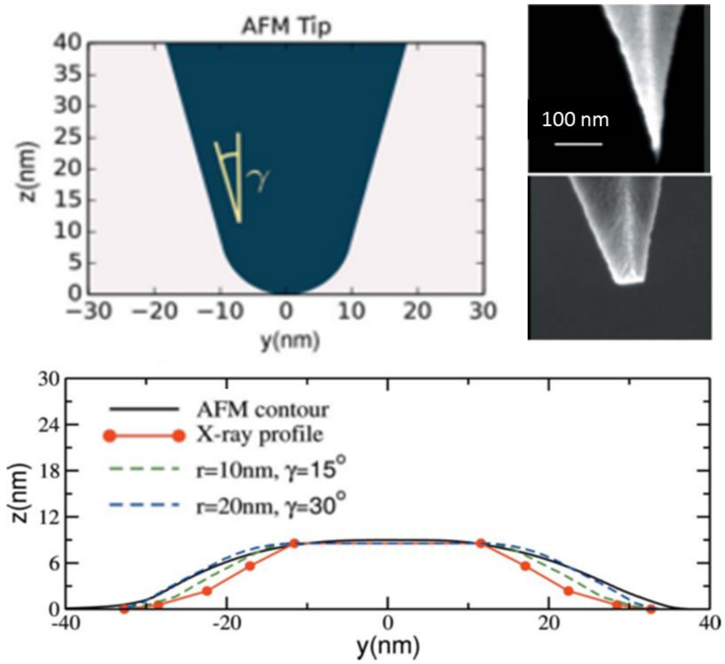

Figure 2.10. (Top)A model for the AFM tip profile and two 45°-tilted front-view SEM images on a new and a used tip. (Bottom) A quantitative comparison of the average AFM profile (Figure 2.5) with the GISAXS predictions (Figure 2.9) convoluted with two models for the AFM tip, following methods described in the literature.[40]

2.5 Conclusion

We presented a detailed analysis of the structure of polymer gratings on a hard surface with samples that present a high degree of fidelity and small line edge-roughness. Furthermore, in contrast to past studies, we analyzed our X-ray scattering data to include the intensity at the Bragg peak positions as well as the intensity between peaks along the Ewald sphere. We find that both techniques provide consistent estimates of roughness but X-ray scattering offers distinct advantages due to the large area sampled and the absence of probe artifacts present in AFM.

However, care has to be taken on scaling the individual contributions to the scattering along the GTRs given that the probed length of the gratings contributes to the intensity recorded.

The methodology presented and the agreement found between the two techniques is of paramount significance. While both can be employed to extract estimates of line-edge roughness, only GISAXS could be extended to shape analysis of buried or embedded gratings. Therefore, our results provide the foundations for further studies that will focus on examining the three-dimensional structures present in directed self-assembly processes.

2.6 References

(1) Jones, R. L.; Hu, T.; Lin, E. K.; Wu, W.-L.; Kolb, R.; Casa, D. M.; Bolton, P. J.; Barclay, G. G. *Appl. Phys. Lett.* **2003**, *83* (19), 4059–4061.

(2) Jones, R. L.; Hu, T.; Soles, C. L.; Lin, E. K.; Wu, W.; Casa, D. M.; Mahorowala, A. In *Microlithography 2004*; 2004; pp 191–198.

(3) Wang, C.; Jones, R. L.; Lin, E. K.; Wu, W.-L.; Rice, B. J.; Choi, K.-W.; Thompson, G.; Weigand, S. J.; Keane, D. T. *J. Appl. Phys.* **2007**, *102* (2), 24901.

(4) Settens, C.; Cordes, A.; Bunday, B.; Bello, A.; Kamineni, V.; Paul, A.; Fronheiser, J.; Matyi, R. *J. Micro/Nanolithography, MEMS, MOEMS* **2014**, *13* (4), 41408.

(5) Sunday, D. F.; List, S.; Chawla, J. S.; Kline, R. J. *J. Appl. Crystallogr.* **2015**, *48* (5), 1355–1363.

(6) Perera, G. M.; Wang, C.; Doxastakis, M.; Kline, R. J.; Wu, W.; Bosse, A. W.; Stein, G. E. *ACS Macro Lett.* **2012**, *1* (11), 1244–1248.

(7) Sunday, D. F.; Hammond, M. R.; Wang, C.; Wu, W.; Delongchamp, D. M.; Tjio, M.; Cheng, J. Y.; Pitera, J. W.; Kline, R. J. *ACS Nano* **2014**, *8* (8), 8426–8437.

(8) Jones, R. L.; Soles, C. L.; Lin, E. K.; Hu, W.; Reano, R. M.; Pang, S. W.; Weigand, S. J.; Keane, D. T.; Quintana, J. P. *J. Micro/Nanolithography, MEMS, MOEMS* **2006**, *5* (1), 13001.

(9) Lu, X.; Yager, K. G.; Johnston, D.; Black, C. T.; Ocko, B. M. *J. Appl. Crystallogr.* **2013**, *46* (1), 165–172.

(10) P., M.; Baumbach, T. *Phys. B Condens. Matter* **1998**, *248* (1), 381–386.

(11) P., M.; Baumbach, T. *Phys. Rev. B* **1999**, *59* (11), 7632–7643.

(12) P., M.; Jergel, M.; Baumbach, T.; Majkova, E.; Pincik, E.; Luby, S.; Ortega, L.; Tucoulou, R.; Hudek, P.; Kostic, I. *J. Phys. D Appl. Phys.* **2001**, *34* (10A), A188.

(13) Ulyanenkov, A.; Inaba, K.; P., M.; Darowski, N.; Omote, K.; Pietsch, U.; Grenzer, J.; Forchel, A. *J. Phys. D Appl. Phys.* **2001**, *34* (10A), A179.

(14) Yan, M.; Gibaud, A. *J. Appl. Crystallogr.* **2007**, *40* (6), 1050–1055.

(15) Wernecke, J.; Scholze, F.; Krumrey, M. *Rev. Sci. Instrum.* **2012**, *83* (10), 103906.

(16) Hofmann, T.; Dobisz, E.; Ocko, B. M. *J. Vac. Sci. Technol. B* **2009**, *27* (6), 3238–3243.

(17) Hlaing, H.; Lu, X.; Hofmann, T.; Yager, K. G.; Black, C. T.; Ocko, B. M. *ACS Nano* **2011**, *5* (9), 7532–7538.

(18) Soltwisch, V.; Wernecke, J.; Haase, A.; Probst, J.; Schoengen, M.; Krumrey, M.; Scholze, F. In *SPIE Advanced Lithography*; 2014; p 905012.

(19) Soltwisch, V.; Wernecke, J.; Haase, A.; Probst, J.; Schoengen, M.; Scholze, F.; Pomplun, J.; Burger, S. In *SPIE Photomask Technology*; **2014**; p 92351D--92351D.

(20) Kato, A.; Scholze, F. *Appl. Opt.* **2010**, *49* (31), 6102–6110.

(21) Gross, H.; Henn, M.-A.; Heidenreich, S.; Rathsfeld, A.; Bär, M. *Appl. Opt.* **2012**, *51* (30), 7384–7394.

(22) Kato, A.; Burger, S.; Scholze, F. *Appl. Opt.* **2012**, *51* (27), 6457–6464.

(23) Rueda, D. R.; Martin-Fabiani, I.; Soccio, M.; Alayo, N.; Perez-Murano, F.; Rebollar, E.; Garc'ia-Gutiérrez, M. C.; Castillejo, M.; Ezquerra, T. A. *J. Appl. Crystallogr.* **2012**, *45* (5), 1038–1045.

(24) Soccio, M.; Alayo, N.; Martin-Fabiani, I.; Rueda, D. R.; Garcia-Gutierrez, M. C.; Rebollar, E.; Martinez-Tong, D. E.; Perez-Murano, F.; Ezquerra, T. A. *J. Appl. Crystallogr.* **2014**, *47* (2), 0.

(25) Delgadillo, P. A. R.; Gronheid, R.; Thode, C. J.; Wu, H.; Cao, Y.; Neisser, M.; Somervell, M.; Nafus, K.; Nealey, P. F. *J. Micro/Nanolithography, MEMS, MOEMS* **2012**, *11* (3), 31302.

(26) Liu, C.; Thode, C. J.; Delgadillo, P. A. R.; Craig, G. S. W. **2011**, *29* (6), 1–6.

(27) Doxastakis, M.; Suh, H. S.; Chen, X.; Rincon Delgadillo, P. A.; Wan, L.; Williamson, L.; Jiang, Z.; Strzalka, J.; Wang, J.; Chen, W.; Ferrier, N.; Ramirez-Hernandez, A.; de Pablo, J. J.; Gronheid, R.; Nealey, P. In *SPIE Advanced Lithography*; Cain, J. P., Sanchez, M. I., Eds.; International Society for Optics and Photonics, **2015**; p 94241N.

(28) Jiang, Z.; Li, X.; Strzalka, J.; Sprung, M.; Sun, T.; Sandy, A. R.; Narayanan, S.; Lee, D. R.; Wang, J. *J. Synchrotron Radiat.* **2012**, *19* (4), 627–636.

(29) Renaud, G.; Lazzari, R.; Leroy, F. *Surf. Sci. Rep.* **2009**, *64* (8), 255–380.

(30) Parratt, L. G. *Phys. Rev.* **1954**, *95* (2), 359.

(31) Tolan, M. *X-ray scattering from soft-matter thin films: materials science and basic research*; Springer-Verlag, 1998.

(32) Mahadevapuram, N.; Strzalka, J.; Stein, G. E. *J. Polym. Sci. Part B Polym. Phys.* **2013**, *51* (7), 602–610.

(33) Kotlarchyk, M.; Chen, S.-H. *J. Chem. Phys.* **1983**, *79* (5), 2461–2469.

(34) Dagum, L.; Menon, R. *IEEE Comput. Sci. Eng.* **1998**, *5* (1), 46–55.

(35) Press, W. H.; Teukolsky, S. A.; Vetterling, W. T.; Flannery, B. P. *Numerical Recipes*, 3rd ed.; Cambridge, **2007**.

(36) Lee, S.-W.; Mittra, R. *Antennas Propagation, IEEE Trans.* **1983**, *31* (1), 99–103.

(37) Beeckman, P. A. In *IEE Proceedings H (Microwaves, Antennas and Propagation)*; **1986**; Vol. 133, pp 291–296.

(38) Chu, F.-L.; Huang, C.-F. *J. Phys. A. Math. Gen.* **1989**, *22* (14), L671.

(39) Jiang, Z.; Lee, D. R.; Narayanan, S.; Wang, J.; Sinha, S. K. *Phys. Rev. B* **2011**, *84* (7), 75440.

(40) Canet-Ferrer, J.; Coronado, E.; Forment-Aliaga, A.; Pinilla-Cienfuegos, E. *Nanotechnology* **2014**, *25* (39), 395703.

Chapter 3

Directed self-assembly of block copolymer with density multiplication for high aspect-ratio structures

3.1 Abstract

We seek the thickness limit and investigate the assembly mechanism of 3X density multiplication directed self-assembly of symmetric poly(styrene-b-methyl methacrylate) ($L_0 = 28$ nm) with increasing film thicknesses. The chemical patterns in use were fabricated in 300 mm pilot line and span a large area of 5 mm by 8 mm. Both top-down scanning electron microscopy (SEM) and grazing incidence small-angle X-ray scattering (GISAXS) are used to locally and globally characterize the long-range ordering and buried structures as a function of film thickness and thermal annealing time. With optimum boundary conditions of the chemical pattern, vertically aligned lamellar structures propagate through the film of 144 nm with a high order parameter of 0.98 within 3 hours of annealing at 250°C. In films thicker than ~ $3L_0$, as grain nucleation and growth may start independently from the free surface and patterned substrate, rotational GISAXS measurements further reveals faster defect annihilation at the film surface compared to the film bulk at a late stage of annealing.

3.2 Introduction

Block copolymer self-assembly has been considered as a promising candidate to address some grand challenges in conventional lithography and to pave the way towards new generation of low-cost, high-resolution nanopatterning technology in semiconductor industry. By integrating with traditional top-down lithography methods, highly-ordered nanostructures have shown significant promise as etch masks for the patterning of FinFET transistors,[1,2] bit-patterned media,[3,4] and contact holes[5,6] for integrated circuits. The typical block copolymer thickness in most above applications is around one to two natural periodicity ($h \sim 1\text{-}2\ L_0$) for the ease of directed assembly and subsequent pattern transfer, which could be further increased by selectively infiltrating metals into the self-assembled microdomains.[7] When the film thickness extends to submicron to micron scale, the scope of block copolymer applications is extended to such applications as separation membrane,[8] templates for nanowires and nanotubes,[9] and energy storage devices.[10] Among a variety of nanostructures that block copolymers can form, vertically aligned cylindrical and lamellar structures with high aspect ratio are of particular interest as their through-film connectivity provides continuous transport pathways ideal for these applications. Different strategies have been successfully demonstrated to achieve perpendicular orientation of high aspect-ratio microdomains, including the use of non-preferential surface treatment,[11] external electrical[12] or magnetic[13] field, solvent-vapor annealing with soft shear,[14] and liquid crystalline block copolymer system.[15] There are still concerns regarding the out-of-plane continuity of the through-film structures as well as the in-plane long-range ordering over macroscopic area.

An alternative approach is the directed self-assembly (DSA) of block copolymer on lithographically defined chemically nanopatterned surfaces that provides precise lateral ordering control of structures over micro- and macroscopic dimensions and thus better guarantees connectivity of nanostructures throughout the film. In our previous work of one-to-one DSA of PS-b-PMMA (L_0= 48 nm) on chemically-patterned substrates in thin to thick films, fully aligned lamellar structures were achieved at the top surface of 640 nm thick film (~ 13.3 L_0) and through-film vertical alignment was confirmed in 380 nm thick film (~ 7.9 L_0) with cross-section scanning electron microscopy (X-SEM). As the feature resolution in the above study is limited by the high molecular weight of block copolymer, we would like to scale down to smaller dimension enabled by DSA with density multiplication.[16] In the meantime, we complement the local information from SEM imaging with X-ray scattering to better investigate the mechanism of density multiplication assembly. Grazing incidence small-angle X-ray scattering (GISAXS) is enabled by the macroscopic line-space chemical patterns (5 mm by 8 mm) fabricated in 300 mm pilot line, providing statistical and global information of both the surface and buried structures during the DSA process.

In this work, we study the directed self-assembly of lamellae-forming PS-b-PMMA (L_0=28 nm) with 3X density multiplication on chemical patterns with a pitch (L_S) of 84 nm. We first investigate the potential for DSA to control nanostructures through varying film thicknesses from 38 nm to 178 nm upon annealing. Top-down SEM imaging and GISAXS were used to locally and globally characterize the long-range ordering and through-film structures as a function of film thickness and thermal annealing time, and highly-ordered perpendicular through-film structures were achieved with an aspect ratio of 10.3 within 3 hours at 250℃ over macroscopic patterned area. The order parameter was calculated as high as 0.98 from GISAXS measurements. When the film thickness exceeds certain critical value ~ 3 L_0, it is evident that independent grain nucleation and growth start from both the free surface and patterned substrate at the early stage of annealing. By controlling the incident angle of X-ray beam, further GISAXS measurements qualitatively and quantitatively reveal that a significant number of defect structures persist within the films even after the surface structures are perfectly aligned.

3.3 Experimental section

3.3.1 Materials

Polystyrene-b-poly(methyl-methacrylate) (PS-b-PMMA) was purchased from Polymer Source, Inc. and had a M_n, PDI and periodicity (L_0) of 18k-18k, 1.07 and ~28 nm, respectively.

Crosslinking polystyrene (XPS, AZEMBLY^{TM} NLD-128) was provided by Merck Performance Materials. Hydroxyl-terminated random copolymer brush of Poly(styrene-ran-methyl methacrylate) containing 52 mol % of PS, P(S52-r-MMA)-OH, were synthesized as described before[17].

3.3.2 Sample preparation for block copolymer assembly

The chemically-patterned substrates used in this work were fabricated on a 300 mm process line at IMEC, Belgium based on a process flow reported by our group previously[18,19]. First ~8 nm XPS thin film was spin coated on 300 mm Si wafers and annealed at 315 C for 5 min in nitrogen to be fully crosslinked. Then the wafers were coated with ~96 nm photoresist, exposed with 193 immersion lithography and developed to create line-space patterns of 84 nm pitch ($L_s = 84$ nm) over 5 mm by 8 mm area. Oxygen-containing plasma etch further trimmed the line width (W) of XPS guiding stripes with photoresist on top and removed the unprotected XPS in between. These patterned samples with alternating PS guiding stripe and exposed substrate were used as received. Hydroxyl-terminated random brush P(S52-r-MMA)-OH was spin-coated from 0.5 wt% toluene solution and yield ~25 nm thick film. The samples were then annealed at 190 C for 12 hr in vacuum to graft the hydroxyl-terminated brush onto the patterned substrate through a condensation reaction. After washing away the excess of unreacted brush by repeated sonication in toluene, a 6-7 nm thick random brush layer was backfilled in the interspatial region in between XPS guiding stripes. Next PS-b-PMMA solutions of 1-4 wt% in toluene were spin-coated onto the sample with a series of thicknesses from 38 nm to 178 nm and then baked for 30 seconds up to 3 hours at 250 °C in nitrogen. The samples were further cleaved into 4 mm by 7 mm coupons for subsequent processing and characterizations to ensure that the inspected area is completely within the 5 mm by 8 mm patterned region.

3.3.3 Film delamination

A thin layer of ~ 30 nm SiN was deposited via chemical vapor deposition onto the cleaved coupon sample, followed by 5-second slight O_2 reactive ion etch to make the surface more hydrophilic. Then graphene oxide was spin coated on from 2 wt% water solution, yielding a 5-10 nm thin layer. Concentrated poly(acrylic acid) (PAA) solution (> 35 wt% in water) was dropped onto the sample and the sample was placed in oven overnight at 60 °C for drying. The BCP film and underlying chemical pattern that adhere to PAA layer was then delaminated from the substrate by subsequent quenching in liquid nitrogen, which was flipped over to float in deionized water with the PAA side down. After PAA is completely dissolved, the free-standing film was picked up and transferred onto a bare Si wafer upside down with the underlying chemical pattern exposed to air.

3.3.4 Characterization

A Hitachi CG5000 was used to measure the line width of PS guiding stripes at IMEC before removing the photoresist on top of the guiding strips. A Carl Zeiss Merlin field-emission scanning electron microscopy (SEM) was used to image the block copolymer films. A Bruker 3A Multimode 5 AFM with tapping mode was used to image the substrate post film delamination for topographic information.

GISAXS measurement was performed at Sector 8-ID-E in the Advanced Photon Source at Argonne National Laboratory. It was taken under vacuum with an incident X-ray beam of 7.35keV ($\lambda = 0.1687\ nm^{-1}$), and sample to detector distance (SDD) is 2.165 m. The azimuthal rotational angle, Φ, was defined as the angle between incident X-ray beam and line-space pattern direction. When the incident beam is carefully aligned in parallel with the pattern, $\Phi = 0°$; when perpendicular to the pattern, $\Phi = 90°$. The incident angle, θ, of incident X-ray beam was set both below and above the critical angle of block copolymer film. Each GISAXS 2D pattern displayed here was a sum of 30 one-second exposure scans.

3.4 Results and discussion

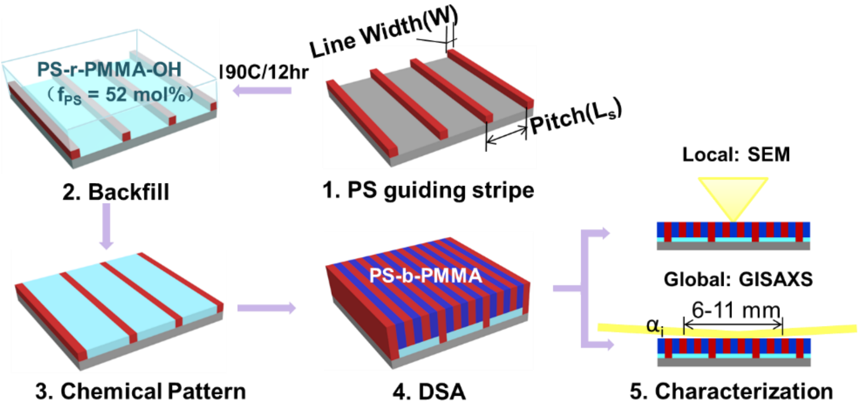

Figure 3.1. Schematic illustration of the directed self-assembly of PS-b-PMMA and its characterization with SEM and GISAXS.

The schematic in Figure 3.1 illustrates the process to direct the self-assembly of lamellae-forming PS-b-PMMA on chemically-patterned substrate and subsequent characterizations. The chemoepitaxial approach of DSA has been extensively developed for different block copolymers[16,20,21] and successfully implemented on a 300 mm production line.[19,22,23] PS guiding stripe patterns were fabricated by standardized processes at IMEC, Leuven that are described elsewhere and not reproduced here,[19,23] yielding 5 mm by 7.5 mm area of PS guiding stripe pattern with alternating cross-linked polystyrene (XPS) guiding lines (~ 8 nm thick) and exposed silicon substrate. The period of PS guiding stripes is defined as pitch, L_S, while the averaged width of each guiding stripe is line width, W. The interspatial background region in between adjacent PS guiding stripes is then grafted and functionalized in subsequent backfilling step with hydroxyl-terminated PS-r-PMMA-OH random brush of certain composition, f_{PS}. Then block copolymer films of PS-b-

PMMA (L_0 = 28 nm) with increasing thicknesses, h = 38 ~ 178 nm, are spin-coated onto the patterned substrate and then annealed in nitrogen at 250 °C for a series of time, followed by SEM and GISAXS characterizations to locally and globally investigate the extent to which the assembled structures are registered with underlying chemical patterns. The most critical advantage of this lithographically-defined chemical pattern is the individual control of its geometry and chemistry. On the one hand, the geometric condition is precisely defined in the lithography and following trim etch step. where L_s is determined by the design of the lithographic mask and W is controlled through the exposure dose and the subsequent trim etch conditions. On the other hand, the chemical condition is efficiently controlled by f_{PS} of the grafted random brush. Optimizing such key parameters of the chemical pattern as L_s,[24] W[23] and f_{PS}[25] is of critical importance to the success of DSA. In this work, the multiplication of the pattern density may be achieved by defining the L_S as a multiple of the domain spacing of the copolymer ($L_S = n \times L_0$). Here the chemical pattern has a pitch of 84 nm and the natural period of PS-b-PMMA is ~28 nm ($L_s = 3L_0$), thus enabling 3X density multiplication assembly. The line width measured before stripping the photoresist is 20 - 21 nm (W/L_0 = 0.7 ~ 0.75), and the hydroxyl-terminated PS-r-PMMA-OH random brush has a composition of f_{PS} = 52 mol%.

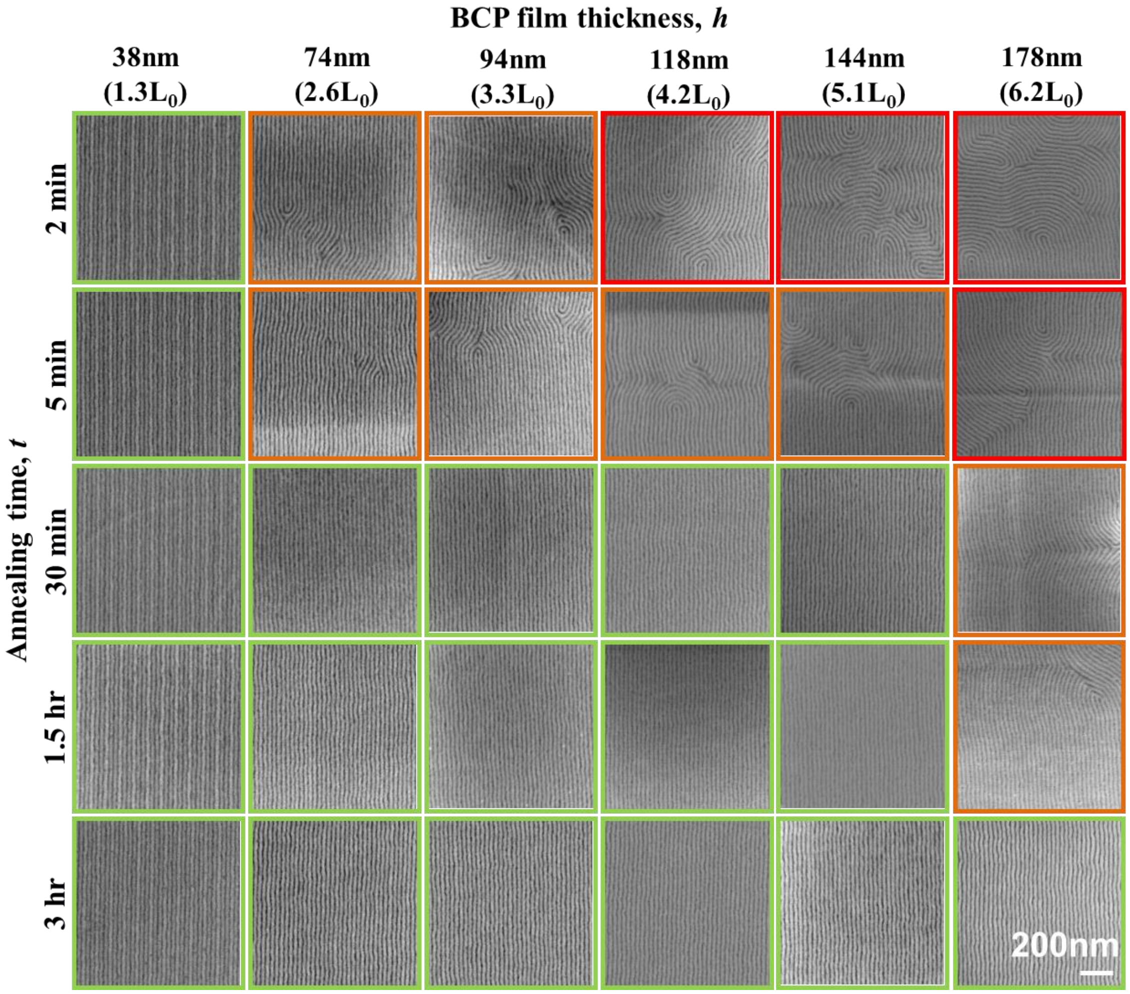

Figure 3.2. Top-down SEM images of assembled PS-b-PMMA (L_0 = 28 nm) on chemical patterns (L_S = 84 nm) over a range of film thicknesses and annealing time at 250 °C.

As shown in Figure 3.2, significantly longer annealing time is required to achieve the directed assembly of block copolymer domains as the film thickness increases. Films of various *h* (~ 1.3 L_0 – 6.2 L_0) were annealed at 250°C for times ranging from 2 min to 3 h to probe the assembly dynamics of the surface morphology of the BCP films. Multiple top-down SEM images were taken all over the 5 mm by 7.5 mm patterned area to provide local but representative information of the progress of assembly. For the thinnest film of 38 nm, BCP domains could be directed to follow underlying chemical patterns shortly within the first 2 min of annealing at 250 °C. As *h* was increased to 74 nm and 94 nm, partial alignment was observed up to 5 min with typical dislocation pair defects that Kim *et al.* previously reported in the 1:1 DSA of PS-b-PMMA (L_0 = 48 nm, h = 60 nm). In consistent with the pattern coarsening process reported in graphoepitaxy[26] and chemoepitaxy, the distance between two dislocation cores reduced both along and across the lamellae direction upon annealing from 2 min to 5 min, eventually leading to directed assembly after 30 min. When $h \geq 118$ nm, the general evolution of the surface morphology clearly followed three stages of assembly starting from random assembly of the fingerprint morphology with little sign of underlying patterns (red boarder). Upon further annealing, it evolved to guided assembly as more microdomains were aligned while a large number of defects still sustained (orange boarder), eventually leading to directed assembly with no visible defects in multiple SEM images over the patterned area (green boarder). This defect-free morphology was achieved on the surface within 30 min of annealing for films up to h = 144 nm. As h was further increased to 178 nm, random and guided assembly presented for the first 1.5 h and directed assembly was not achieved until after 3 hours of annealing at 250 °C. The time evolution of the surface morphology suggested the slower kinetics of assembly with increasing h from the following two aspects. On the one hand, the fraction of defective structures increased markedly with h at the same annealing stage. On the other hand, significantly longer annealing time was required to achieve directed assembly on the top surface of thicker films.

Since the surface energies (γ) of PS and PMMA blocks are very close at elevated temperatures,[27] the boundary conditions of the chemical pattern play a key role in determining the maximum thickness (h_{max}) that aligned structures could propagate through the film. Optimizing such geometrical and chemical parameters of the underlying pattern as L_S,[28] W and f_{PS} significantly increase this h_{max}. As longer annealing time or higher temperature may further increase the reported $h_{\max}$ of 178 nm in Figure 3.2, it is probably restricted by the density multiplication factor. Welander *et al.* reported perfect registration on the top surface of 620 nm thick film in 1:1 DSA of PS-b-PMMA (h = 620 nm, L_0 = 48 nm) with the aspect ratio of the lamellar domain doubled from what we obtained in 3X density multiplication (h = 178 nm, L_0 = 28 nm).[28] Note that other variations in the materials and annealing conditions may contribute to the variation in thickness as well. While we use the PS-b-PMMA with a smaller molecular weight (18-b-18 kg/mol) and thus presumably faster assembly kinetics under the same condition, relatively harsh annealing of 3 days at 230 °C was used in their 1:1 DSA study.

The domain orientation within a film of 118 nm demonstrates that grain nucleation and growth started independently at the top free surface and the patterned substrate. We delaminated the assembled film from the chemical pattern after 2 min of annealing and imaged both the top and bottom interfaces. As shown in Figure 3.3d, while fingerprint morphology formed at the polymer-air surface of the 118 nm thick film, the lamellar domains close to the polymer-substrate interface were already fully registered with underlying patterns. The block copolymer film was first sandwiched in between the chemical pattern and the top layers of ~30 nm SiN and 5-10 nm graphene oxide (GO) as illustrated in Figure 3.3a. Concentrated PAA solution was then dropped onto the sample and dried overnight at 60 °C, after which the sample was dipped into liquid nitrogen for film delamination. As the SiN and GO layers created adequate adhesion in between PAA and the polymer film of interest, part of the assembled film was peeled off from the patterned substrate (Figure 3.3a, part 2) while the rest stayed intact (Figure 3.3a, part 1). AFM measurement confirmed that the height of the film remaining on the substrate was ~ 120 nm as shown in Figure 3.3b-c, suggesting a complete delamination of part 2 from the chemical pattern. The peeled film was flipped over and floated on DI water with PAA side down. After PAA was fully dissolved, the free-standing film was transferred onto a piece of Si substrate for SEM imaging. As shown in Figure 3.3d, the left part reflected the structures assembled at the bottom of the film interfacing with the chemical pattern. From the magnified view with green border, we could clearly see that the lamellas were aligned perfectly at the patterned substrate after short annealing of 2 min. Note that the brighter lines of PS domains that were sparsely separated by 84 nm corresponded to the chemical pattern. In the right part of Figure 3.3d, the residual polymer on the SiN layer replicating the top surface of assembled block copolymer showed random fingerprint morphology, and agreed with the above top-down SEM image in Figure 3.2. At such thickness of 118 nm, lamellar domains at the bottom interface registered with chemical pattern underneath only after 2 min of annealing while the top grains nucleated independently and formed fingerprint at the polymer air surface owing to similar surface energy of these two blocks at 250°C.[29]

The morphology on the top surface of the film is determined by the competition in between the interaction at substrate interface and the free surface, in which the film thickness, h, plays a critical role. When $h \gg L_0$, decoupled assembly was evident by independent grain nucleation and equilibrium morphology on the polymer-air surface and substrate-polymer interface. Ji *et al.* systematically investigated the domain orientation in the self-assembly of cylinder-forming PS-b-PMMA as a function of film thickness, annealing temperature and substrate wetting, and reported that the morphology on the free surface was completely dominated by the polymer-air interaction when $h > 6\ L_0$, regardless of the wetting behavior of underlying substrate.[30] Similarly in the case of directed assembly, an increase in h from 13 L_0 to 16 L_0 resulted in the transition at the free surface from aligned lamellas to fingerprint morphology with no sign of underlying patterns.[28] Different assembly mechanism has been proposed in thinner films where h is comparable to the L_0 of forming BCP structures. Cooperative assembly was described throughout the thin film in the

DSA of PS-b-PMMA when the patterned substrate was optimized and the free surface almost equally favored both blocks, and no fingerprint morphology was observed even within short annealing.[31,32] The contrasting fingerprint and aligned morphologies on the top and bottom interfaces in Figure 3.3 reveals individual grain nucleation events across the film depth at the very beginning of annealing, but finally it is the patterned substrate that dominates the equilibrium structure on the free surface. The single grain of directed assembly propagated upwards upon further annealing, resulting in full alignment through the entire film as shown in Figure 3.2.

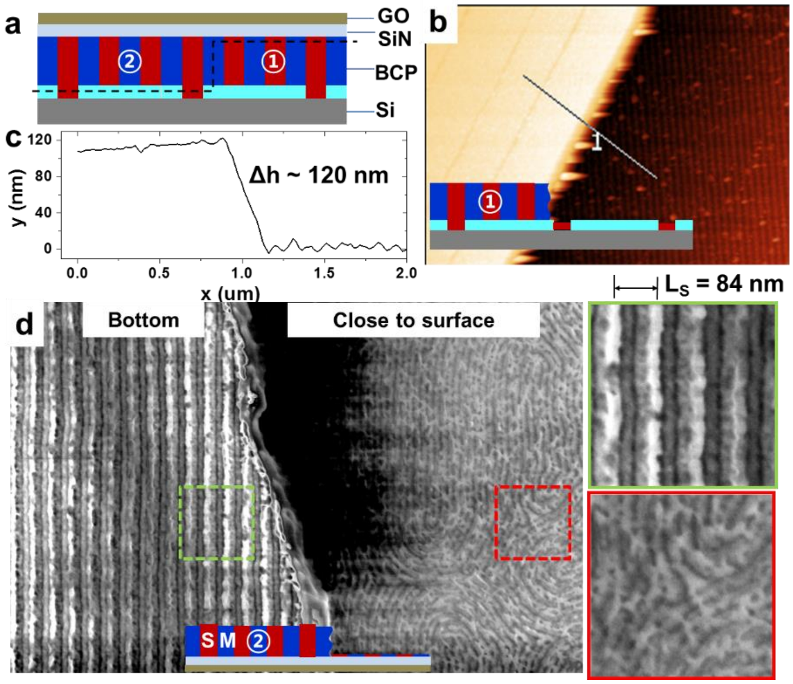

Figure 3.3. (a) Schematic illustration of the sample with the black dash line indicating the breakage from where the BCP film is delaminated from the patterned substrate. The remaining film on the substrate is noted as part 1, while the delaminated film is part 2. AFM **(b)** height image and **(c)** height profile data of the film on the substrate. **(d)** top-down SEM image of part 2 with the bottom side up. Magnified views on the right side correspond to the polymer-substrate (in green) and polymer-air (in red) interfaces of the BCP film.

As SEM imaging only provides local information on the top surface, GISAXS measurements were performed to statistically and globally evaluate the ordering of BCP structures over macroscopic patterned area and through the entire film. Figure 3.4 represents the geometry of GISAXS measurement and the incident angle of X-ray beam is α_i. The rotation angle, ϕ, is defined as the angle between the incident beam and chemical pattern direction. When the incident beam is parallel to the chemical pattern, $\phi = 0°$; and when they are in perpendicular direction, $\phi = 90°$. Simply by rotating the sample azimuthally, the orientation of the block copolymer microdomains could be easily evaluated over large area owing to the projection of X-ray beam at a shallow α_i (~5.7 cm at $\alpha_i = 0.2°$). Figure S1 presented 2D GISAXS patterns of the directed and random assembly of 35 nm BCP films ($L_0 = 28$ nm) on sparse chemical patterns ($L_S = 84$ nm) respectively. Two sets of diffraction Bragg peaks were observed at $\phi = 0°$ in both cases. The sharper and denser ones at a multiple of $q_{y,\mathrm{Patt}} = 7.47\times10^{-3}$ Å^{-1} corresponded to 84 nm from the pitch of highly-ordered chemical patterns. The BCP structures gave rise to sparser Bragg rods at every $q_{y,\mathrm{BCP}} = 2.24\times10^{-2}$ Å^{-1} that corresponded to the BCP domain spacing of 28 nm. It is the evolution of $q_{y,\mathrm{BCP}}$ upon sample rotation that distinguishes the directed from random assembly. As seen from the 2D GISAXS patterns, the intensity of $q_{y,\mathrm{BCP}}$ became significantly weaker with increasing ϕ and finally disappeared at $\phi = 90°$ for the directed assembly. Contrastingly for the random assembly, the intensity of these Bragg peaks maintained almost constant during the full rotation. Note that in both cases the chemical pattern peaks turned into an asymmetric arc of bright scattering spots once pattern and incident beam were misaligned (e.g. $\phi = 2°$), and disappeared quickly within a few degrees of rotation ($\phi < 10°$).[33] The lithographically defined chemical patterns are extremely well-ordered and have sharper interface compared to the assembled block copolymer considering the interfacial width of ~ 5 nm in between PS and PMMA blocks,[34] thus leading to the sharp reciprocal peaks.

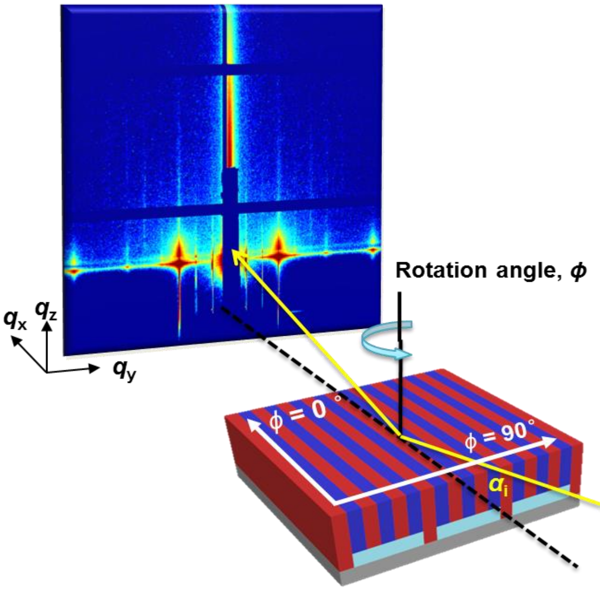

Figure 3.4. Three-dimensional illustration of rotational GISAXS measurement. α_i is the incident angle of X-ray beam, and ϕ is the rotation angle. When the incident beam is parallel to chemical pattern, ϕ = 0°. When perpendicular, ϕ = 90°. q_x, q_y and q_z are components of the scattering vector q.

We characterized the evolution of assembly using GISAXS at ϕ = 90° and probed the surface morphology and buried structures by controlling the incident angle (α_i) of the X-ray beam and thus its penetration depth into the film. When α_i is below the critical angle of polymer, α_C ($\alpha_C \approx 0.156°$ for PS-b-PMMA), the beam undergoes total external reflection and thus the X-ray penetration is confined to the surface layer of a few nanometers below polymer-air interface[35] and enables the surface analysis. When $\alpha_i > \alpha_C$, the penetration depth drastically increases over 1 μm that exceeds the film thickness, enabling full-film analysis. Figure 3.5 shows the 2D GISAXS patterns of surface and full-film analysis of 144 nm thick film at α_i = 0.1° and 0.178° respectively with the incident beam perpendicular to the chemical pattern (ϕ = 90°). In the GISAXS surface analysis (Figure 3.5b), the scattering peak of $q_y^* = 0.0224$ Å^{-1} corresponding to the BCP domain spacing of 28 nm disappeared after 30 min of annealing, thus indicating defect-free assembly on the free surface in good agreement with the top-down SEM imaging (Figure 3.5a). Meanwhile, q_y^* existed in the full-film analysis (Figure 3.5c) for up to 1.5 hr at 250°C regardless of its weaker intensity upon annealing, revealing that defects sustained much longer in the film bulk compared to at the film surface. Note that hereafter by claiming defect-free assembly we mean that the defect ratio in the total scattering volume is below the detection limit of GISAXS. Using industrial equipment and conditions, defect analysis could be more accurate counting its total number and density,[36] but this is beyond the capability and scope of our work.

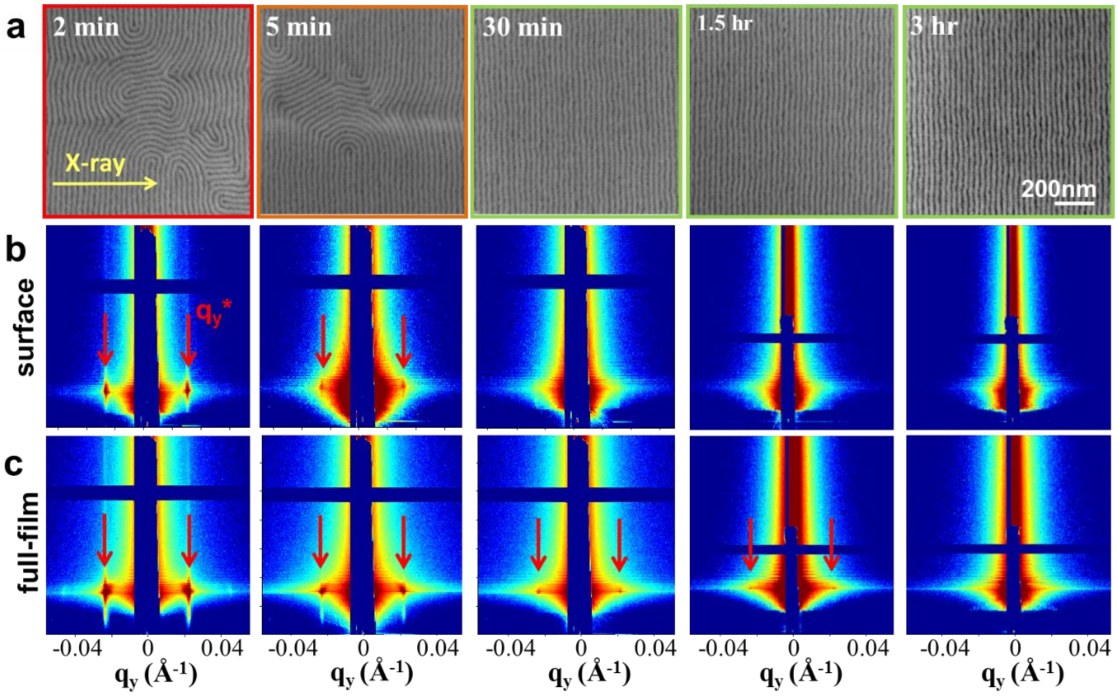

Figure 3.5. (a) Top-down SEM images of ~144 nm thick PS-b-PMMA (L_0 = 28 nm) assembled on chemical patterns of 84 nm pitch with increasing annealing time at 250°C in nitrogen. 2D GISAXS patterns at the incident angle of **(b)** 0.1° for surface analysis, and **(c)** 0.178° for full-film analysis. Bragg peak of $q_y^* = 0.0224$ Å^{-1} corresponds to the natural period of PS-b-PMMA. X-ray beam is perpendicular to direction of chemical patterns so that $\phi = 90°$ in both cases.

GISAXS inspection of samples with increasing film thicknesses from 38 nm to 144 nm ($\phi = 90°$) suggested that such discrepancy in between surface and full-film analysis only occurred in films above certain critical thickness ~ $3L_0$. As shown in Figure 3.6, a series of horizontal 1-D linecuts along the Yoneda peak in 2D GISAXS patterns were plotted as a function of q_y over a time span of thermal annealing from 30 sec to 3 h for varying film thicknesses. In all cases the defect annihilation was easily addressed by the disappearance of q_y^* upon annealing. Consistent with previous SEM results in Figure 3.2, longer time is required to annihilate the defects with increasing film thickness. In the thinnest film of 38 nm, despite that multiple SEM images failed to catch a single defect within 2 um by 2 um patterned area after the first 30 sec of annealing, both GISAXS surface and full-film analysis resolved a tiny peak from the BCP domains. As h was increased to 74 nm, defects were simultaneously detected in GISAXS surface and full-film analysis at the earlier stage of thermal annealing, and were healed later in both cases within 5 min of annealing. When $h \geq 94$ nm, defects annihilation was apparently slower in the film bulk compared to the surface of film. As q_y^* no longer existed in the surface analysis after 30 min of annealing for all the films from 94 nm to 144 nm thick, it presented in the full-film analysis for significantly longer time even up to 1.5 hr as indicated by the black arrows in Figure 3.6.

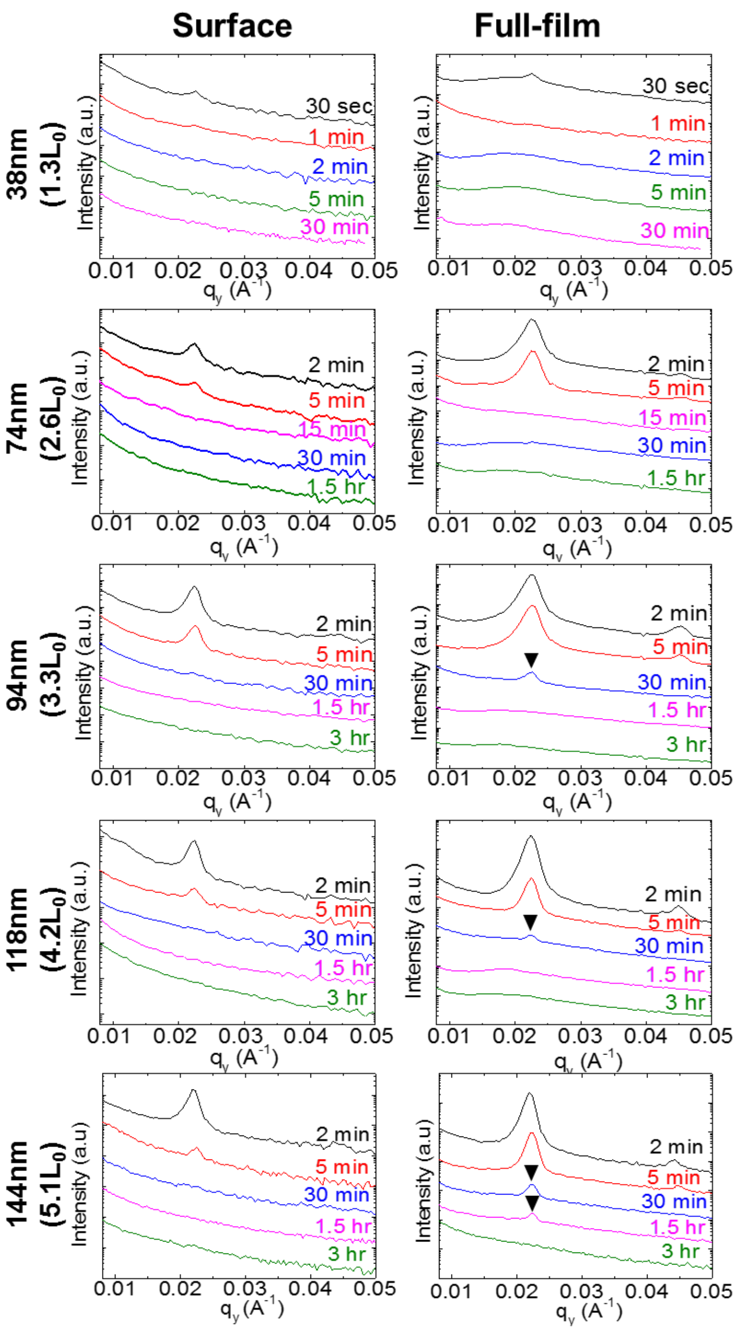

Figure 3.6. The scattering line profiles of Intensity vs. q_y at Yoneda peak for surface and full-film analysis as a function of annealing time and film thickness. All samples were annealed at 250 °C.

As the GISAXS measurements at $\phi = 90°$ provided qualitative analysis, we further quantitatively characterize the assembled structures of the 144 nm thick film on the top surface and throughout the entire film by azimuthally rotating the sample from $\phi = 0°$ to 90°. The inspected samples were annealed for 1.5 h and 3 h at 250°C. 2D GISAXS patterns and 1D horizontal linecuts of the surface and full-film analysis were plotted as a function of ϕ in Figure S2-S5 upon sample rotation. In the surface analysis (Figure S2 and S4), the disappearance of q_y^* peak well indicates the defect-free alignment on the top surface of both samples. Meanwhile in the full-film analysis, as the intensity of q_y^* peak significantly weakens with increasing ϕ, a tiny peak that indicates the remaining defects in the film bulk is resolved all the way up to $\phi = 90°$ at $t = 1.5$ h (Figure S3). Since it is already at a late annealing stage, the ratio of sustaining defects in the total scattering volume is relatively small and thus the Bragg peak of q_y^* has low intensity. We normalized the peak area at each ϕ to that at $\phi = 0°$ as $A_{\mathrm{norm}}(\phi) = A(\phi)/A(\phi = 0°)$, and plotted it as a function of ϕ in Figure 3.7 to calculate the ordering parameter, *S*. As the chemical pattern is extremely well-ordered, $\phi = 0°$ could be accurately aligned by symmetrizing the scattering spots in terms of their position and intensity at high incidence angle.[33] Although here the sample was rotated clockwise from $\phi = 0°$ to 90° (solid circles and squares), the same peak intensity is assumed upon counter-clockwise rotation of $\phi =$ 0°~ -90° on the other side (empty circles and squares). As seen from Figure 3.7a, S = 0.94 for surface analysis and S = 0.97 for full-film analysis are achieved at $t = 1.5$ h for the film of 144 nm, confirming a higher level of lateral ordering at the film surface compared to that in the entire film. Meanwhile at $t = 3$ h, the two fitting curves overlap for surface and full-film analysis, both generating a higher order parameter of S = 0.98. As the diffraction pattern turns into “ring of scattering spots” once $\phi \neq 0°$, S = 1 is expected for underlying chemical pattern. Exceptionally highly-ordered directed assembly is quantified by the ordering parameter of 0.98 throughout the film of 144 nm with an aspect ratio of ~ 10.3.

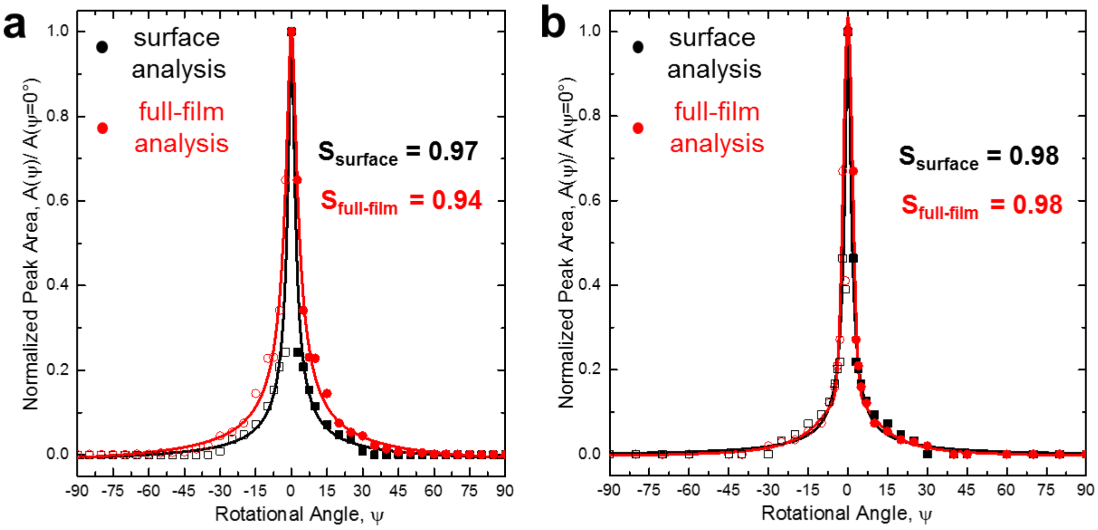

Figure 3.7. Normalized peak area for the first-order Bragg peak, q_y^*, as a function of ϕ in GISAXS surface and full-film analysis for the 144 nm thick film after **a)** 1.5 h and **b)** 3 h of annealing. The peak area at ϕ, $A(\phi)$ is normalized to that at $\phi = 0°$, A (ϕ=0°). All q_y linecuts was taken at $q_z = 0.02276$ Å^{-1}.

Faster ordering kinetics at the film surface compared to the full film has been qualitatively and quantitatively demonstrated in the GISAXS measurements, and appears to be valid above a critical thickness limit of $h > 3L_0$. This seems counterintuitive as one might expect that the underlying chemical patterns must propagate upwards into the film to align the lateral ordering of the fingerprint morphology forming from the free surface. However, they are not contradictory arguments as the discrepancy in between GISAXS surface and full-film analysis in thicker films may focus more on a later stage of the defect annihilation process. As we know that defective structures could be kinetically trapped even over a perfect pattern while most microdomains are registered with underlying pattern.[37,38] Instead of being halted by defects, the propagation of aligned structures into the film may percolate around them and continue the alignment of the coarsening grains above. While such defects exist both at the film surface and in the film bulk, their faster annihilation through lateral ordering driven by neighboring aligned structures on the surface layer might be attributed to the enhanced chain mobility on the free surface of the polymer film, which is associated with a decrease in the glass-transition temperature (T_g) compared to the bulk value due to the segregation of the chain ends to the free surface of the film.[39] The dynamics of polymers could be altered by interactions between polymer films and the neighboring substrates. Zheng *et al.* reported an increasing diffusion rate of deuterated PS in the matrix of hydrogenated PS at a greater distance away from the Si substrate.[40] While defect annihilate process is faster on the top surface of a thicker film, consistent GISAXS surface and full-film analysis in Figure 3.6 suggests that it may be cooperative through the film depth in thinner films for the following two reasons. On the one hand, the guiding chemical pattern assumes more of a role in determining the total system free energy[41] and healing existing defects. On the other hand, it is very likely that defects are through-film structures in thin films.[37] Therefore, the critical thickness limit of $h \sim 3L_0$ might be a result of the interplay between the enhanced chain mobility near the free surface and the effect of underlying chemical pattern.

3.5 Conclusion

In this work, we investigated the directed self-assembly of PS-b-PMMA (L_0 = 28 nm) with density multiplication over a wide range of film thickness up to 178 nm (~ 6.2 L_0). Films were assembled on chemical patterns (L_S = 84 nm) with optimum geometrical and chemical conditions to minimize the interfacial free energy, and significantly longer annealing time is required for the guiding of underlying pattern to propagate upwards through the film and achieve directed assembly. In thicker films above ~ 4 L_0, while the microdomains close to the bottom substrate were fully aligned within several minutes of annealing, the top surface still shows random fingerprint, thus confirming independent nucleation of grain growth from both interfaces. Further rotational GISAXS experiments also revealed a faster defect annihilation on the top surface of the film compared to the bulk when the film thickness is over a critical value, which is 94 nm (~ 3.3 L_0) in our work here.

3.6 References

(1) Tsai, H.; Pitera, J. W.; Miyazoe, H.; Bangsaruntip, S.; Engelmann, S. U.; Liu, C.-C.; Cheng, J. Y.; Bucchignano, J. J.; Klaus, D. P.; Joseph, E. A.; Sanders, D. P.; Colburn, M. E.; Guillorn, M. A. *ACS Nano* **2014**, *8* (5), 5227–5232.

(2) Tsai, H.; Miyazoe, H.; Vora, A.; Magbitang, T.; Arellano, N.; Liu, C.-C.; Maher, M. J.; Durand, W. J.; Dawes, S. J.; Bucchignano, J. J.; Gignac, L.; Sanders, D. P.; Joseph, E. A.; Colburn, M. E.; Willson, C. G.; Ellison, C. J.; Guillorn, M. A. In *Proc. SPIE*; 2016; p 977910.

(3) Ruiz, R.; Dobisz, E.; Albrecht, T. R. *ACS Nano* **2011**, *5* (1), 79–84.

(4) Albrecht, T. R.; Bedau, D.; Dobisz, E.; Gao, H.; Grobis, M.; Hellwig, O.; Kercher, D.; Lille, J.; Marinero, E.; Patel, K.; Ruiz, R.; Schabes, M. E.; Wan, L.; Weller, D. *IEEE Trans. Magn.* **2013**, *49* (2), 773–778.

(5) Bao, X.; Yi, H.; Bencher, C.; Chang, L.; Dai, H.; Chen, Y.; Chen, P. J.; Wong, H. P. In *Electron Devices Meeting (IEDM)*; 2011; p 7.7.1-7.7.4.

(6) Yi, H.; Bao, X. Y.; Zhang, J.; Bencher, C.; Chang, L. W.; Chen, X.; Tiberio, R.; Conway, J.; Dai, H.; Chen, Y.; Mitra, S.; Wong, H. S. P. *Adv. Mater.* **2012**, *24* (23), 3107–3114.

(7) Ramanathan, M.; Tseng, Y.-C.; Ariga, K.; Darling, S. B. *J. Mater. Chem. C Pages* **2013**, *1111* (21), 2050–7526.

(8) Seung, B.; Yang, Y.; Park, J.; Yoon, J.; Ree, M.; Jang, S. K.; Kim, J. K. **2008**, 1371–1377.

(9) Guarini, K.; Black, C. T.; Tuominen, M. T.; Russell, T. P. **2013**, *290* (5499), 2126–2129.

(10) Crossland, E. J. W.; Nedelcu, M.; Ducati, C.; Ludwigs, S.; Hillmyer, M. A.; Steiner, U.; Snaith, H. J. *Nano Lett.* **2009**, *9* (8), 2813–2819.

(11) Han, E.; Stuen, K. O.; Leolukman, M.; Liu, C. C.; Nealey, P. F.; Gopalan, P. *Macromolecules* **2009**, *42* (13), 4896–4901.

(12) Olszowka, V.; Kuntermann, V.; Böker, A. *Macromolecules* **2008**, *41* (15), 5515–5518.

(13) Majewski, P. W.; Gopinadhan, M.; Osuji, C. O. *J. Polym. Sci. Part B Polym. Phys.* **2012**, *50*, 2–8.

(14) Qiang, Z.; Zhang, L.; Stein, G. E.; Cavicchi, K. A.; Vogt, B. D. *Macromolecules* **2014**, *47* (3), 1109–1116.

(15) Komura, M.; Iyoda, T. *Macromolecules* **2007**, 4106–4108.

(16) Ruiz, R.; Kang, H.; Detcheverry, F. a; Dobisz, E.; Kercher, D. S.; Albrecht, T. R.; de Pablo, J. J.; Nealey, P. F. *Science* . **2008**, *321* (5891), 936–939.

(17) Han, E.; Stuen, K. O.; La, Y. H.; Nealey, P. F.; Gopalan, P. *Macromolecules* **2008**, *41* (23), 9090–9097.

(18) Liu, C. C.; Han, E.; Onses, M. S.; Thode, C. J.; Ji, S.; Gopalan, P.; Nealey, P. F. *Macromolecules* **2011**, *44* (7), 1876–1885.

(19) Delgadillo, P. A. R.; Gronheid, R.; Thode, C. J.; Wu, H.; Cao, Y.; Neisser, M.; Somervell, M.; Nafus, K.; Nealey, P. F. *J. Micro/Nanolithography, MEMS, MOEMS* **2012**, *11* (3), 31302.

(20) Xiong, S.; Wan, L.; Ishida, Y.; Chapuis, Y. A.; Craig, G. S. W.; Ruiz, R.; Nealey, P. F. *ACS Nano* **2016**, *10* (8), 7855–7865.

(21) Yang, G.-W.; Wu, G.-P.; Chen, X.; Xiong, S.; Arges, C. G.; Ji, S.; Nealey, P. F.; Lu, X.-B.; Darensbourg, D. J.; Xu, Z.-K. *Nano Lett.* **2017**, *17* (2), 1233–1239.

(22) Liu, C.; Han, E.; Onses, M. S.; Thode, C. J.; Ji, S.; Gopalan, P.; Nealey, P. F. **2011**, 1876–1885.

(23) Williamson, L. D.; Seidel, R. N.; Chen, X.; Suh, H. S.; Rincon Delgadillo, P.; Gronheid, R.; Nealey, P. F. *ACS Appl. Mater. Interfaces* **2016**, *8* (4), 2704–2712.

(24) Edwards, B. E. W.; Montague, M. F.; Solak, H. H.; Hawker, C. J.; Nealey, P. F. *Adv. Mater.* **2004**, No. 15, 1315–1319.

(25) Liu, C.; Ramirez-Hernandez, A.; Han, E.; Craig, G. S. W.; Tada, Y.; Yoshida, H.; Kang, H.; Ji, S.; Gopalan, P.; de Pablo, J. J.; Nealey, P. F. *Macrmolecules* **2013**, *46*, 1415–1424.

(26) Tong, Q.; Sibener, S. J. *Macromolecules* **2013**, *46* (21), 8538–8544.

(27) Welander, A. M.; Kang, H.; Stuen, K. O.; Solak, H. H.; Müller, M.; Pablo, J. J. De; Nealey, P. F. *Macrmolecules* **2008**, *41*, 2759–2761.

(28) Welander, A. M.; Craig, G. S. W.; Tada, Y.; Yoshida, H.; Nealey, P. F. *Macrmolecules* **2013**, *46*, 3915–3921.

(29) Mansky, P.; Russell, T.; Hawker, C.; Mays, J.; Cook, D.; Satija, S. *Phys. Rev. Lett.* **1997**, *79* (2), 237–240.

(30) Ji, S.; Liu, C. C.; Liao, W.; Fenske, A. L.; Craig, G. S. W.; Nealey, P. F. *Macromolecules* **2011**, *44* (11), 4291–4300.

(31) Edwards, E. W.; Stoykovich, M. P.; Müller, M.; Solak, H. H.; de Pablo, J. J.; Nealey, P. F. *J. Polym. Sci. Part B Polym. Phys.* **2005**, *43* (23), 3444–3459.

(32) Liu, G.; Delcambre, S. P.; Stuen, K. O.; Craig, G. S. W.; Pablo, J. J. De; Nealey, P. F. *J. Vac. Sci. Technol. B* **2010**, *28*, C6B13-C6B19.

(33) Suh, H. S.; Chen, X.; Rincon-Delgadillo, P. A.; Jiang, Z.; Strzalka, J.; Wang, J.; Chen, W.; Gronheid, R.; De Pablo, J. J.; Ferrier, N.; Doxastakis, M.; Nealey, P. F. *J. Appl. Crystallogr.* **2016**, *49*, 823–834.

(34) Anastasiadis, S. H.; Russell, T. P.; Satija, S. K.; Majkrzak, C. F. *J. Chem. Phys.* **1990**, *92* (9), 5677–5691.

(35) Levine, J. R.; Cohen, J. B.; Chung, Y. W.; Georgopoulos, P. *J. Appl. Crystallogr.* **1989**, *22* (6), 528–532.

(36) Delgadillo, P. R.; Suri, M.; Durant, S.; Cross, A.; Nagaswami, V. R.; Heuvel, D. Van Den; Gronheid, R.; Nealey, P. *J. Micro/Nanolithography, MEMS, MOEMS* **2013**, *8680*, 86800L.

(37) Nagpal, U.; Mu, M.; Nealey, P. F.; Pablo, J. J. De. *ACS Macro Lett.* **2012**, *1*, 418–422.

(38) Hur, S.-M.; Thapar, V.; Ramírez-Hernández, A.; Khaira, G.; Segal-Peretz, T.; Rincon-Delgadillo, P. A.; Li, W.; Müller, M.; Nealey, P. F.; de Pablo, J. J. *Proc. Natl. Acad. Sci.* **2015**, *112* (46), 14144–14149.

(39) Ediger, M. D.; Forrest, J. A. *Macrmolecules* **2014**, *47* (2), 471–478.

(40) Zheng, X.; Rafailovich, M.; Sokolov, J.; Strzhemechny, Y.; Schwarz, S.; Sauer, B.; Rubinstein, M. *Phys. Rev. Lett.* **1997**, *79* (2), 241–244.

(41) Doerk, G. S.; Cheng, J. Y.; Singh, G.; Rettner, C. T.; Pitera, J. W.; Balakrishnan, S.; Arellano, N.; Sanders, D. P. *Nat. Commun.* **2014**, *5*, 5805.

Chapter 4

Enabling sub-10 nm directed self-assembly of poly(styrene-b-methyl methacrylate) with ionic liquid additive

4.1 Abstract

The directed self-assembly (DSA) of block copolymers (BCPs) has been extensively developed to complement optical lithography in future nanopatterning technologies. Over the past decade, poly(styrene-b-methyl methacrylate) (PS-b-PMMA) has become one of the prototypical block copolymers applied in this field and standardized protocols for its processing have been developed. Scaling of PS-b-PMMA to pitches below 20 nm, however, is hindered by the relatively weak segregation strength between the constituent blocks as characterized by a low Flory-Huggins interaction parameter of $\chi \sim 0.036$ at 200 °C. Here we investigated the approach of adding ionic liquids (IL) into PS-b-PMMA to substantially increase the effective χ of the block copolymer, thus reducing its intrinsic resolution limit while simultaneously maintaining its favorable attributes. Criteria for the selection of IL additives were identified. We evaluated numerous candidates and highlighted that the thermal stability of the IL during annealing is essential. Using the appropriate IL, the inclusion of less than 6 vol% of the IL doubled the χ of PS-b-PMMA, while low concentrations of IL induced limited changes in the surface and interfacial properties of block copolymers, such that the chemically patterned templates developed for pure PS-b-PMMA could be used with minor adjustments for thermal annealing of the blends with a free surface. By adding ~ 3.1 vol% of the IL into a low molecular weight PS-b-PMMA (M_n = 10.3k-b-9.5k), we demonstrated DSA of lamellas with feature sizes down to 8.25 nm on chemically-patterned substrates. Compatibility of the PS-b-PMMMA/IL blends with the standardized processes and

guiding patterns that have been previously developed for block copolymer DSA suggests that such materials could replace PS-b-PMMA as a high-χ, drop-in solution for sub-10 nm lithography.

4.2 Introduction

Self-assembling block copolymers, when applied in combination with traditional optical lithography methods, have shown significant promise for the patterning of FinFET transistors,[1,2] bit-patterned media,[3,4] and contact holes[5,6] for integrated circuits. BCPs spontaneously microphase separate into periodic nanostructures with a length scale of 3 - 50 nm,[7] and the self-assembled structures can be directed to form user-defined and highly-organized morphologies on chemically[8,9] and topographically[10,11] patterned substrates with high density of features.[12] Over the past few decades, PS-b-PMMA has received the most academic and industrial interests among all BCPs for DSA applications owing to numerous reasons: the surface energy of PS and PMMA are nearly equal at the temperature of annealing,[13] random brush or mat materials are available and easily patterned for control of interfacial interactions, and the selective removal of PMMA domains offers ease of pattern transfer.[3,14] Integrated with 193 nm immersion photolithography, DSA of PS-b-PMMA has been fully implemented in 300 mm scale production cleanroom and successfully demonstrated at 14 nm half pitch with extremely low level of defects through the chemoepitaxy approach.[15,16]

The polymer physics governing the thermodynamics and kinetics of DSA process is well understood through extensive studies of PS-b-PMMA. In the case of lamellae, the chemical pre-pattern for DSA with density multiplication usually consists of alternating narrow guiding stripes and wide background regions. Directed assembly is achieved with less defects and in shorter time when key parameters of pre-pattern, including the pitch and width of guiding stripes,[17–19] the chemistry of guiding stripes and background regions,[9] are optimized to minimize the interfacial energy between the substrate and the overlaying polymer films. Unfortunately, the relatively low segregation strength between two blocks as characterized by the Flory-Huggins interaction parameter, χ (~0.036[20] at 200 °C), restricts the minimum feature above ~ 11 nm[21] (L_0 ~ 22 nm) and limits its utility for current and future technology nodes. Therefore, high-χ and low-N BCP materials, where N is the degree of polymerization, must be developed to scale down the resolution limit.[22] While the same type of underlying chemical template and the developed knowledge of DSA of PS-b-PMMA can be applied to assemble high-χ materials, most of them have considerably dissimilar surface energies and the block of lower surface energy easily segregates to the free surface during thermal annealing, which precludes the perpendicular through-film structures.

Several approaches have been established to enable perpendicular orientation for high-χ materials. The first one is to introduce a neutral top coat layer to replace the free air surface so that equal interfacial rather than surface energy is recovered. This could be accomplished by spin-coating,[23] printing,[24] or chemical vapor deposition.[25] Rather than including extra steps to apply the top coat, an alternative is to blend surface active additives that are neutral or selective with the building blocks of high-χ BCP, which segregate to the top of the film and modulate the surface/interfacial tensions at the top surface during thermal annealing.[26,27] Another approach that may involve more processing tweaks is solvent vapor annealing (SVA),[28–31] where the assembly occurs in solvated but phase separated state.[32] The presence of adequate solvent enhances the chain mobility, balances the surface energy of solvated BCP, and more importantly, maintains the recognition of chemical contrast in underlying template.[33] The last approach is to molecularly engineer pairs of monomers with high χ but similar enough surface energies.[34–38] For example, Kim *et al.* synthesized a diblock copolymer of A-b-[B-ran-C] with $\chi_{BC} > \chi_{AB} \approx \chi_{AC}$, such that $\chi_{A/B-}$

$_{\text{r-C}}$ was higher than $\chi_{\text{PS/PMMA}}$ when equivalent surface and interfacial energies could be achieved simultaneously by tuning the composition of the random block [B-ran-C].[34,39]

We would introduce a conceptually different role of the additive to increase the effective χ of PS-b-PMMA and thus scale down its resolution limit without radically changing the surface and interfacial properties. This additive is ionic liquid (IL), a type of salt composed of poorly coordinating ions and thus has low melting point below 100 °C and in many cases below room temperature. We work with selective IL additive that only goes into the polar PMMA domain, thus boosting the effective χ between the blocks. It was reported that selective ILs could induce the self-assembly of diblock and triblock copolymers into ordered microphases.[40–43] Apart from these bulk studies, Bennett *et al.* demonstrated the promoted phase separation of PS-b-PMMA in thin films by the addition of 1-ethyl-3-methylimidalzolium bis(trifluoro-methanesulfonyl)amide ([EMIM][TFSI]).[44] Therefore, the enhanced phase segregation of BCPs upon the addition of ILs may provide opportunities to enable the DSA of PS-b-PMMA below its intrinsic resolution limit using thermal annealing with a free surface, thus being more integration-friendly.

In the present work, we successfully demonstrate sub-10 nm DSA with density multiplication of PS-b-PMMA/IL blends at 300 mm wafer fabrication scale, using the same random mat and brush materials that are commercially available as well as the standard thermal annealing processes and templates as developed previously for PS-b-PMMA.[9] We first investigate the self-assembly of PS-b-PMMA/IL blends and systematically control the orientation by tuning the random brush composition to compensate the change in interfacial energies with increasing IL loading. We also point out the critical importance of thermal stability as one of primary criteria in the selection of ILs for DSA. Other factors include the capability to increase χ_{eff} with a low loading amount, the possibility of orientation control using PS-r-PMMA brush, and the compatibility with industrial fabrication processes. It is shown that by adding a small fraction of N-butyl-N-methylpyrrolidinium bis(trifluoromethylsulfonyl)imide ([BMPR][TFSI]) to a low molecular weight PS-b-PMMA that does not otherwise microphase separate, it is possible to induce phase separation and direct the forming lamellar structures having periods down to 16.5 nm. Without the necessity to tailor the chemical pattern or the process flow, smaller features are accessible below the limit of pure symmetric PS-b-PMMA. We therefore believe that PS-b-PMMA/IL blends provide a promising high-χ, drop-in replacement for PS-b-PMMA that simplifies the scaling of block copolymer DSA towards sub-10 nm resolutions.

4.3 Experimental section

4.3.1 Materials

Cross-linkable polystyrene mat (XPS), P(S-r-MMA-r-HEMA) brushes, PS-b-PMMA BCPs and ionic liquids of [BMPR][TFSI], [EMIM][TFSI] and [HMIM][PF_6] used in this study were provided by Tokyo Ohka Kogyo (TOK), Japan. Photoresist AIM5484, Orgasolv STR 301 and the organic solvent RER600 were purchased from JSR Micro, BASF and Fujifilm, respectively. All chemicals were used as received.

The XPS contained 5 mol% of vinylbenzocyclobutene (VBCB) as crosslinker, and before crosslinking had a weight-averaged molecular weight (M_w) of ~ 48 kg/mol and a polydispersity index (PDI) of 1.90. The series of P(S-r-MMA-r-HEMA) brushes used here had a styrene mole ratio ranging from 34 to 59%, with M_w and PDI values in the range of 38 – 48 kg/mol and 1.44 – 1.90, respectively. The number-averaged molecular weight (M_n) and PDI values of the three PS-b-PMMA BCPs used in this study were listed as follows: 10.3k-b-9.5k, 1.02; 14.3k-b-13.7k, 1.02; and 22.9k-b-22.9k, 1.02.

4.3.2 Sample preparation

All samples were fabricated on the 300 mm DSA process line in the production-level cleanroom at imec, Belgium. The self-assembled samples were prepared on 300 mm bare Si wafer. First, P(S-r-MMA-r-HEMA) brushes of varying styrene ratios were spin-coated from 0.5 wt% solutions, and were grafted onto the native oxide of Si substrate through a condensation reaction by 5 min annealing at 250°C in a nitrogen atmosphere. A subsequent rinse in RER 600 washed away the unreacted brush, thus yielding a 6 - 7 nm thick layer of P(S-r-MMA) to modify the substrate chemistry. Then PS-b-PMMA or PS-b-PMMA/IL blends were spin-coated from 1.00 – 1.25 wt% solutions at varying spin speeds to achieve the targeted film thickness and were annealed for various times at 200 °C in a nitrogen environment.

The chemical pre-patterns were fabricated based on a previously reported chemo-epitaxy process[9,16]. First, an antireflective layer of silicon nitride (SiN) was deposited via Chemical Vapor Deposition (CVD) to a thickness of ~13 nm on 300 mm Si wafers, on which ~8 nm of XPS was coated and crosslinked at 315°C for 5 min under nitrogen atmosphere using a TEL CLEAN TRACK LITHIUS Pro Z tool. The wafers were coated with ~95 nm of AIM5484 photoresist using a SOKUDO DUO track, exposed on an ASML 1950 immersion scanner and developed to yield line-space patterns of varying pitches (L_S = 78 - 86 nm) and line widths. Subsequently, an oxygen-based plasma etch on a LAM etcher trimmed the line widths and also removed the unprotected XPS, after which the remaining photoresist was stripped with Orgasolv STR 301 in a TEL ACT12 track. The pattern of XPS guiding stripes was coated and backfilled with P(S-r-MMA-r-HEMA) brushes using a 5 min anneal at 250°C under nitrogen. After removing the unreacted brush, films of the blended PS-b-PMMA/IL were spin-coated onto the chemical patterns and then annealed in nitrogen.

4.3.3 Characterization

Differential scanning calorimetry (DSC) measurements were performed on DSC Q2000 (TA instruments). The blends of homopolymer PS or PMMA and ionic liquid were sealed in hermetic aluminum pans. All samples were heated to 125 °C at a rate of 20 °C /min, cooled to 0 °C at a rate of 20 °C/min, and heated again to 200 °C at a rate of 2 °C/min. Data from the second heating cycle were used to determine the glass transition temperature (T_g).

All top-down scanning electron microscope (SEM) imaging was performed with a Hitachi CG5000 tool. When necessary, the PMMA domains were removed by plasma etching on TEL-Tactras etcher to enhance domain contrast for better imaging. Film thicknesses were determined with a KLA Tencor SpectraCD 100 spectroscopic ellipsometer. Wafer mass measurements to confirm ionic liquid evaporation were performed with a Metryx Mentor high precision mass metrology tool.

Grazing-incidence small-angle X-ray scattering (GISAXS) was performed at Sector 8-ID-E of the Advanced Photon Source at Argonne National Laboratory. The measurements were taken under vacuum with an incident X-ray beam of 7.35 keV ($\lambda = 0.1687$ nm), and the incidence angle was set at 0.2°. A 2D Pilatus CCD detector was used to capture the scattering patterns, and the sample to detector distance (SDD) was 0.557 m. All GISAXS spectra that are presented are the sum of 30 one-second exposures that were collected.

4.4 Results and discussion

We used the following three ionic liquid (IL) candidates in this study, N-butyl-N-methylpyrrolidinium bis(trifluoromethylsulfonyl)imide ([BMPR][TFSI]), 1-ethyl-3-methylimidazolium bis(trifluoromethylsulfonyl)imide ([EMIM][TFSI]) and 1-hexyl-3-methylimidazolium hexafluorophosphate ([HMIM][PF_6]). Figure 4.1 illustrates the chemical structures of PS-b-PMMA and the above ILs, and Table 4.1 lists the properties of PS-b-PMMA block copolymers used. All three ILs exhibited preferential solubility with PMMA rather than PS homopolymer, which was confirmed by differential scanning calorimetry (DSC) analysis (Figure B.1). The glass transition temperature (T_g) of the PMMA homopolymer decreased by 30.1 °C, 29.9 °C and 37.3 °C respectively after being mixed with [BMPR][TFSI], [EMIM][TFSI] and [HMIM][PF_6], whereas no significant changes in the T_g were measured in the PS homopolymer upon the addition of ILs. The lack of plasticization in the PS homopolymer therefore indicates that a homogeneous blend of the PS and ILs is not formed. This selective compatibility allows the IL to be incorporated only into the polar PMMA block when added to PS-b-PMMA, thus increasing the polarity of the PMMA domain and enhancing the segregation strength between the two blocks as described by the effective interaction parameter (χ_{eff}).

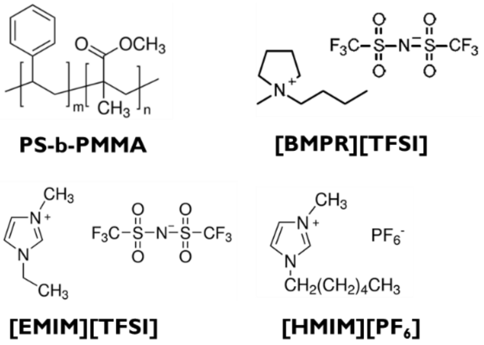

Figure 4.1. Structure of the PS-b-PMMA block copolymer and the ionic liquids.

Table 4.1. Molecular weight and composition of the PS-b-PMMA block copolymers considered in this work, as well as the morphologies into which they microphase separate.

Sample[a]	M_n of PS (kg/mol)	M_n of PMMA (kg/mol)	f_{PS}[b]	PDI	L_0[c] (nm)	Morphology[c]
SM (22.9, 22.9)	22.9	22.9	0.530	1.02	~ 24.6	lamellae
SM (14.3, 13.7)	14.3	13.7	0.540	1.02	-	disordered
SM (10.3, 9.5)	10.3	9.5	0.549	1.02	-	disordered

[a] **SM (x, y)** represents PS-*b*-PMMA where x and y are the M_n of the PS and PMMA blocks, respectively. [b] Determined using densities of ρ(PS) = 1.05 g/cm^3 and ρ(PMMA) = 1.18 g/cm^3. [c] Measured by Fast Fourier Transform (FFT) analyses of top-down SEM images of the block polymer thin films.

The wetting behavior of PS-b-PMMA/IL blends were investigated as a function of IL loading ratio and the composition of side-chain-grafted P(S-r-MMA-r-HEMA) random brushes. Thin films of PS-b-PMMA with varying IL loading ratios and thicknesses of 25 - 28 nm were coated onto a series of substrates treated with P(S-r-MMA) random brushes with increasing styrene mole ratios (f_{PS} = 34 - 59 mol%). As shown in Figure 4.2a, a relatively wide 'window' of random brushes yields perpendicular orientations (with the characteristic fingerprint structures as indicated by the green border, f_{PS} = 49 - 59 mol%) for pure PS-b-PMMA, which is consistent with previous studies.[45,46] Upon the addition of [BMPR][TFSI] up to 7.4 vol%, this window gradually but clearly shifts towards lower PS compositions (f_{PS} = 34 - 38 mol%) in the random brush. Likewise, the addition of the other two ILs of [EMIM][TFSI] (Figure B.2) and [HMIM][PF_6] (Figure B.3) exhibits similar trends. As summarized in Figure 4.2b, a higher IL content in PS-b-PMMA/IL blends requires less styrene in the random copolymer brush to maintain the perpendicular orientation. It is also observed for all three ILs that the perpendicular windows of random brush composition (Figure 4.2b, green dots) become narrower with a higher loading of the IL. There is eventually an upper limit of IL loading, beyond which perpendicular structures could not be maintained any longer. This maximum IL loading also varies with the choice of IL. For example, 7.4 vol% of [BMPR][TFSI] could be added to PS-b-PMMA and perpendicular lamellas still arise on surface treatments with f_{PS} = 34 - 38 mol%. Meanwhile, a loading ratio of [EMIM][TFSI] and [HMIM][PF_6] above 4.8 vol% and 3.3 vol% respectively result in parallel or mixed structures over a wide range of brush compositions.

These observations may result from the changes in interfacial and surface energies with increasing amount of IL in the blends. Orientation of block copolymer microdomains relative to the substrate in thin films is determined by the interfacial energy at the BCP/substrate interface,[13,46] the surface energies at the top surface,[24,47] film thickness,[48] and the morphology/architectures of the BCPs.[49,50] To achieve vertical alignment for practical patterning applications, various approaches have been developed for pure PS-b-PMMA including the addition of surfactant,[51] surface modification of the substrate via copolymer brush or mat[13,52] and self-assembled monolayers,[53,54] among which random copolymer brush of P(S-r-MMA) is recognized as a simple and robust way to control the polymer/substrate interfacial interactions. As the surface energies are very close for PS and PMMA at elevated temperatures up to 250 °C,[55,56] random brush of similar amount of styrene and methyl-methacrylate could be used to obtain perpendicular structures for symmetric PS-b-PMMA.[13,45] The shift of f_{PS} in random brush with increasing IL loading ratio could be explained by the polarity change of PMMA/IL domain. As IL additive increases the polarity of its resident PMMA block, a more polar random brush (lower f_{PS}) helps minimize the difference in interfacial energies of the PS and PMMA/IL domains with the substrate. Meanwhile, there might also be greater difference in surface energies between two blocks at the free surface upon the addition of IL ($\Delta\gamma_{\mathrm{air}} > 0$) as suggested by the narrower process window with higher IL loading and the eventual cap limit of the IL ratio in Figure 4.2b. The incorporation of IL into PMMA domain may increase the surface energy of the resident block ($\gamma_{\mathrm{M/IL}} > \gamma_{\mathrm{M}} \approx \gamma_{\mathrm{S}}$) and thus result in greater deviation of $\Delta\gamma_{\mathrm{air}}$ from 0 ($\Delta\gamma_{\mathrm{air}} = |\gamma_{\mathrm{M/IL}} - \gamma_{\mathrm{S}}| > 0$) despite that no attempt was made to directly measure the change in surface energies. The equilibrium morphology is governed by the minimization of overall free energy. As polymer chains prefer to orient parallel to the interface for the entropic bonus, perpendicular structure is energetically favored when surface/interfacial energies for both blocks are equal (*i.e.* $\Delta\gamma_{\mathrm{air}} = \Delta\gamma_{\mathrm{sub}} = 0$).[57,58] In the context of our case where $\Delta\gamma_{\mathrm{sub}}$ is minimized by fine tuning the random brush composition and $\Delta\gamma_{\mathrm{air}}$ is maintained at a moderate level by carefully controlling the loading amount of IL, there exists a range within which the gain in surface energy to form parallel wetting could not compensate for the entropy penalty due to perpendicular chain configuration to the substrate, thus making perpendicular structure (*i.e.* parallel chain configuration) more energetically favored (Figure 4.3b, green dots). Such competing effect of chain architecture and surface energy also accounts for the formation of perpendicular orientation in tri- or star-block copolymers.[59,60] Once $\Delta\gamma_{\mathrm{air}}$ becomes large enough ($\Delta\gamma_{\mathrm{air}} >> 0$) to afford the entropy cost due to higher IL loading, parallel wetting is favored and thus we are confronted with the same issue that prohibits some other high-χ materials from forming perpendicular structures via thermal annealing. Exploring more film thicknesses other than the ~1 L_0 case in Figure 4.2 might allow us to elaborate in more details on the impact of IL additive on the interfacial and surface properties of the blends, but it is beyond the scope of this work. The key concept here is that we can increase the χ_{eff} of PS-b-PMMA with a low loading of IL additive, such that perpendicular orientations can be achieved with thermal annealing at a free surface simply by minimizing the interfacial energy difference based on the composition of random brush.

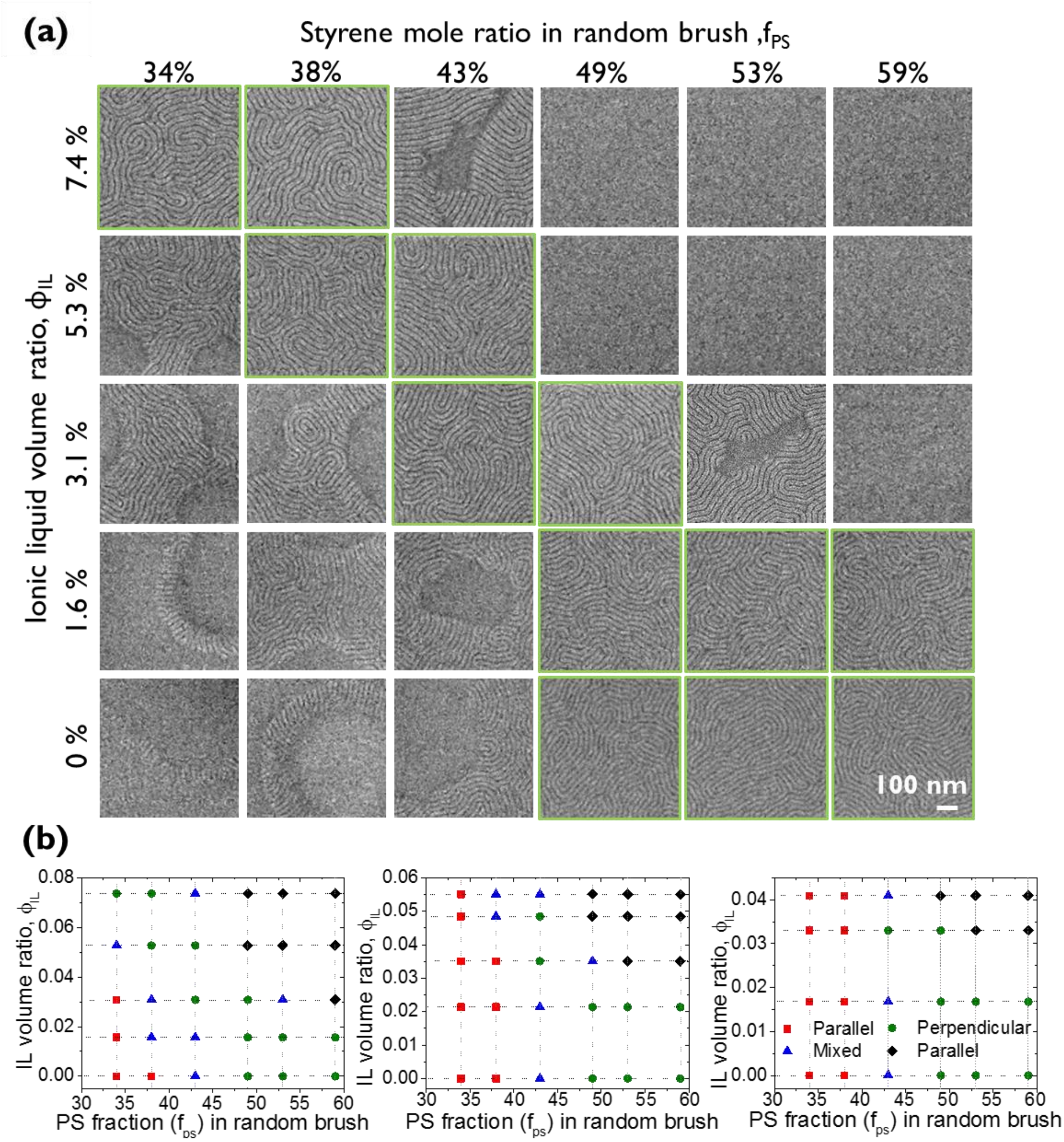

Figure 4.2. a) Top-down SEM images of SM (22.9, 22.9) and [BMPR][TFSI] blends as a function of the concentration of IL, ϕ_{IL} (reported as a volume fraction), and the PS-r-PMMA random brush composition, f_{PS} (styrene mole ratio). b) Maps of the orientation of self-assembled PS-b-PMMA in thin films when blended with [BMPR][TFSI], [EMIM][TFSI], and [HMIM][PF$_6$] from left to right. All samples had film thicknesses of 25 - 28 nm and were annealed in nitrogen at 200°C for 5 min.

A series of thin films of SM (22.9, 22.9) (L_0 ~ 24.6 nm) and IL blends with [BMPR][TFSI], [EMIM][TFSI] and [HMIM][PF_6] were prepared on random brushes of appropriate composition so as to form self-assembled perpendicularly-oriented domains in order to study the relationship between L_0 and the IL volume ratio, ϕ_{IL}, as plotted in Figure 4.3a. L_0 was measured from Fast Fourier Transform (FFT) analyses of SEM images. The L_0 of PS-b-PMMA/IL blends increased from 24.6 nm for pure PS-b-PMMA to 27.3 nm when ϕ_{IL} = 4.9 vol% for [EMIM][TFSI]. A stronger dependence of L_0 on ϕ_{IL} was observed for the other two ILs as the L_0 was increased to higher values of 28.1 nm and 27.8 nm respectively upon the addition of 4.6 vol% [BMPR][TFSI] and 4.1 vol% [HMIM][PF_6].

For block copolymers, the addition of a neutral solvent or small molecule that equally favors both blocks typically results in a decrease in the domain spacing due to the screening of unfavorable interactions between the two microphases.[61] In contrast, the addition of a selective solvent at a low volume fraction, such as the ionic liquids used here, drives a reduction in the unfavorable contacts between two domains by minimizing the interfacial area per block copolymer molecule and thereby increasing the domain spacing. The following power law dependence of domain spacing on the composition of BCP/IL blends has been shown both experimentally[62,63] and theorectically[63]:

$$L_0 \sim \phi_{\mathrm{P}}^{\alpha}$$

where ϕ_P is the volume fraction of block copolymer (ϕ_P = 1- ϕ_{IL}). The log-log plot of L_0 as a function of ϕ_P in Figure B.4 indicates that all blends exhibit an increase in L_0 with decreasing ϕ_P (*i.e.*, increasing ϕ_{IL} in Figure 4.4a). With the slope of the linear power law fits representing α, we report a qualitatively consistent but stronger dependence of L_0 on ϕ_P (α = -2.98 for [HMIM][PF_6], -2.92 for [BMPR][TFSI], and -2.04 for [EMIM][TFSI]) compared with prior work studying the phase behavior of other blends of BCPs and selective ILs.[40,42,64] Apart from the difference in materials, it is worth noting that we work with a much lower range of IL concentration, *i.e.* $0 < \phi_{\mathrm{IL}} < 0.05$, while other studies span a wider range of $0 < \phi_{\mathrm{IL}} < 0.5$ and even go through phase transitions. According to the scaling relationship of $L_0 \propto \chi^{1/6}N^{2/3}$ by assuming that the blending system is in strong segregation regime, the increase in L_0 is a result of the enhanced segregation strength upon IL addition (increasing χ_{eff}), as well as the swollen volume of the added IL in its resident block (equivalently increasing N_{eff}). The increase in N due to swollen volume of IL in PMMA domain could be easily calculated:

$$\Delta \mathrm{N} = \mathrm{N_{eff}} \text{-} \mathrm{N_{PS\text{-}PMMA}} = \frac{\mathrm{V_{IL}} \rho_{\mathrm{PMMA}}}{\mathrm{M_{MMA}}}$$

in which $\mathrm{V_{IL}}$ is the volume of IL per mole, ρ_{PMMA} is the density of PMMA and $\mathrm{M_{MMA}}$ is the molar mass of methyl methacrylate. As N_{eff} increases linearly with ϕ_{IL}, it is likely that the effect of IL additive to increase χ_{eff} and thus L_0 is more drastic at low ϕ_{IL}, and becomes less significant upon further loading. A nonlinear dependence of χ_{eff} on salt concentration was revealed in the blends of poly(styrene-b-ethylene oxide) (PS-b-PEO) and lithium bis(trifluoromethylsulfonyl)imide (LiTFSI) with a steep slope at low concentration and a plateau at high salt concentration.[65] Although no such nonlinear behavior has been investigated for ionic liquid blended copolymer system, this might be a possible explanation for the more negative α value in our case at low ϕ_{IL} than those in other literatures. Similarly, a low α value of -3.16 has also been reported at 225°C in another study of the polystyrene-b-poly(2-vinylpyridine) (PS-b-P2VP) and [Im][TFSI] blends where $0 < \phi_{\mathrm{IL}} < 0.07$.[41]

χ_{eff} is calculated from the L_0 measured above and plotted as a function of ϕ_{IL} in Figure 4.4.3b. Consistent with the above results, [HMIM][PF$_6$] and [BMPR][TFSI] have a stronger capability to increase χ_{eff} as compared to [EMIM][TFSI]. The addition of 4.5 vol% [BMPR][TFSI] increases

χ_{eff} to ~ 0.067, which has ~ 85% increase from that of PS-b-PMMA (χ ~ 0.036 at 200°C [20]) at the same annealing temperature. It should be noted that the calculated χ_{eff} represents a slight overestimation, as the pure SM (22.9, 22.9) is not in the strong segregation regime (χN ~ 16.2 at 200°C) but the intermediate one, where $L_0 \sim \chi^{\beta}$ but with a less well-defined β in the range from 1/6 to 1/5.[66] The capability of enhancing segregation strength with a lower loading of IL additive is actually one of the criteria for IL selection, as the introduction of less additive into the block copolymer system will limit potential side effects on subsequent pattern transfer processes, based on which [HMIM][TFSI] and [BMPR][TFSI] are preferred.

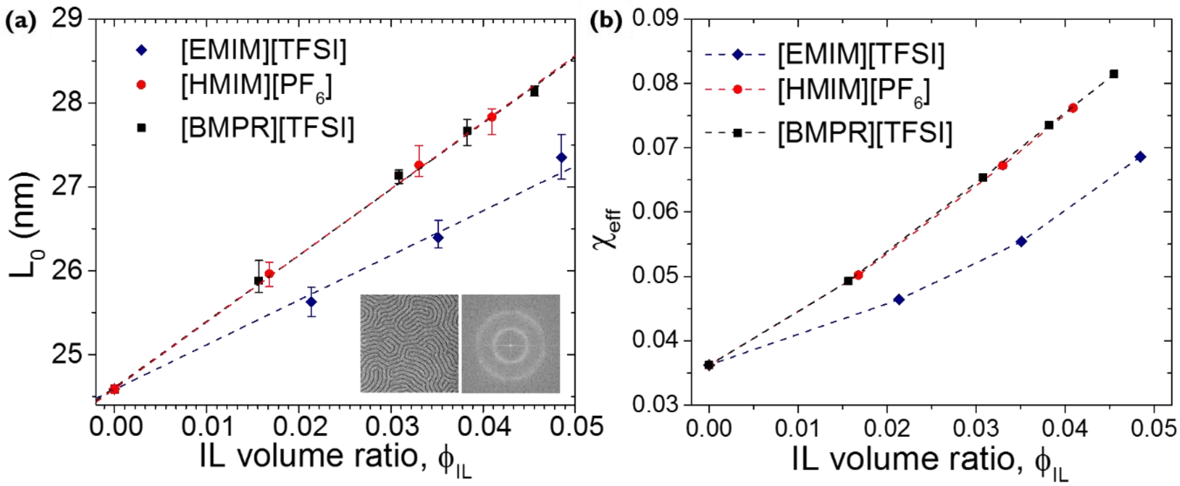

Figure 4.3. a) The lamellar period L_0 and **b)** χ_{eff} of SM (22.9, 22.9) and IL blends as a function of the concentration of IL, ϕ_{IL}. Inset are top-down SEM and corresponding 2D Fourier transformed image. L_0 was measured from Fast Fourier Transform (FFT) analyses of SEM images. All samples were annealed for 5 min at 200 °C in nitrogen.

Another criterion that must be considered is the thermal stability of PS-b-PMMA/IL blends over the typical process time of thermal annealing for directed self-assembly from several minutes to hours at elevated temperatures. We annealed SM (22.9, 22.9) blended with [BMPR][TFSI], [EMIM][TFSI] and [HMIM][PF$_6$] at 200°C for times varying from 2 to 30 min, during which the measured L_0 evolved at significantly different rates. As evident in Figure 4.4a, the blends containing [BMPR][TFSI] or [HMIM][PF_6] additives have relatively fair thermal stability, exhibiting a 1.7% and 0.7% decrease in L_0 from 2 min to 30 min, respectively. In contrast, the blends of SM (22.9, 22.9) and [EMIM][TFSI] have the L_0 reduced by 7.2% after 10 min of annealing, and almost approach the intrinsic L_0 of SM (22.9, 22.9) of 24.6 nm after 30 min of annealing. Moreover, the composition of random brush to maintain perpendicular structures also shifts towards higher styrene ratio during thermal annealing. As shown in Figure 4.4b, perpendicular lamellas of PS-b-PMMA and [EMIM][TFSI] blends are maintained on random brush of $f_{PS} = 43$ mol% up to 10 min of annealing. However, asymmetric wetting conditions arise after 30 min of annealing due to the PMMA preference of the substrate, and the perpendicular orientations may be recovered only on brushes with higher styrene concentrations such as $f_{PS} = 59$ mol%. To figure out the reason for the L_0 shrink and morphology change, we performed wafer mass measurements and revealed the loss of film mass upon annealing. Samples of pure PMMA homopolymer and PMMA blended with 20 wt% of [EMIM][TFSI] and [BMPR][TFSI] were prepared in PGMEA solution, spin coated onto 300 mm wafers, and annealed at 215°C for different times up to 30 min. As shown in Figure B.5, the blends of PMMA and [EMIM][TFSI] exhibit the greatest and most rapid loss of film mass with a 17% decrease from 0 to 30 min of annealing, which is in qualitative agreement with the results in Figure 4.4. A possible explanation for all these observations is that the IL evaporates to the environment from the thin film upon annealing. Although IL evaporation seems surprising given their reputation of having low volatility and being chemically and thermally stable, the mass loss that is observed cannot be attributed to the polymer or other small molecule contaminants, such as absorbed water, that would be present in much lower quantities[67].

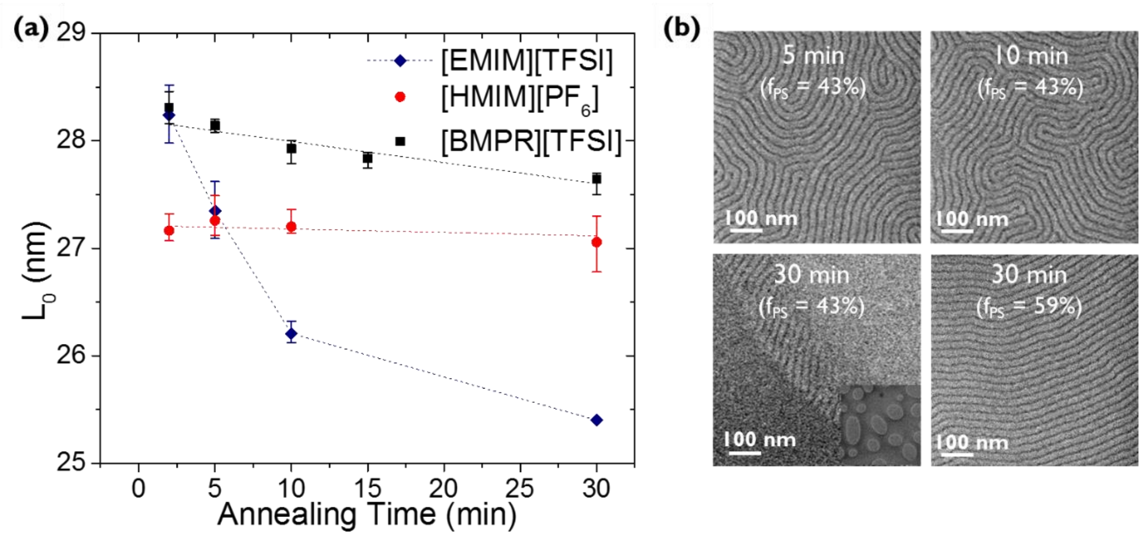

Figure 4.4. a) The lamellar period L_0 of blends of SM (22.9, 22.9) and [EMIM][TFSI] (~ 4.8 vol%), [HMIM][PF_6] (~ 3.3 vol%), and [BMPR][TFSI] (~ 4.5 vol%) as a function of annealing time at 200 °C. **b)** Top-down SEM images of blends of SM (22.9, 22.9) and [EMIM][TFSI] (~ 4.8 vol%) after 5, 10, and 30 min annealing (inset shows a low magnification SEM image, 13.5 by 13.5 um area) on a PS-r-PMMA brush with f_{PS} = 43 mol% and after 30 min anneal on a PS-r-PMMA brush with f_{PS} = 59 mol%. All samples had film thicknesses of around ~28 nm.

To investigate whether or not IL additive can induce the self-assembly of disordered PS-b-PMMA into sub-10 nm features (L_0 < 20 nm), three ILs were added into symmetric PS-b-PMMA of low molecular weight. Here we used SM (14.3,13.7) as it has a χN value corresponding to the disordered regime and thus does not exhibit any phase separated nanostructures (Figure 4.6a). Based on the knowledge of brush composition extrapolated from Figure 4.2, the blends of SM (14.3,13.7) and [BMPR][TFSI] at ϕ_{IL} = 1.6 vol% immediately self-assembled into perpendicular lamellas on the random brush layer with f_{PS} = 53% as shown in Figure 4.6b. These lamellar structures had a L_0 of ~19.3 nm as determined by FFT analysis of the SEM images. We also performed grazing incidence small-angle X-ray scattering (GISAXS, Figure 4.6c) to statistically and globally probe the structures through the entire film at an incident angle of 0.2°. The first-order diffraction peak at $q_{y,1}$ = 0.03280 Å^{-1} in Figure 4.6d reveals the perpendicular lamellas have a L_0 of ~19.2 nm that agrees with previous FFT result. The much weaker intensity of the second-order diffraction peak indicates the dimensional symmetry of the PS and IL-infused PMMA domains. Both the SEM and GISAXS results demonstrated that the addition of [BMPR][TFSI] effectively pushed the χN of pure SM (14.3,13.7) beyond the order-disorder transition point. Similarly, the addition of [EMIM][TFSI] (2.1 vol%) and [HMIM][PF$_6$] (1.5 vol%) enables the phase separation of SM (14.3,13.7) into lamellar structures of 19.2 nm and 19.4 nm in L_0 respectively as shown in Figure B.6.

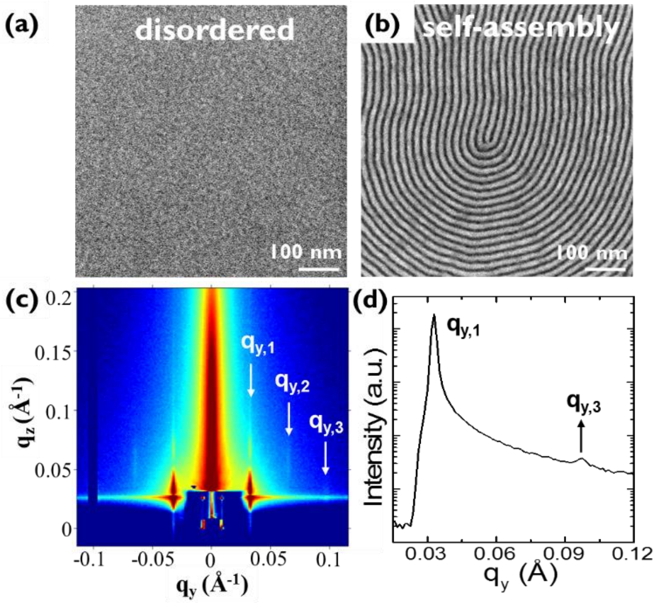

Figure 4.5. Top-down SEM images of SM (14.3,13.7) **a)** in the disordered state without ionic liquid and **b)** self-assembled into lamellae upon addition of 1.6 vol% [BMPR][TFSI] after 5 min annealing under 200°C. The PMMA domain has been removed for better contrast in the SEM. **c)** 2D GISAXS pattern and **d)** the scattering line profiles of intensity versus q_y at q_z = 0.026 Å^{-1} for the same blends imaged in b. The GISAXS incident angle was 0.2°.

To continue the studies of directed self-assembly of PS-b-PMMA/IL blends, we chose to work with [BMPR][TFSI] for the following attributes: 1) it is selectively soluble with only one block of the copolymer; 2) a small amount of IL additive substantially increases the effective χ of the BCPs; 3) a relatively wide window of compositions of the PS-r-PMMA random brush is available to control the wetting behavior of the BCP/IL blends; and 4) the BCP/IL blends have thermal stability to endure sufficient annealing at elevated temperatures as required for defect annihilation. While [HMIM][PF_6] is also qualified for these conditions, the implementation of DSA into lithographic processes in semiconductor fabrication facilities requires meticulous control of the materials themselves, and thus the integration of [HMIM][PF_6] is unfavorable because phosphorus is one of the most common silicon dopants in the semiconductor industry.

The blends of PS-b-PMMA and [BMPR][TFSI] was assembled on chemically-patterned surfaces based on the following process flow that allows the geometry and chemistry of the surface patterns to be independently controlled in distinct steps as schematized in Figure 4.6. The period of PS guide stripes is defined by the pitch L_S, while the width of the individual PS guiding stripes is given by W. This approach to DSA has been extensively developed for PS-b-PMMA[68,69] and other materials of higher χ,[38,70] and it has been successfully implemented on a 300 mm production line using tools and processes compatible with conventional fabrication[16,19,71]. Standardized fabrication processes to generate PS guiding stripes for DSA from cross-linkable polystyrene (XPS) mats are described elsewhere[9] and not reproduced in detail here. Briefly, the fabrication process includes a photolithographic patterning step followed by a trim etch step to precisely define the geometry of the line-space chemical pattern, where L_S is determined by the design of the lithographic mask and W is controlled through the exposure dose and the subsequent trim etch conditions. In the backfill step, grafting of the PS-r-PMMA random copolymer brush efficiently alters the chemistry and surface wetting behavior of the exposed substrate intermediate to the PS guiding stripes. Next we investigate how the dimensional and chemical constraints defined in the chemically patterned substrates could be satisfied simultaneously to direct the self-assembly of PS-b-PMMA/IL blends into sub-10 nm features.

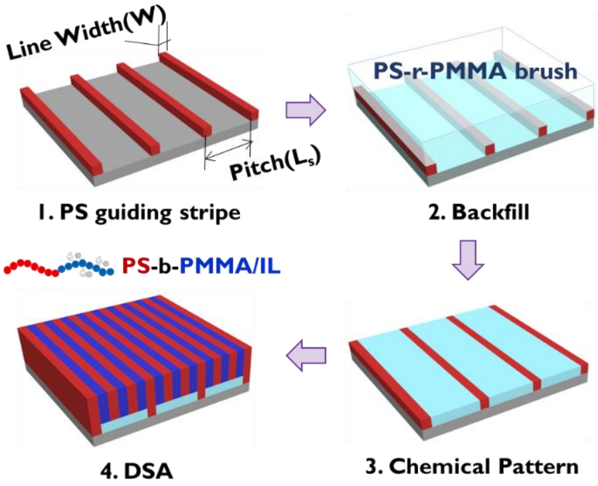

Figure 4.6. Schematic of the directed self-assembly of blends of PS-b-PMMA and IL on chemically patterned substrates.

The DSA of PS-b-PMMA/[BMPR][TFSI] blends was systematically investigated as a function of the dimensions of the chemically patterned substrates (*i.e.* L_s and W) and was found to behave similarly to the pure block copolymer, albeit accessing smaller feature resolutions. The multiplication of the pattern density may be achieved by defining the pitch of guiding patterns as a multiple of the domain spacing of the copolymer ($L_S = n \times L_0$). As shown in Figure 4.7, the 4X density multiplication DSA of SM (14.3,13.7) blended with 1.6 vol% [BMPR][TFSI] ($L_0 \approx 19.3$ nm) were tried on chemical patterns with a pitch range from 76 - 82 nm ($L_S = 3.9 - 4.2\ L_0$). When $L_s = 76$, 78, and 80 nm (3.9 – 4.1 L_0), defect-free line patterns are directed to self-assemble over large areas. When L_s is 82 nm (Figure 4.7d, $L_S/L_0 \approx 4.2$), the chemical patterns provide alignment to the block copolymer lamellae, although dislocation defects appear as highlighted with yellow circles. Meanwhile, insufficient resolution in the 193-immersion lithography technique used to fabricate the chemical surface patterns did not allow for characterization of surfaces with $L_S \leq 75$ nm. The commensurability of the period of PS-b-PMMA/IL blends with the surface patterns spans a similar range as that reported for 3X density multiplication DSA with pure PS-b-PMMA (L_0 = 28 nm, L_S = 84 nm). Another significant parameter in the chemical surface pattern is the width (W) of the crosslinked PS guide stripes. By controlling the exposure dose in the lithography step as well as the subsequent trim etch conditions, W was varied from 12 nm to 38 nm ($0.6 \leq W/L_0 \leq 2.0$) to direct the self-assembly of the PS-b-PMMA/IL blends. As shown in Figure 4.8, successful DSA was achieved over two different process windows in terms of W – a narrow range of W around 31~32 nm ($W/L_0 \sim 1.6$), and a much wider range of W from 13.8 to 21.2 nm ($0.7 \leq W/L_0 \leq 1.1$).

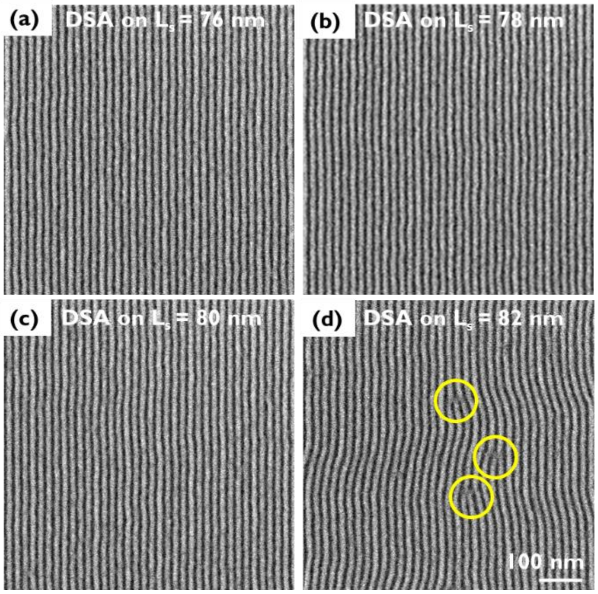

Figure 4.7. Top-down SEM images of PS-b-PMMA and [BMPR][TFSI] blends ($L_0 \sim 19.3$ nm) assembled on line-space chemical patterns of pitch **a)** L_S = 76 nm; **b)** L_S = 78 nm; **c)** L_S = 80 nm and **d)** L_S = 82 nm with 4X density multiplication. All samples were backfilled with random brush with f_{PS}= 53 mol% and annealed for 5 min at 200°C in nitrogen. The PMMA domains have been removed for better imaging contrast.

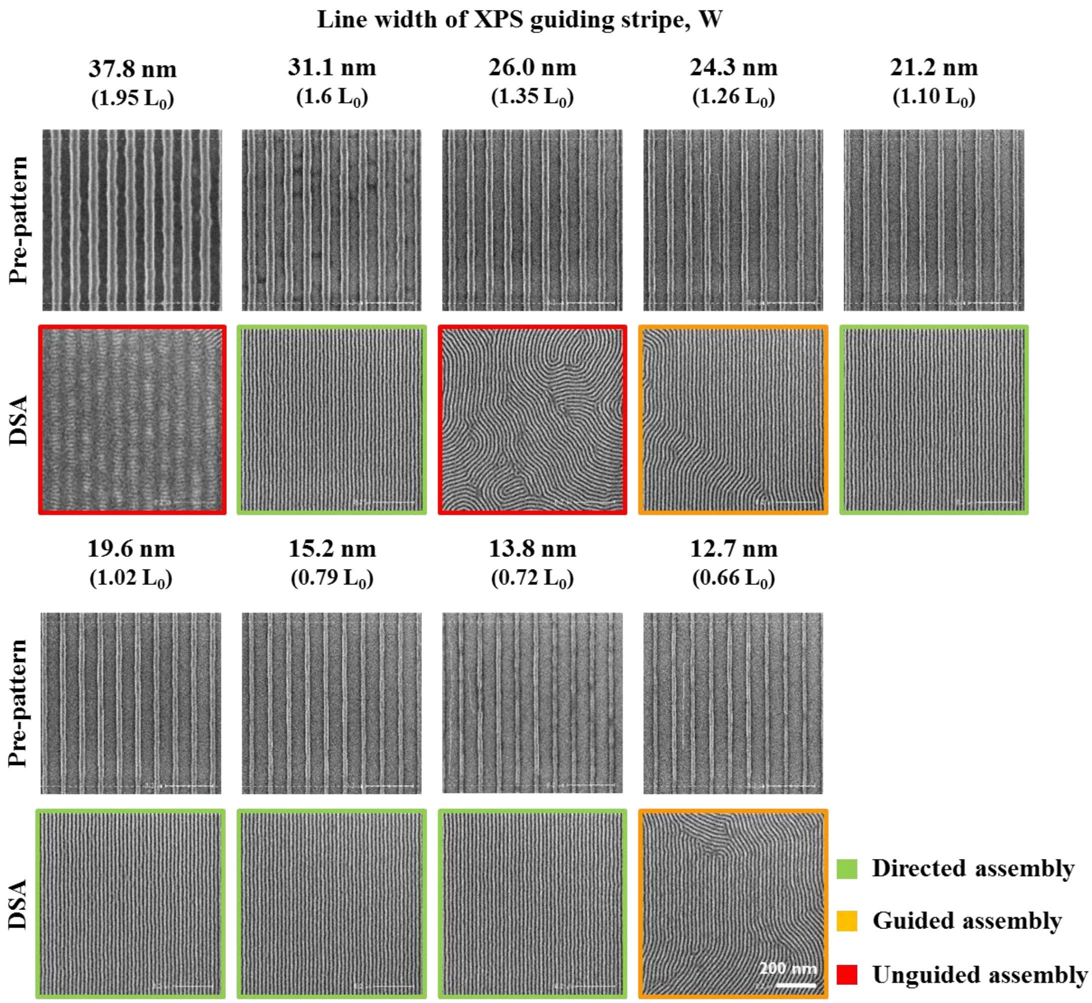

Figure 4.8. Top-down SEM images of PS-b-PMMA and [BMPR][TFSI] blends ($L_0 \approx 19.3$ nm) assembled on line-space chemical patterns with a 78 nm pitch ($L_S \approx 4\,L_0$) over a range of widths of the crosslinked PS guide stripes. All samples were backfilled with a random brush of $f_{PS} = 53$ mol% and annealed for 5 min at 200°C in nitrogen. The PMMA domains have been removed for better imaging contrast.

Although a random brush with f_{PS} = 53 mol% was backfilled between the PS guide stripes for the above results in Figure 4.7 and 8, a wider range of brush compositions exists for successful DSA. As shown in Figure B.7, random brushes of f_{PS} = 49 - 59 mol% provide similar windows of dimension commensurability. The same range of f_{PS} was used to orient perpendicular structures in self-assembly (Figure 4.2a, ϕ_{IL} = 1.6 vol%). Liu *et al.* previously reported that the f_{PS} to minimize the interfacial energy between the background region and overlying block copolymer film for directed assembly increased with the density multiplication factor and would be in general smaller than the non-preferential brush composition for self-assembly.[68] As we worked with a relatively high density multiplication factor of 4X, no significant difference was observed in the f_{PS} for the optimization of self-assembly and DSA despite that the higher $f_{PS} = 59$ mol% yielded a slightly narrower window for DSA.

We further explored the resolution limit of the PS-b-PMMA/[BMPR][TFSI] system by increasing the concentration of the IL additive (*i.e.*, tuning χ_{eff}) and decreasing the molecular weight of the block copolymer (*i.e.*, tuning N). As shown in Figure 4.9, even smaller lamellae structures of $L_0 \approx 16.5$ nm may be achieved by blending SM (10.3, 9.5) with 3.1 vol% of [BMPR][TFSI], and the 5X DSA of this blend was achieved on a chemical pattern with a pitch of 83 nm ($L_S = 5.03\ L_0$), demonstrating the possibility of such materials achieving sub-9 nm dimensions. The PS domains registered with the underlying PS guide stripes appear slightly lighter gray in the SEM image and indicate the five-fold increase in pattern density before and after DSA. An example calculation provided in the supporting information suggests that doubling χ and halving N would reduce the minimum L_0 formed by a symmetric diblock copolymer by 30%. For the PS-b-PMMA/[BMPR][TFSI] blends considered in Figures 4.7 and 4.8, the addition of 1.6 vol% of [BMPR][TFSI] into SM (14.3, 13.7) increased the effective χN from ~ 9.9 to ~13.4, thus triggering the transition from the disordered to ordered states and yielded lamellae with $L_0 \approx 19.3$ nm. Here 3.1 vol% [BMPR][TFSI] addition into SM (10.3, 9.5) increases χN from ~ 7.3 to ~ 11.7, resulting in a smaller L_0 of 16.5 nm. Adding a greater amount of IL (i.e. increasing χ) into PS-b-PMMA of lower molecular weight (i.e. decreasing N) seems a potential strategy to scale down the resolution of the PS-b-PMMA/IL blends, however, the following challenges are expected. On the on hand, the order-to-disorder transition temperature (T_{ODT}) of PS-b-PMMA is significantly decreased with a smaller molecular weight, thus requiring a much lower annealing temperature and accordingly longer annealing time for DSA.[56] For example, the annealing condition of 24 hr at 125°C is applied to achieve the assembly in Figure 4.9 at $L_0 \approx 16.5$ nm as compared to that of 5 min at 200°C in Figure 4.7 and 8 at $L_0 \approx 19.3$ nm. On the other hand, more IL additive as required to achieve a higher χ_{eff} potentially leads to greater difference in surface and interfacial properties. Meanwhile, we also observed a weaker dependence of L_0 (*i.e.* χ_{eff}) on ϕ_{IL} with a decreasing molecular weight of PS-b-PMMA as shown in Figure B.8.[42] More importantly, as χN approaches the critical ODT point, the weaker phase separation together with the smaller feature size of the blends impose additional barriers for subsequent pattern transfer. Despite the potential to scale down the resolution limit of the blending material below 16 nm in full pitch, we believe that a more practical range for the blends of PS-b-PMMA and IL additive to serve as a high-χ replacement of PS-b-PMMA would be 18 - 22 nm considering the feasibility of DSA and quality of pattern transfer.

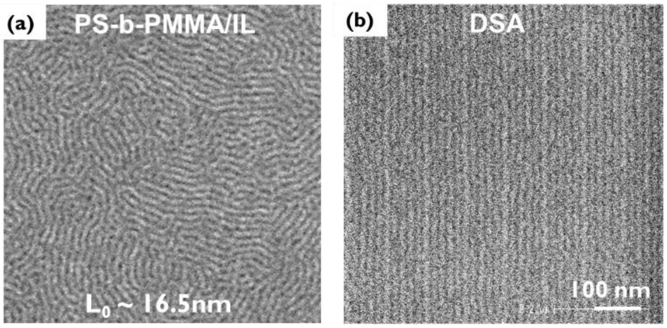

Figure 4.9. a) The self-assembly on a neutral brush ($f_{\text{PS}} = 43$ mol% because of the higher IL content in the blend) and **b)** 5X DSA on chemical patterns with 83 nm pitch ($L_S = 5.03\ L_0$) of blends of SM (10.3, 9.5) and 4 vol% [BMPR][TFSI]. The samples were annealed at 125°C for 24 hr.

4.5 Conclusion

The strategy of using ionic liquid additives to substantially increase the χ parameter of PS-b-PMMA was shown to be successful and enables the scaling of the intrinsic resolution limit of PS-b-PMMA below 10 nm ($L_0 < 20$ nm). The ionic liquid additive is selectively soluble with the more polar PMMA domain when being blended with the block copolymer, thus increasing the polarity of its resident block and enhancing the segregation strength between the two domains. Owing to the low concentration, the ionic liquid additive does not significantly change the surface and interfacial properties such that P(S-r-MMA) random brushes remain useful in controlling the interfacial interaction and thus the wetting behavior in thin films. Several additional criteria in the selection of ionic liquids to blend with BCPs for DSA were identified including a propensity to increase χ_{eff}, ability to control domain orientation using PS-r-PMMA random brushes, good thermal stability, and compatibility with industrial fabrication processes. A blend of PS-b-PMMA and [BMPR][TFSI] was therefore selected as a leading candidate and demonstrated sub-10 nm DSA on a 300 mm production line. Importantly, the DSA of this high-χ PS-b-PMMA based material with ionic liquid additive resembles that of pure PS-b-PMMA in several aspects: 1) the same chemically patterned substrates and process flow for DSA may be applied; 2) thermal annealing may be applied with a free surface for microphase separation and to facilitate defect annihilation; and 3) similar process windows of the dimensions defined on the chemically patterned surfaces (*i.e.*, L_s and W) for defect-free assembly are exhibited. Given these many attractive features of PS-b-PMMA/IL blends, we suggest that such high-χ materials are promising drop-in replacements for PS-b-PMMA to achieve sub-10 nm features in wafer-scale DSA patterning.

4.6 References

(1) Tsai, H.; Pitera, J. W.; Miyazoe, H.; Bangsaruntip, S.; Engelmann, S. U.; Liu, C.-C.; Cheng, J. Y.; Bucchignano, J. J.; Klaus, D. P.; Joseph, E. A.; Sanders, D. P.; Colburn, M. E.; Guillorn, M. A. *ACS Nano* **2014**, *8* (5), 5227–5232.

(2) Tsai, H.; Miyazoe, H.; Vora, A.; Magbitang, T.; Arellano, N.; Liu, C.-C.; Maher, M. J.; Durand, W. J.; Dawes, S. J.; Bucchignano, J. J.; Gignac, L.; Sanders, D. P.; Joseph, E. A.; Colburn, M. E.; Willson, C. G.; Ellison, C. J.; Guillorn, M. A. In *Proc. SPIE*; 2016; p 977910.

(3) Ruiz, R.; Dobisz, E.; Albrecht, T. R. *ACS Nano* **2011**, *5* (1), 79–84.

(4) Albrecht, T. R.; Bedau, D.; Dobisz, E.; Gao, H.; Grobis, M.; Hellwig, O.; Kercher, D.; Lille, J.; Marinero, E.; Patel, K.; Ruiz, R.; Schabes, M. E.; Wan, L.; Weller, D. *IEEE Trans. Magn.* **2013**, *49* (2), 773–778.

(5) Bao, X.; Yi, H.; Bencher, C.; Chang, L.; Dai, H.; Chen, Y.; Chen, P. J.; Wong, H. P. In *Electron Devices Meeting (IEDM)*; 2011; p 7.7.1-7.7.4.

(6) Yi, H.; Bao, X. Y.; Zhang, J.; Bencher, C.; Chang, L. W.; Chen, X.; Tiberio, R.; Conway, J.; Dai, H.; Chen, Y.; Mitra, S.; Wong, H. S. P. *Adv. Mater.* **2012**, *24* (23), 3107–3114.

(7) Bates, F. S.; Fredrickson, G. H. *Annu. Rev. Phys. Chern* **1990**, *41*, 525–557.

(8) Kim, S. O.; Solak, H. H.; Stoykovich, M. P.; Ferrier, N. J.; Pablo, J. J. De; Nealey, P. F. *Nature* **2003**, *424*, 411–414.

(9) Liu, C. C.; Han, E.; Onses, M. S.; Thode, C. J.; Ji, S.; Gopalan, P.; Nealey, P. F. *Macromolecules* **2011**, *44* (7), 1876–1885.

(10) Segalman, R. A.; Yokoyama, H.; Kramer, E. J. *Adv. Mater.* **2001**, *13* (15), 1152–1155.

(11) Cheng, J. Y.; Mayes, A. M.; Ross, C. A. *Nat. Mater.* **2004**, *3* (11), 823–828.

(12) Ruiz, R.; Kang, H.; Detcheverry, F. a; Dobisz, E.; Kercher, D. S.; Albrecht, T. R.; de Pablo, J. J.; Nealey, P. F. *Science* . **2008**, *321* (5891), 936–939.

(13) Mansky, P.; Liu, Y.; Huang, E.; Russell, T. P.; Hawker, C. *Science* . **1997**, *275*, 1458–1460.

(14) He, C.; Stoykovich, M. P. *Adv. Funct. Mater.* **2014**, *24* (45), 7078–7084.

(15) Liu, C.-C.; Thode, C. J.; Delgadillo, P. A. R.; Craig, G. S. W.; Gronheid, P. F. N.; Nealey, P. F.; Gronheid, R. *J. Vac. Sci. Technol. B Nanotechnol. Microelectron. Mater. Process. Meas. Phenom.* **2011**, *29*, 6–203.

(16) Delgadillo, P. A. R.; Gronheid, R.; Thode, C. J.; Wu, H.; Cao, Y.; Neisser, M.; Somervell, M.; Nafus, K.; Nealey, P. F. *J. Micro/Nanolithography, MEMS, MOEMS* **2012**, *11* (3), 31302.

(17) Edwards, B. E. W.; Montague, M. F.; Solak, H. H.; Hawker, C. J.; Nealey, P. F. *Adv. Mater.* **2004**, No. 15, 1315–1319.

(18) Edwards, E. W.; Mu, M.; Stoykovich, M. P.; Solak, H. H.; Pablo, J. J. De; Nealey, P. F. *Macrmolecules* **2007**, *40*, 90–96.

(19) Williamson, L. D.; Seidel, R. N.; Chen, X.; Suh, H. S.; Rincon Delgadillo, P.; Gronheid, R.; Nealey, P. F. *ACS Appl. Mater. Interfaces* **2016**, *8* (4), 2704–2712.

(20) Russell, T.; Jr, R. H.; Seeger, P. *Macromolecules* **1990**, *23*, 890–893.

(21) Wan, L.; Ruiz, R.; Gao, H.; Patel, K. C.; Albrecht, T. R.; Yin, J.; Kim, J.; Cao, Y.; Lin, G. *ACS Nano* **2015**, *9* (7), 7506–7514.

(22) Sinturel, C.; Bates, F. S.; Hillmyer, M. A. *ACS Macro Lett.* **2015**, *4* (9), 1044–1050.

(23) Bates, C. M.; Seshimo, T.; Maher, M. J.; Durand, W. J.; Cushen, J. D.; Dean, L. M.; Blachut, G.; Ellison, C. J.; Willson, C. G. *Science* . **2012**, *338* (6108), 775–779.

(24) Yoshida, H.; Suh, H. S.; Ramirez-Hernandez, A.; Lee, J. I.; Aida, K.; Wan, L.; Ishida, Y.; Tada, Y.; Ruiz, R.; de Pablo, J.; Nealey, P. F. *J. Photopolym. Sci. Technol.* **2013**, *26* (1), 55–58.

(25) Suh, H. S.; Kim, D. H.; Moni, P.; Xiong, S.; Ocola, L. E.; Zaluzec, N. J.; Gleason, K. K.; Nealey, P. F. *Nat. Nanotechnol.* **2017**, *12*, 575–581.

(26) Zhang, J.; Clark, M. B.; Wu, C.; Li, M.; Trefonas, P.; Hustad, P. D. *Nano Lett.* **2016**, *16* (1), 728–735.

(27) Vora, A.; Schmidt, K.; Alva, G.; Arellano, N.; Magbitang, T.; Chunder, A.; Thompson, L. E.; Lofano, E.; Pitera, J. W.; Cheng, J. Y.; Sanders, D. P. *ACS Appl. Mater. Interfaces* **2016**, *8* (43), 29808–29817.

(28) Kim, S. H.; Misner, M. J.; Xu, T.; Kimura, M.; Russell, T. P. *Adv. Mater.* **2004**, *16* (3), 226–231.

(29) Park, S.; Lee, D. H.; Xu, J.; Kim, B.; Hong, S. W.; Jeong, U.; Xu, T.; Russell, T. P. *Science* **2009**, *323* (February), 1030–1033.

(30) Gotrik, K. W.; Hannon, A. F.; Son, J. G.; Keller, B.; Alexander-Katz, A.; Ross, C. A. *ACS Nano* **2012**, *6* (9), 8052–8059.

(31) Zhang, J.; Posselt, D.; Smilgies, D.-M.; Perlich, J.; Kyriakos, K.; Jaksch, S.; Papadakis, C. M. *Macromolecules* **2014**, *47*, 5711–5718.

(32) Hur, S. M.; Khaira, G. S.; Ramírez-Hernández, A.; Müller, M.; Nealey, P. F.; De Pablo, J. J. *ACS Macro Lett.* **2015**, *4* (1), 11–15.

(33) Xiong, S.; Wan, L.; Ishida, Y.; Chapuis, Y. A.; Craig, G. S. W.; Ruiz, R.; Nealey, P. F. *ACS Nano* **2016**, *10* (8), 7855–7865.

(34) Kim, S.; Nealey, P. F.; Bates, F. S. *Nano Lett.* **2014**, *14*, 148–152.

(35) Zhou, S. X.; Janes, D. W.; Kim, C. Bin; Willson, C. G.; Ellison, C. J. *Macrmolecules* **2016**, *49*, 8332–8340.

(36) Vora, A.; Wojtecki, R. J.; Schmidt, K.; Chunder, A.; Cheng, J. Y.; Nelson, A.; Sanders, D. P. *Polym. Chem.* **2016**, *7* (4), 940–950.

(37) Seshimo, T.; Maeda, R.; Odashima, R.; Takenaka, Y.; Kawana, D.; Ohmori, K.; Hayakawa, T. *Sci. Rep.* **2016**, *6* (1), 19481.

(38) Yang, G.-W.; Wu, G.-P.; Chen, X.; Xiong, S.; Arges, C. G.; Ji, S.; Nealey, P. F.; Lu, X.-B.; Darensbourg, D. J.; Xu, Z.-K. *Nano Lett.* **2017**, *17* (2), 1233–1239.

(39) Kim, S.; Nealey, P. F.; Bates, F. S. *ACS Macro Lett.* **2012**, *1* (1), 11–14.

(40) Simone, P. M.; Lodge, T. P. *Macromolecules* **2008**, *41* (5), 1753–1759.

(41) Virgili, J. M.; Hexemer, A.; Pople, J. A.; Balsara, N. P.; Segalman, R. A. *Macromolecules* **2009**, *42* (13), 4604–4613.

(42) Bennett, T. M.; Jack, K. S.; Thurecht, K. J.; Blakey, I. *Macromolecules* **2016**, *49* (1), 205–214.

(43) Miranda, D. F.; Russell, T. P.; Watkins, J. J. *Macromolecules* **2010**, *43* (24), 10528–10535.

(44) Bennett, T. M.; Pei, K.; Cheng, H.-H.; Thurecht, K. J.; Jack, K. S.; Blakey, I. *J. Micro/Nanolithography, MEMS, MOEMS* **2014**, *13* (3), 31304.

(45) In, I.; La, Y.-H.; Park, S.-M.; Nealey, P. F.; Gopalan, P. *Langmuir* **2006**, *22* (18), 7855–7860.

(46) Han, E.; Stuen, K. O.; La, Y. H.; Nealey, P. F.; Gopalan, P. *Macromolecules* **2008**, *41* (23), 9090–9097.

(47) Bates, C. M.; Seshimo, T.; Maher, M. J.; Durand, W. J.; Cushen, J. D.; Dean, L. M.; Blachut, G.; Ellison, C. J.; Willson, C. G. *Science* **2012**, *338* (6108), 775–779.

(48) Suh, H. S.; Kang, H.; Nealey, P. F.; Char, K. *Macrmolecules* **2010**, *43*, 4744–4751.

(49) Vu, T.; Mahadevapuram, N.; Perera, G. M.; Stein, G. E. *Macromolecules* **2011**, *44* (15), 6121–6127.

(50) Lo, T.-Y.; Dehghan, A.; Georgopanos, P.; Avgeropoulos, A.; Shi, A.-C.; Ho, R.-M. *Macromolecules* **2016**, *49* (2), 624–633.

(51) Jeong, B.; Son, G.; Bulliard, X.; Kang, H.; Nealey, P. F.; Char, K. *Adv. Mater.* **2008**, *20*, 3643–3648.

(52) Ryu, D. Y.; Shin, K.; Drockenmuller, E.; Hawker, C. J.; Russel, T. P. *Science* . **2005**, *308* (5719), 236–238.

(53) Peters, R. D.; Yang, X. M.; Kim, T. K.; Nealey, P. F. *Langmuir* **2000**, *16* (24), 9620–9626.

(54) Albert, J. N. L.; Baney, M. J.; Stafford, C. M.; Kelly, J. Y.; Epps, T. H. *ACS Nano* **2009**, *3* (12), 3977–3986.

(55) Mansky, P.; Russell, T.; Hawker, C.; Mays, J.; Cook, D.; Satija, S. *Phys. Rev. Lett.* **1997**, *79* (2), 237–240.

(56) Welander, A. M.; Kang, H.; Stuen, K. O.; Solak, H. H.; Müller, M.; Pablo, J. J. De; Nealey, P. F. *Macrmolecules* **2008**, *41*, 2759–2761.

(57) Matsushita, Y.; Mori, K.; Mogi, Y.; Saguchi, R.; Noda, I.; Nagasawalc, M.; Chang, T.; Glinka, C. J.; Han, C. C. *Macromolecules* **1990**, *23*, 4317–4321.

(58) Pickett, G. T.; Witten, T. A.; Nagel, S. R. *Macromolecules* **1993**, *26*, 3194–3199.

(59) Khanna, V.; Cochran, E. W.; Hexemer, A.; Stein, G. E.; Fredrickson, G. H.; Kramer, E. J.; Li, X.; Wang, J.; Hahn, S. F. *Macromolecules* **2006**, *39*, 9346–9356.

(60) Georgopanos, P.; Lo, T.-Y.; Ho, R.-M.; Avgeropoulos, A. *Polym. Chem.* **2017**, *8*, 843.

(61) Whitmore, M. D.; Noolandi, J. *J. Chem. Phys.* **1990**, *93* (4), 2946–2955.

(62) Lai, C.; Russel, W. B.; Register, R. A. *Macromolecules* **2002**, *35* (10), 4044–4049.

(63) Hanley, K. J.; Lodge, T. P.; Huang, C. I. *Macromolecules* **2000**, *33* (16), 5918–5931.

(64) Simone, P. M.; Lodge, T. P. *ACS Appl. Mater. Interfaces* **2009**, *1* (12), 2812–2820.

(65) Teran, A. A.; Balsara, N. P. *J. Phys. Chem. B* **2014**, *118* (1), 4–17.

(66) Whitmore, M. D.; Vavasour, J. D. *Acta Polym.* **1995**, *46* (5), 341–360.

(67) Tran, C. D.; De Paoli Lacerda, S. H.; Oliveira, D. *Appl. Spectrosc.* **2003**, *57* (2), 152–157.

(68) Liu, C.; Ramirez-Hernandez, A.; Han, E.; Craig, G. S. W.; Tada, Y.; Yoshida, H.; Kang, H.; Ji, S.; Gopalan, P.; de Pablo, J. J.; Nealey, P. F. *Macrmolecules* **2013**, *46*, 1415–1424.

(69) Liu, G.; Thomas, C. S.; Craig, G. S. W.; Nealey, P. F. *Adv. Funct. Mater.* **2010**, *20*, 1251–1257.

(70) Maher, M. J.; Rettner, C. T.; Bates, C. M.; Blachut, G.; Carlson, M. C.; Durand, W. J.; Ellison, C. J.; Sanders, D. P.; Cheng, J. Y.; Willson, C. G. *ACS Appl. Mater. Interfaces* **2015**, *7* (5), 3323–3328.

(71) Liu, C.-C.; Thode, C. J.; Rincon Delgadillo, P. A.; Craig, G. S. W.; Nealey, P. F.; Gronheid, R. *J. Vac. Sci. Technol. B Microelectron. Nanom. Struct.* **2011**, *29* (6), 06F203.

Chapter 5

Impact of segregation strength increase by ionic liquid additive on the directed self-assembly of block copolymer

5.1 Abstract

Directed self-assembly (DSA) is a promising patterning strategy at the sublithographic resolution enabled by the capability of block copolymers (BCPs) to multiply the density of lithographically defined pre-pattern. As the traditional poly(styrene-b-methyl methacrylate) (PS-b-PMMA) fails to pattern sub-10 nm features due to the relatively low Flory-huggins interaction parameter, χ, "high-χ" materials are developed to achieve smaller dimension and therefore it is imperative to investigate the impact of such χ increase. Here we work with a PS-b-PMMA based high χ blends with ionic liquid (IL) additive, which selectively segregates to the polar PMMA block and thus results in a higher effective χ. Unlike most other high- χ materials consisting of other monomer pairs, the effect of χ increase could be delineated from different block chemistry owing to the low volume fraction of IL additive in the blends. IL additive of N-butyl-N-methylpyrrolidinium bis(trifluoromethylsulfonyl)imide ([BMPR][TFSI]) were added into PS-b-PMMA, and multilayers of the blends were characterized using Resonant soft X-ray refelectivity (RSoXR). It was revealed that the interfacial width of component blocks was reduced by 30% with the addition of 6 wt% [BMPR][TFSI]. We further compared the DSA of PS-b-PMMA before and after loading the same amount of IL, however, the reduction in interfacial width does not result in significant improvement in the line-edge roughness (LER) of DSA patterns after the removal of PMMA domains. While having limited impact in improving LER compared to other factors such as enhanced etch contrast, the increase in χ considerably slows down the assembly kinetics,

suggesting that great challenges awaits to implement high-χ materials to DSA applications other than the dimension scaling.

5.2 Introduction

Directed self-assembly (DSA) of block copolymer (BCP) has emerged as a complementary technology to extend the patterning capabilities beyond the resolution limit of conventional lithography.[1–3] As the leading material candidate for DSA applications over the past decades, poly(styrene-b-methyl methacrylate) (PS-b-PMMA) enjoys nearly equal surface energy[4] and sufficient etch selectivity of two component blocks,[5] however, continued scaling of its feature size is limited by the relatively low flory-huggins interaction parameter, χ (e.g. ½ $L_0 > 12$ nm for the lamellar case).[6] With ongoing demands in nanomanufacturing industry to generate sub-10 nm structures in half pitch, high-χ materials must be developed.

A great deal of research effort has been focused on the dimension scaling based on various high-χ BCPs. Several successful approaches have been adopted in order to circumvent the considerable difference in between the surface energy of building blocks that comes in hand with the higher χ value, including the application of a neutral top coat layer,[7–10] solvent vapor annealing[11–13] and synthesis of materials with blocks that have similar enough surface energies as well as a high χ.[14–16] However, the implementation of DSA to semiconductor industry poses other stringent requirements on pattern quality than the ability to access smaller feature dimension, such as line roughness and defect density, on which the impact of the enhanced segregation strength of high-χ materials still needs to be fully evaluated.

Representing the deviation from a straight edge, line edge roughness (LER) is one of the key parameters that directly determine the device performance. Previous theoretical studies predicted that the use of high χ materials could substantially improve the pattern quality in terms of LER.[17,18]

Both the interfacial width as well as the positional fluctuations in between different block domains are inversely proportional to the square root of χ.[19,20] Meanwhile, there are experimental works, though fewer, demonstrating LER improvements of high-χ materials. Tsai *et al.* showed improved mid- to low-frequency LER of an organic-organic high-χ BCP by 33% compared to PS-b-PMMA.[21] Kim *et al.* reported an extremely low LER value of ~ 0.98 nm for poly(4vinylpyridine-b-dimethylsiloxane).[22] However, as most high-χ materials adopt different chemistry and thus have varying etch selectivity from PS/PMMA, it is difficult to deconvolute the contributions of enhanced etch contrast and increased χ to the final LER reduction. For example, the incorporation of silicon results in high etch selectivity under oxygen-based reactive ion etch (RIE) conditions.[23]

Defect density is another primary concern of DSA on the trajectory towards commercialization. Not only the thermodynamic driving force but also the kinetic pathway plays a critical role towards the defect-free state.[24,25] Hur *et al.* simulated the annihilation process of dislocation pairs in the DSA of lamellar-forming BCP on chemically-patterned substrate, and revealed several kinetic barriers along the way that correspond to “bridge” transition states. As χN increases, although the increased free energy of defect formation exerts greater thermodynamic driving force of defect removal, the kinetic barrier is proportional to χN and may inhibit the annihilation process.[25] The diffusivity of BCP across the boundary interface is also calculated to decrease exponentially with the χN value.[26] With all these theoretical predictions, not much experimental observations have been made to shed light on the slower assembly kinetics induced by the higher χ value.

Recently, we demonstrated the DSA of PS-b-PMMA based high-χ material into sub-10 nm features enabled by ionic liquid (IL) additive. By controlling a low loading amount of IL additive, we remain most key attributes of PS-b-PMMA while effectively enhancing the segregation strength, thus providing an integration-friendly solution to scale down its intrinsic resolution limit for nanopatterning applications. More importantly, we are able to delineate the impact of the χ increase in this blending system as the same chemistry of PS/PMMA is maintained. In this study, we added selective IL additive of [BMPR][TFSI] into lamellae-forming PS-b-PMMA to increase the effective χ of the entire system. Based on the resonant soft X-ray reflectivity (RSoXR) measurements, we measured the interfacial width in between two component blocks as a function of the IL loading ratio. We further deconvolute the impact of χ increase on line edge roughness by analyzing the DSA patterns of PS-b-PMMA before and after blending in IL additive. Finally, a slower assembly kinetics towards defect-free state is visualized for the PS-b-PMMA/IL blending system compared to the pure block polymer.

5.3 Experimental section

5.3.1 Materials

The ionic liquid of [BMPR][TFSI], PS-b-PMMA BCPs and other infrastructure materials to make chemical patterns for directed self-assembly including cross-linkable polystyrene mat (XPS) and P(S-r-MMA-r-HEMA) random brushes used in this study were provided by Tokyo Ohka Kogyo (TOK), Japan. Photoresist AIM5484, Orgasolv STR 301 and the organic solvent RER600 were purchased from JSR Micro, BASF and Fujifilm, respectively. All chemicals were used as received.

The number-averaged molecular weight (M_n), fraction of polystyrene (f_{PS}), PDI and natural periodicity (L_0) of the three PS-b-PMMA BCPs used in this study were listed in Table 1. The XPS contained 5 mol% of vinylbenzocyclobutene (VBCB) as crosslinker, and before crosslinking had a weight-averaged molecular weight (M_w) of ~ 48 kg/mol and a polydispersity index (PDI) of 1.90. The series of P(S-r-MMA-r-HEMA) brushes used here had a styrene mole ratio ranging from 34% to 59%, with M_w and PDI values in the range of 38 – 48 kg/mol and 1.44 – 1.90, respectively.

Table 5.1. Molecular weight and composition of the PS-b-PMMA block copolymers considered in this work, as well as the morphologies into which they microphase separate.

Sample[a]	M_n of PS (Kg/mol)	M_n of PMMA (Kg/mol)	f_{PS}[b]	PDI	L_0[c] (nm)	Morphology [c]
SM(22.9, 22.9)	22.9	22.9	0.530	1.02	~ 24.6	lamellae
SM(30.4, 27.4)	30.4	27.4	0.555	1.02	~ 28	lamellae
SM(39.5, 37)	39.5	37	0.545	1.02	~ 34.3	lamellae

5.3.2 Fabrication of self-assembled, parallel-wetting and directed self-assembled samples

The self-assembled samples for infrared photoinduced force microscopy (IR-PiFM) were prepared on 300 mm bare Si wafer. First, P(S-r-MMA-r-HEMA) brushes of varying styrene ratios were spin-coated from 0.5 wt% solutions, and were grafted onto the native oxide of Si substrate through a condensation reaction by 5 min annealing at 250°C in a nitrogen atmosphere. A subsequent rinse in RER 600 washed away the unreacted brush, thus yielding a 6 – 7 nm thick layer of P(S-r-MMA) to modify the substrate chemistry. Then SM (39.5, 37) or SM (39.5, 37)/[BMPR][TFSI] blends (ϕ_{IL} = 10 wt%) were spin-coated from 1.00 - 1.25 wt% solutions at varying spin speeds to achieve the targeted film thickness ~ 1 L_0 and were annealed for 5 min at 200 °C in a nitrogen environment.

The parallel-wetting samples for resonant soft X-ray reflectivity (RSoXR) measurements were prepared on piranha cleaned Si substrate. Pure SM (22.9, 22.9) and that blended with 4 - 10 wt% [BMPR][TFSI] were spin coated from 4 - 4.2 wt% solutions, and the film thickness was accurately controlled ~ 5.5 L_0 by varying the spin speed so that parallel structures formed owing to the asymmetric wetting at the free and substrate interfaces, which were confirmed by optical microscopy and top-down SEM. Homopolymer PS and PMMA/[BMPR][TFSI] blends (ϕ_{IL} = 10 -

20 wt%) with a thickness > 100 nm as well as bare Si substrate were prepared as reference samples. All samples were annealed for 10 min at 200 °C in a nitrogen environment.

The directed self-assembled samples for roughness measurements were fabricated on the 300 mm DSA process line in the production-level cleanroom at imec, Belgium. The chemical pre-patterns were fabricated based on a previously reported chemo-epitaxy process[27,28] First, an antireflective layer of silicon nitride (SiN) was deposited via chemical vapor deposition (CVD) to a thickness of ~13 nm on 300 mm Si wafers, on which ~8 nm of XPS was coated and crosslinked at 315°C for 5 min under nitrogen atmosphere using a TEL CLEAN TRACK LITHIUS Pro Z tool. The wafers were coated with ~95 nm of AIM5484 photoresist using a SOKUDO DUO track, exposed on an ASML 1950 immersion scanner and developed to yield line-space patterns of varying pitches (L_S = 78 - 86 nm) and line widths. Subsequently, an oxygen-based plasma etch on a Lam etcher trimmed the line widths and also removed the unprotected XPS, after which the remaining photoresist was stripped with Orgasolv STR 301 in a TEL ACT12 track. The pattern of XPS guiding stripes was coated and backfilled with P(S-r-MMA-r-HEMA) brushes using a 5 min anneal at 250°C under nitrogen. After removing the unreacted brush, films of pure SM (22.9, 22.9) and the blends of SM (22.9, 22.9) and [BMPR][TFSI] (ϕ_{IL} = 8 wt%) were spin-coated onto the chemical patterns and then annealed for 30 min at 215 °C in nitrogen. PMMA domains were removed by dry etching on TEL TACTRAS etcher.

5.3.3 Photoinduced force microscopy

A VistaScope microscope from Molecular Vista Inc. was coupled to a LaserTune QCL product with a wavenumber resolution of 0.5 cm^{-1} and a tuning range from 800 to 1800cm^{-1} from Block Engineering. The microscope was operated in dynamic mode, with NCH-Au 300 kHz noncontact cantilevers from Nanosensors.

5.3.4 Resonant soft X-ray reflectivity (RSoXR) measurements

RSoXR measurements were performed at the Advanced Light Source (ALS) at the Lawrence Berkeley National Laboratory using beamline 6.3.2. Measurements at the carbon edge (260 eV-300 eV) were conducted using a 600 mm^{-1} grating, a 600 nm Ti filter and a Burle CEM detector.[29] Measurements at the oxygen edge (520 eV-540 eV) were conducted using a 1200 mm^{-1} grating, a Cr filter and the Burle CEM detector. The data was fit using the Refl1D program and uncertainties determined using the differential evolution adaptive metropolis (DREAM) algorithm.

5.4 Results and discussion

We work with [BMPR][TFSI] ionic liquid, which is selectively soluble with the more polar PMMA domain in PS-b-PMMA block copolymer. This selective solubility could be directly visualized by infrared photoinduced force microscopy (IR-PiFM). As an emerging scanning probe technique, PiFM has demonstrated the capability to map chemical information with the morphology of self-assembled block copolymer with a spatial resolution < 10 nm by imaging at multiple IR wavelengths corresponding to absorption peaks of different chemical species.[30] While the resonance peaks of PS and PMMA were known as 1493 cm^{-1} and 1733 cm^{-1} from PiFM spectra in ref 30, 1057 cm^{-1} was chosen as the characteristic adsorption peak for [BMPR][TFSI] according to the FTIR spectra in Figure C.1. Lamellae-forming SM (39.5, 37) with a L_0 of 34.3 nm and a thickness of 34 nm self-assembled into fingerprint morphology on the non-preferential substrate grafted with a PS-r-PMMA random brush of f_{PS} = 53 mol%. Owing to the effective χ increase by blending in [BMPR][TFSI] at a weight ratio of ϕ_{IL} = 10 wt%, the L_0 increased from the intrinsic value of 34.3 nm to 41.3 nm as measured from Fast Fourier Transform analysis of top-down SEM images in Figure C.2, while the random brush underlayer shifted to f_{PS} = 38 mol%. The pristine SM (39.5, 37) was first imaged at the IL peak of 1057 cm^{-1}, showing almost no sign of the lamellar structures (Figure 5.2a). Then PiFM images were acquired for the blends of SM (39.5, 37) and [BMPR][TFSI] at the wavenumber of 1057 cm^{-1}, 1493 cm^{-1} and 1733 cm^{-1} in Figure 5.1b-d, thus highlighting the IL-containing, PS and PMMA domains respectively. It is evident that [BMPR][TFSI] is solely incorporated into the PMMA but not PS domain from the consistence in between Figure 5.1b and 5.1d as well as the reverse tone of Figure 5.1b and 5.1c.

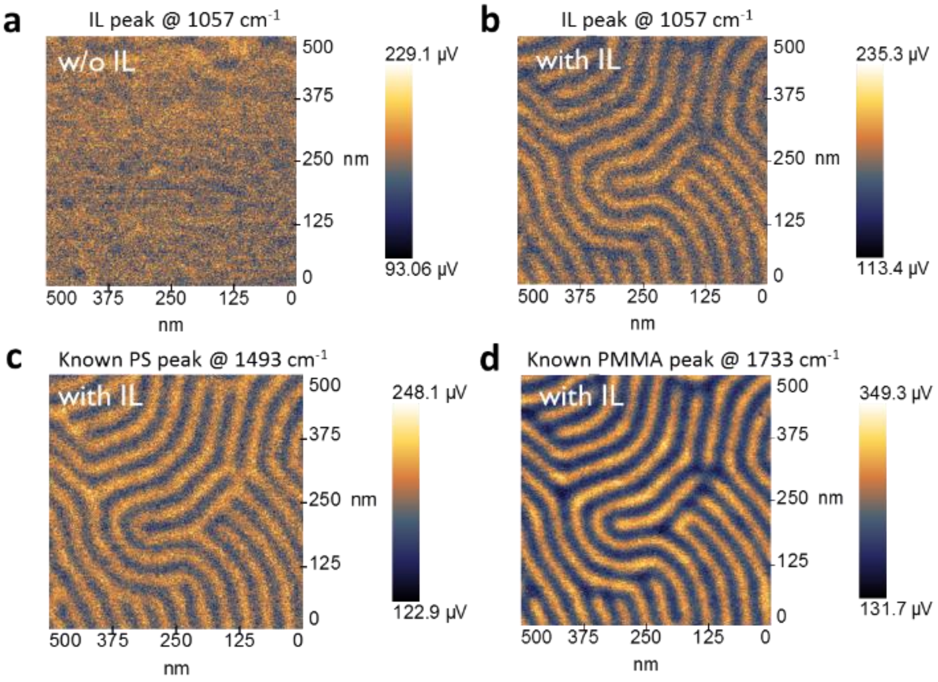

Figure 5.1. PiFM images of **a)** SM (39.5, 37) at 1057 cm^{-1}; **b)** SM (39.5, 37) and [BMPR][TFSI] blends at 1057 cm^{-1}; **c)** 1493 cm^{-1}; and **d)** 1733 cm^{-1}. Wavenumbers of 1057 cm^{-1}, 1493 cm^{-1} and 1733 cm^{-1} correspond to the adsorption peaks of IL, PS and PMMA respectively.

To explore the impact of ionic liquid additive on the block copolymer system, multilayers of the blends of PS-b-PMMA and [BMPR][TFSI] were characterized using resonant soft X-ray reflectivity (RSoXR). The real component of the complex refractive index, δ, was determined around the carbon and oxygen edges by reflectivity measurements. Then parallel-wetting samples of SM (22.9, 22.9) and [BMPR][TFSI] (ϕ_{IL} = 0 - 10 wt%) blends were prepared for RSoXR measurements on Si substrate with the film thickness targeted at ~ 5.5 L_0 ranging from 131 - 153 nm as a function of ϕ_{IL}. The lamellae morphology is maintained in all cases. Figure 5.2 presents the representative RSoXR results at carbon (280 eV) and oxygen (532 eV) edges for pristine SM (22.9, 22.9) and that blended with 4 - 10 wt% of [BMPR][TFSI]. With increasing [BMPR][TFSI] loading into PS-b-PMMA, more prominent multilayer fringes (black arrow in Figure 5.2) are observed at higher orders, which could be attributed to the narrower interfacial width. Besides, the position of multilayer peaks shifts to lower q range, thus indicating an increase in L_0 of the blends upon ionic liquid addition as literatures reported.[31] By modeling he depth profile of δ, the fitting (black line in Figure 5.2) reaches excellent agreement with the reflectivity data (red dots in Figure 5.2) and preludes several interesting results.

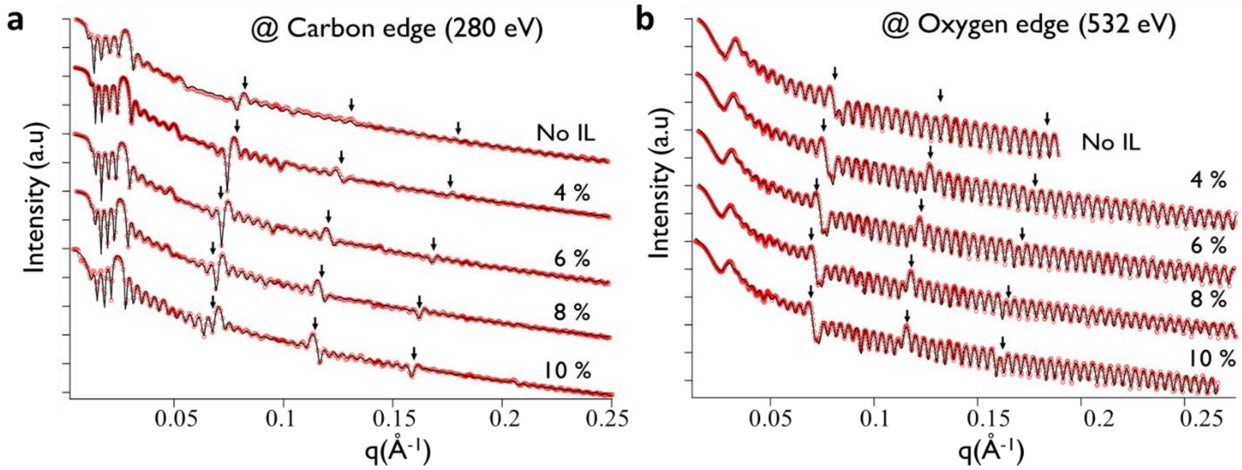

Figure 5.2. Representative RSoXR curves collected at the **a)** carbon edge (280 eV) and **b)** oxygen edge (532 eV) for SM (22.9, 22.9) and [BMPR][TFSI] blends as a function of IL loading ratio (in wt%).

Figure 5.3 shows the evolution of lamellae thickness of both domains and the interfacial width in between them upon the addition of [BMPR][TFSI]. In Figure 5.3a, the lamellae thickness of PS and IL-blended PMMA domains was normalized to that of pure SM (22.9, 22.9) and plotted as a function of ϕ_{IL}. The periodicity and the thickness of each domain are available in Table C.1. As

[BMPR][TFSI] is incorporated only into the PMMA domain, the PMMA layer thickness is increased by 22.5% at ϕ_{IL} = 10 wt% from its intrinsic value in pure SM (22.9, 22.9). However, the lamellae thickness of PS domain is also increased by 11% upon the addition of [BMPR][TFSI] at ϕ_{IL} = 8 wt% and then plateaus up to 10 wt%. Figure 5.3b presents the interfacial width (in red) for the blends of SM (22.9, 22.9) and [BMPR][TFSI]. It is measured as 4.8 nm at ϕ_{IL} = 0 wt%, which agrees with the reported value for PS-b-PMMA in literature,[32] and further reduces to 3.4 nm following a linear trendline with the addition of [BMPR][TFSI] up to 6 wt%. The reduction in interfacial width then slows down as it reaches 3.2 nm at ϕ_{IL} = 8 wt% and plateaus up to 10 wt%. As the calculation of interfacial width in the mean-field theory follows the following equations including the corrections for finite molecular mass:

$$\Delta = \Delta_0\left[1 + 1.34/(\chi N)^{1/3}\right], \ \Delta_0 = {}^{2a_{st}}\Big/_{\sqrt{6\chi}} \tag{1}$$

in which χ is the flory-huggins interaction parameter, N is the total degree of polymerization and a_{st} is the statistical segment length. Further considering the effect of thermal fluctuations of:

$$\langle \delta_x{}^2 \rangle = \frac{1}{2\pi\gamma_0} \ln\left(\frac{L_0}{\Delta_0}\right) \tag{2}$$

in which $\gamma_0 = \frac{a_{st}}{v}\left(\frac{\chi}{6}\right)^{1/2}$, representing the interfacial tension and v is the monomer volume. The apparent interfacial width, Δ^* could be further corrected from eq 1 as:

$$\Delta^* = \left[\Delta^2 + 2\pi\langle \delta_x{}^2 \rangle\right]^{1/2} \tag{3}$$

χ_{eff} could be back calculated from the interface width based on eq 1-3 and plotted as a function of ϕ_{IL} in Figure 5.3b. Accordingly, the addition of 8 wt% [BMPR][TFSI] into SM (22.9, 22.9) increases χ_{eff} from 0.037 to 0.106 and doesn't change upon further IL addition. Note that here the calculated χ_{eff} values are approximations by assuming that the system is in strong segregation regime where $\chi N >> 10.5$ and eq 1 is validated, while the pristine SM (22.9, 22.9) is in intermediate segregation regime ($\chi N \sim 16.2$ at 200°C).

As the addition of ionic liquid increases and the segregation strength of the entire system, both PS and PMMA chains tend to stretch away from the interface to minimize unfavorable contacts, thus reducing the interfacial width. It is apparent from Figure 5.3 that such chain stretch and thus the reduction in interfacial width are more drastic at low ϕ_{IL} (0 ~ 6 wt%) and reach a saturation limit upon further loading ($\phi_{\mathrm{IL}} \geq 8$ wt%), after which the ionic liquid simply swells the PMMA domain (Figure 5.3a) without changing the interfacial properties. This nonlinear dependence of segregation strength may account for the stronger dependence of L_0 on ϕ_{IL} of the same blends that we previously reported in Chapter 4 at the low ϕ_{IL} regime compared with other studies that span over a much wider range. This also poses a limit of ϕ_{IL}, below which ionic liquid can be efficiently used to increase χ_{eff} and scale down the resolution limit of block copolymer self-assembly.

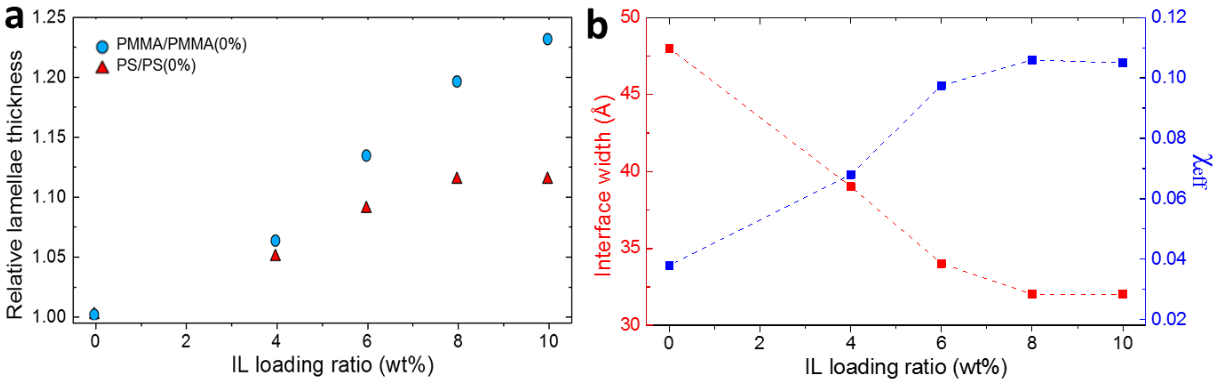

Figure 5.3. a) Relative lamellae thickness of PS and PMMA domains in SM (22.9, 22.9) and [BMPR][TFSI] blends normalized to that in pure SM (22.9, 22.9); **b)** Interfacial width and χ_{eff} as a function of IL loading ratio (in wt%).

Having revealed the increase in segregation strength and the reduction in interface width in between two component blocks with the addition of ionic liquid, we move towards the fabrication end to investigate its impact on the line roughness after selective removal of one block by comparing DSA of PS-b-PMMA without and with [BMPR][TFSI]. Two pure block copolymer systems, SM (22.9, 22.9) and SM (30.4, 27.4), as well as the blends of SM (22.9, 22.9) and [BMPR][TFSI] (ϕ_{IL} = 8 wt%) were used here with the L_0 and χN as listed in Table C.2. These three material systems were successfully assembled on chemical patterns with optimum conditions (Table C.2), followed by subsequent dry etch step to completely remove the PMMA (or PMMA/IL) domain. Multiple rectangular scans as represented in Figure 5.4a were taken by high-resolution CDSEM for the power spectral density (PSD) roughness analysis as shown in Figure 5.4b to characterize the post-etch line edge roughness ($3\sigma_{\mathrm{LER}}$) in different range of the frequency spectrum. As the area under PSD curve is proportional to σ_{LER}^2 based on Parseval theorem, $3\sigma_{\mathrm{LER}}$ = 2.88 nm for SM (22.9, 22.9), which is slightly reduced to 2.76 nm for SM (30.4, 27.4) with a higher N value and 2.67 nm with the addition of [BMPR][TFSI] and thus a higher χ_{eff}. Most of the reductions come from the low to medium frequency range. The inlet of Figure 5.4b plots $3\sigma_{\mathrm{LER}}$ and $3\sigma_{\mathrm{LER}}/L_0$ as a function of χN for these three systems. The addition of [BMPR][TFSI], while increasing the χ_{eff} of PS-b-PMMA by 61.7%, reduces the post-etch LER by 7.3% in $3\sigma_{\mathrm{LER}}$ and 16.4% in $3\sigma_{\mathrm{LER}}/L_0$ (from A to C).

The PSD roughness analysis reveals that χ increase upon the addition of ionic liquid results in insignificant LER reduction in the medium-frequency range of our interest after PMMA removal ($\Delta 3\sigma_{\mathrm{LER}}$ ~ 0.2 nm), especially when compared to that in the interfacial width (1.5 - 2 nm). Simulation showed that increased segregation strength resulted in decreased LER and LWR within a narrow frequency range at $1/L_0$.[33] While such difference in the BCP state may not be fully translated through the dry etch step, it is the line roughness after selective removal of one block and pattern transfer that determines the device performance.[34] Post-etch LER and LWR were reported smaller for high-χ polymer compared to PS-b-PMMA.[21] However, it is arguable to attribute the roughness reduction simply to the higher χ value. As for many existing high-χ systems that adopt different chemistry, it is challenging to deconvolute χ increase with other factors, such as enhanced etch contrast, in the contribution to roughness healing. In our case, we assume that the PS-b-PMMA without and with IL additive have similar etching properties considering the low ϕ_{IL}, thus the impact of χ increase is reasonably delineated. Note that the variations in pre-patterns, such as the pitch size, may contribute to the LER difference. For example, SM (30.4, 27.4) and SM (22.9, 22.9)/[BMPR][TFSI] blends assembled on the chemical patterns of L_S = 84 and 82 nm respectively (~ $3L_0$) have similar PSD curves (in blue and red), while that of SM (22.9, 22.9) is more deviated, which is assembled on L_S = 98 nm (~ $4L_0$) due to the insufficient resolution of 193 nm immersion lithography to produce patterns of L_S = 74 nm (~ $3L_0$).

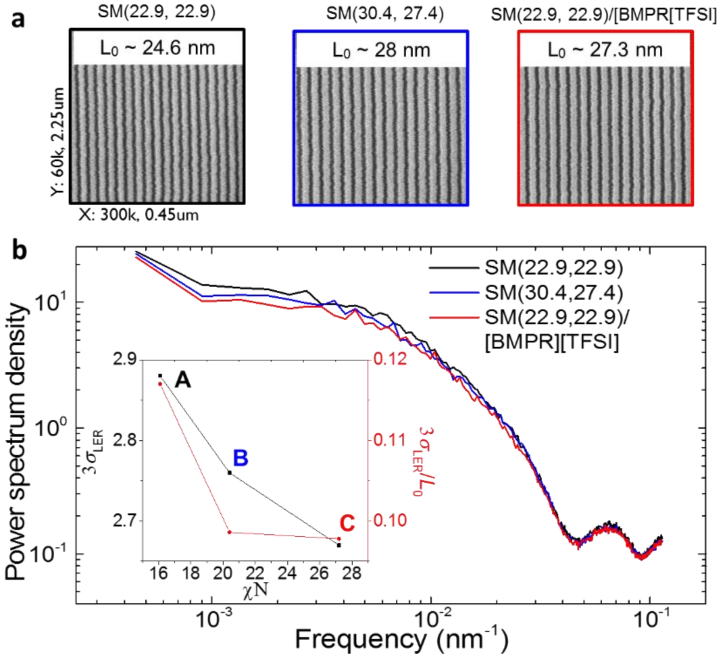

Figure 5.4. a) Top-down SEM images in rectangular scan (0.45 um by 2.25 um area) of directed self-assembly of SM (22.9, 22.9), SM (30.4, 27.4) and SM (22.9, 22.9)/[BMPR][TFSI] blends; and **b)** corresponding PSD curves. Inlet shows the $3\sigma_{LER}$ and normalized $3\sigma_{LER}$ (to L_0) as a function of the calculated χN value for the above three materials. 50 rectangular scans were analyzed for the PSD results. PMMA domains were removed for the measurements of line roughness.

We further investigate the impact of χ increase by ionic liquid addition on the assembly kinetics. To compare the DSA of pure PS-b-PMMA and PS-b-PMMA/IL blends, SM (30.4, 27.4) with $L_0 \approx 28$ nm and SM (22.9, 22.9)/[BMPR][TFSI] blends with $L_0 \approx 27.3$ nm were assembled on chemical patterns of $L_S \approx 84$ nm and 82 nm, respectively. While the L_0 and density multiplication factor were close in both cases, the blends system has a χN value 33% higher than that of the pure block copolymer mainly owing to the [BMPR][TFSI] additive. Figure 5.5 shows the evolution of directed assembly upon thermal annealing at 215°C, and it is evident that the addition of ionic liquid slows the kinetics of DSA. As the pitch and width of guiding stripes are optimized based on the L_0, no effect of additional chain compression and stretching is included. The kinetcis of assembly may be impacted by the following two contradictive factors. On the one hand, the addition of ionic liquid into block copolymer, as a plasticizer, increases the chain mobility within PMMA domains. On the other hand, ionic liquid additive leads to the increase in χ, and thus an exponential decrease in the chain mobility across domains[26] and an increase in free energy barrier to defect annilation,[25] both contributing to a slower kinetics of assembly. Considering that the defect annihilation of the lamellar system here requires the inter-domain molecule diffusion, the former factor may exert limited impact while the latter one of χ increase plays a dorminant role in the resulting slower kinetics. In other cases of block copolymers with different morphology and molecular weight, for example in cylindrical systems, the intra-domain diffusions parallel along and rotating around the interface without domain traversal also contribute to the grain realignment so that it is the interplay of both the above two factors that determine the impact of ionic liquid additve on the assembly kinetics.

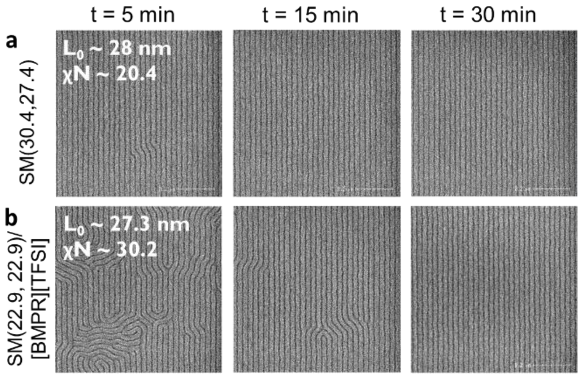

Figure 5.5. Top-down SEM images of 3X density multiplication assembly of **a)** SM(30.4, 27.4) on chemical pattern of L_S = 84 nm (~ $3L_0$), and **b)** SM(22.9, 22.9) and [BMPR][TFSI] blends on chemical pattern of L_S = 82 nm (~ $3L_0$) as a function of annealing time at 215C°.

5.5 Conclusion

We enhance the segregation strength of PS-b-PMMA block copolymer by blending in relatively low volume ratio of IL additive and investigate the impact of χ increase on the polymer system and its directed self-assembly. It is shown by RSoXR measurements that the addition of 8 wt% of IL significantly stretches the PS and PMMA chains away from the interface and narrows the interfacial width in between from 4.8 nm to 3.2 nm to alleviate the unfavorable contacts at the lamellae interface. We further study the impact of χ increase on the LER and assembly kinetics by comparing the DSA of PS-b-PMMA without and with IL. The LER analysis is performed after etching away the PMMA domains. Unlike the significant reduction in interfacial width and presumably less positional fluctuation at the intermixing region, negligible improvement in LER (~0.2 nm in 3σ) is observed. Here the impact of χ is delineated from other factors, like different chemistry of component blocks, by assuming that the pure and blending systems have the same etch properties owing to the low volume ratio of ionic liquid. It is therefore indicated that the reduction in LER reported in other high-χ materials might not be simply attributed the χ increase.

Meanwhile, the assembly kinetics towards the defect-free state is slower as seen in the blends compared to pure PS-b-PMMA at the same dimension, which is a result of smaller interdiffusivity and higher energy barriers for defect annihilation.

5.6 References

(1) Kim, S. O.; Solak, H. H.; Stoykovich, M. P.; Ferrier, N. J.; Pablo, J. J. De; Nealey, P. F. *Nature* **2003**, *424*, 411–414.

(2) Ruiz, R.; Kang, H.; Detcheverry, F. a; Dobisz, E.; Kercher, D. S.; Albrecht, T. R.; de Pablo, J. J.; Nealey, P. F. *Science.* **2008**, *321* (5891), 936–939.

(3) Bita, I.; Yang, J. K. W.; Jung, Y. S.; Ross, C. a; Thomas, E. L.; Berggren, K. K. *Science* . **2008**, *321* (5891), 939–943.

(4) Mansky, P.; Liu, Y.; Huang, E.; Russell, T. P.; Hawker, C. *Science* . **1997**, *275*, 1458–1460.

(5) Ruiz, R.; Dobisz, E.; Albrecht, T. R. *ACS Nano* **2011**, *5* (1), 79–84.

(6) Wan, L.; Ruiz, R.; Gao, H.; Patel, K. C.; Albrecht, T. R.; Yin, J.; Kim, J.; Cao, Y.; Lin, G. **2012**, *20* (3), 5–6.

(7) Yoshida, H.; Suh, H. S.; Ramírez-hernández, A.; Lee, J. I.; Aida, K. **2013**, *C*, 55–58.

(8) Bates, C. M.; Seshimo, T.; Maher, M. J.; Durand, W. J.; Cushen, J. D.; Dean, L. M.; Blachut, G.; Ellison, C. J.; Willson, C. G. *Science* . **2012**, *338* (6108), 775–779.

(9) Zhang, J.; Clark, M. B.; Wu, C.; Li, M.; Trefonas, P.; Hustad, P. D. *Nano Lett.* **2016**, *16* (1), 728–735.

(10) Suh, H. S.; Kim, D. H.; Moni, P.; Xiong, S.; Ocola, L. E.; Zaluzec, N. J.; Gleason, K. K.; Nealey, P. F. *Nat. Nanotechnol.* **2017**.

(11) Sinturel, C.; Ne Vayer, M.; Morris, M.; Hillmyer, M. A. *Macrmolecules* **2013**, *46*, 5399–5415.

(12) Gotrik, K. W.; Hannon, A. F.; Son, J. G.; Keller, B.; Alexander-Katz, A.; Ross, C. A. *ACS Nano* **2012**, *6* (9), 8052–8059.

(13) Xiong, S.; Wan, L.; Ishida, Y.; Chapuis, Y. A.; Craig, G. S. W.; Ruiz, R.; Nealey, P. F. *ACS Nano* **2016**, *10* (8), 7855–7865.

(14) Kim, S.; Nealey, P. F.; Bates, F. S. *Nano Lett.* **2014**, *14*, 148–152.

(15) Kim, S.; Nealey, P. F.; Bates, F. S. *ACS Macro Lett.* **2012**, *1* (1), 11–14.

(16) Yang, G.-W.; Wu, G.-P.; Chen, X.; Xiong, S.; Arges, C. G.; Ji, S.; Nealey, P. F.; Lu, X.-B.; Darensbourg, D. J.; Xu, Z.-K. *Nano Lett.* **2017**, *17* (2), 1233–1239.

(17) Bosse, A. W. *J. Vac. Sci. Technol. B, Nanotechnol. Microelectron. Mater. Process. Meas. Phenom.* **2011**, *29* (6), 06F202.

(18) Patrone, P. N.; Gallatin, G. M. *Macromolecules* **2012**, *45* (23), 9507–9516.

(19) Helfand, E.; Tagami, Y. *J. Polym. Sci. Part B Polym. Lett.* **1971**, *9* (10), 741–746.

(20) Semenov, A. N. *Macromolecules* **1993**, *26*, 6617–6621.

(21) Tsai, H.; Miyazoe, H.; Vora, A.; Magbitang, T.; Arellano, N.; Liu, C.-C.; Maher, M. J.; Durand, W. J.; Dawes, S. J.; Bucchignano, J. J.; Gignac, L.; Sanders, D. P.; Joseph, E. A.; Colburn, M. E.; Willson, C. G.; Ellison, C. J.; Guillorn, M. A. In *Proc. SPIE*; 2016; p 977910.

(22) Kim, J. M.; Hur, Y. H.; Jeong, J. W.; Nam, T. W.; Lee, J. H.; Jeon, K.; Kim, Y.; Jung, Y. S. *Chem. Mater.* **2016**, *28* (16), 5680–5688.

(23) Gabor, A.; Lehner, E.; Mao, G.; Schneggenburger, L.; Ober, C. K. *Chem. Mater.* **1994**, *6* (16), 927–934.

(24) Nagpal, U.; Mu, M.; Nealey, P. F.; Pablo, J. J. De. *ACS Macro Lett.* **2012**, *1*, 418–422.

(25) Hur, S.-M.; Thapar, V.; Ramírez-Hernández, A.; Khaira, G.; Segal-Peretz, T.; Rincon-Delgadillo, P. A.; Li, W.; Müller, M.; Nealey, P. F.; de Pablo, J. J. *Proc. Natl. Acad. Sci.* **2015**, *112* (46), 14144–14149.

(26) Lodge, T. P.; Dalvi, M. C. *Phys. Rev. Lett.* **1995**, *75* (4), 657–660.

(27) Liu, C. C.; Han, E.; Onses, M. S.; Thode, C. J.; Ji, S.; Gopalan, P.; Nealey, P. F. *Macromolecules* **2011**, *44* (7), 1876–1885.

(28) Delgadillo, P. A. R.; Gronheid, R.; Thode, C. J.; Wu, H.; Cao, Y.; Neisser, M.; Somervell, M.; Nafus, K.; Nealey, P. F. *J. Micro/Nanolithography, MEMS, MOEMS* **2012**, *11* (3), 31302.

(29) Underwood, J. .; Gullikson, E. . *J. Electron Spectros. Relat. Phenomena* **1998**, *92* (1–3), 265–272.

(30) Nowak, D.; Morrison, W.; Wickramasinghe, H. K.; Jahng, J.; Potma, E.; Wan, L.; Ruiz, R.; Albrecht, T. R.; Schmidt, K.; Frommer, J.; Sanders, D. P.; Park, S. *Sci. Adv.* **2016**, *2* (3), e1501571–e1501571.

(31) Simone, P. M.; Lodge, T. P. *Macromolecules* **2008**, *41* (5), 1753–1759.

(32) Anastasiadis, S. H.; Russell, T. P.; Satija, S. K.; Majkrzak, C. F. *J. Chem. Phys.* **1990**, *92* (9), 5677–5691.

(33) Bosse, A. W. *J. Vac. Sci. Technol. B Microelectron. Nanom. Struct.* **2011**, *29* (3), 31803.

(34) Baravelli, E.; Dixit, A.; Rooyackers, R.; Jurczak, M.; Speciale, N.; De Meyer, K. *IEEE Trans. Electron Devices* **2007**, *54* (9), 2466–2474.

Appendix A

Supplemental information for Chapter 3

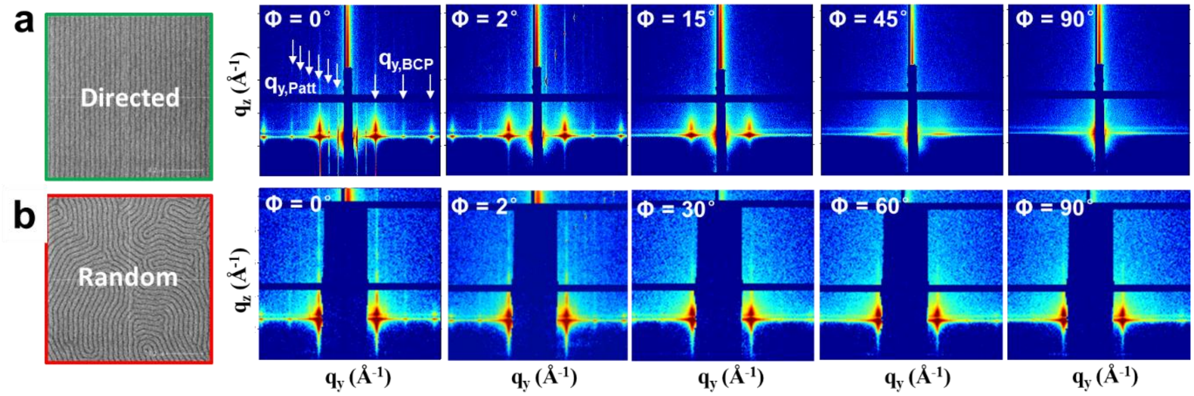

Figure A.1. 2D GISAXS patterns of 35 nm thin film of PS-b-PMMA (L_0 = 28 nm) upon sample rotation from ϕ = 0° to 90°. **a)** Directed and **b)** random assembly were achieved on W=0.77 L_0 and 1.19 L_0 respectively. In both cases, the chemical pattern had a pitch of L_S = 84 nm, and the samples were annealed at 250°C for 5 min in nitrogen.

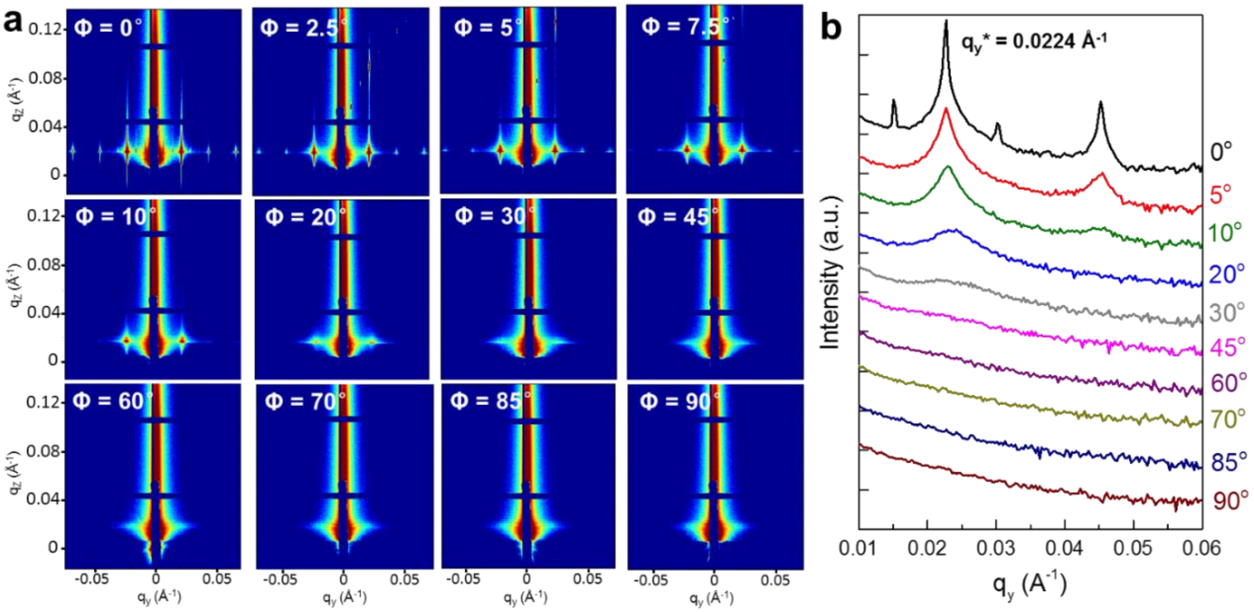

Figure A.2. a) 2D GISAXS patterns and **b)** the scattering line profiles of Intensity vs. q_y at q_z = 0.01674 Å^{-1} with increasing rotational angles, ϕ, of the 144 nm thick PS-b-PMMA film at the incident angle of 0.1°. The sample was annealing at 250°C for 1.5 h in nitrogen. The Bragg peak of q_y^* corresponds to the natural period of PS-b-PMMA.

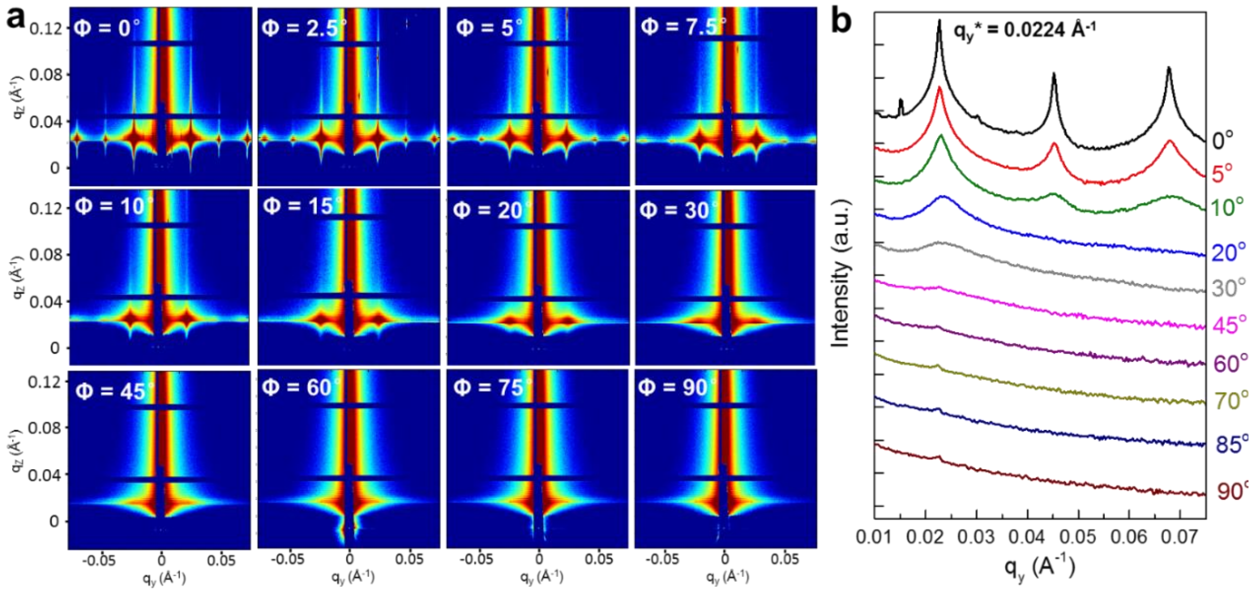

Figure A.3. a) 2D GISAXS patterns and **b)** the scattering line profiles of Intensity vs. q_y at q_z = 0.02276 Å^{-1} with increasing rotational angles, ϕ, of the 144 nm thick PS-b-PMMA film at the incident angle of 0.178°. The sample was annealing at 250°C for 1.5 h in nitrogen. The Bragg peak of q_y^* corresponds to the natural period of PS-b-PMMA

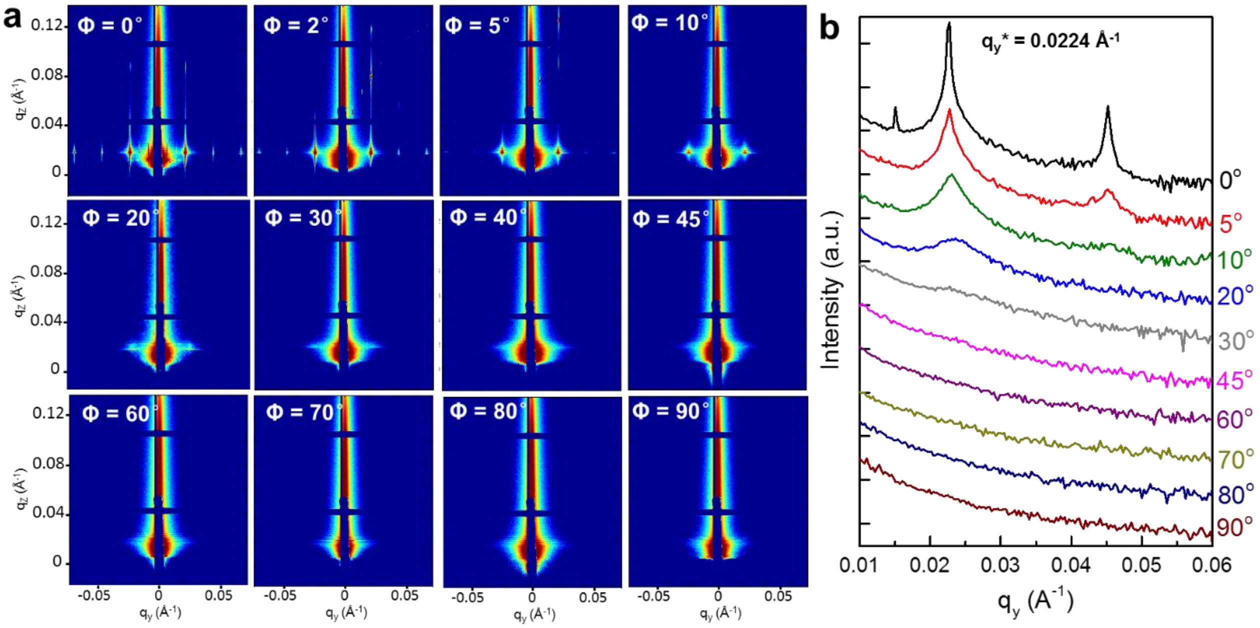

Figure A.4. a) 2D GISAXS patterns and **b)** the scattering line profiles of Intensity vs. q_y at q_z = 0.01755 Å^{-1} with increasing rotational angles, ϕ, of the 144 nm thick PS-b-PMMA film at the incident angle of 0.1°. The sample was annealing at 250°C for 3 h in nitrogen. The Bragg peak of q_y^* corresponds to the natural period of PS-b-PMMA.

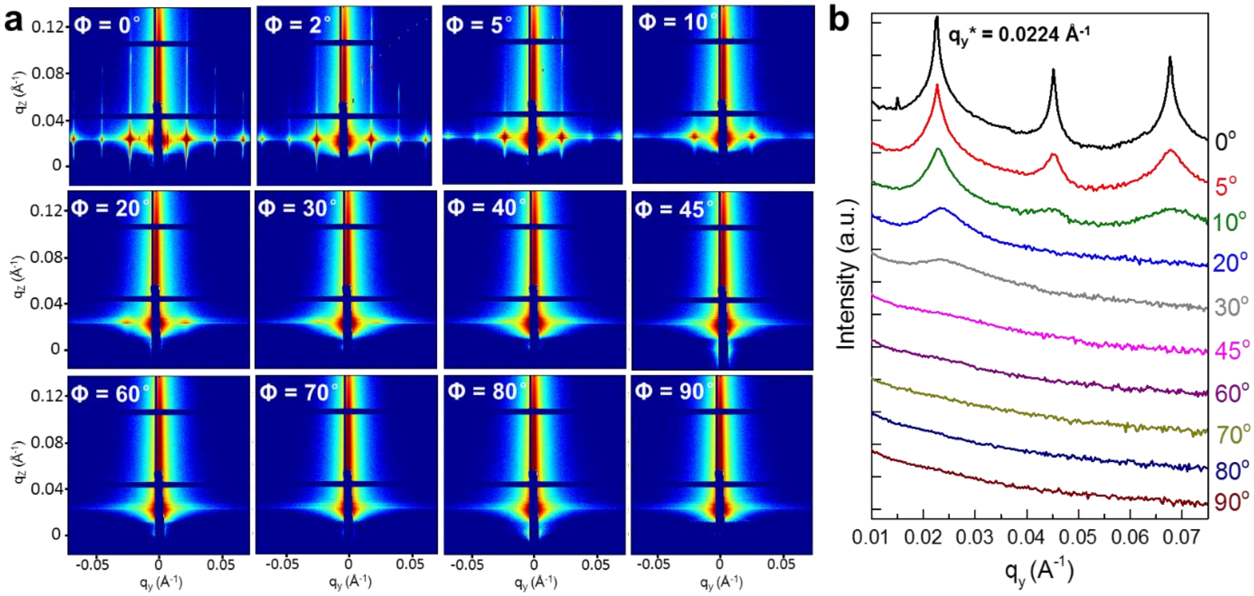

Figure A.5. a) 2D GISAXS patterns and **b)** the scattering line profiles of Intensity vs. q_y at q_z = 0.02286 Å^{-1} with increasing rotational angles, ϕ, of the 144 nm thick PS-b-PMMA film at the incident angle of 0.177°. The sample was annealing at 250°C for 3 h in nitrogen. The Bragg peak of q_y^* corresponds to the natural period of PS-b-PMMA.

Appendix B

Supplemental information for Chapter 4

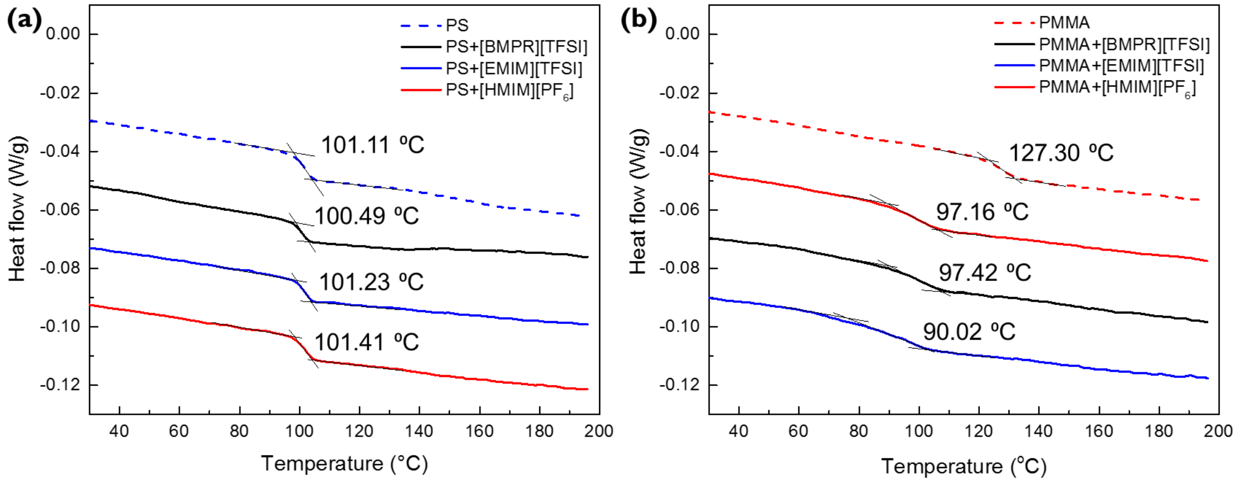

Figure B.1. Differential Scanning Calorimetry (DSC) scans of **a)** PS homopolymer and **b)** PMMA homopolymer before and after blending with ionic liquids (20 wt%) of [BMPR][TFSI], [EMIM][TFSI] and [HMIM][PF_6] respectively. Scans are offset vertically for clarity.

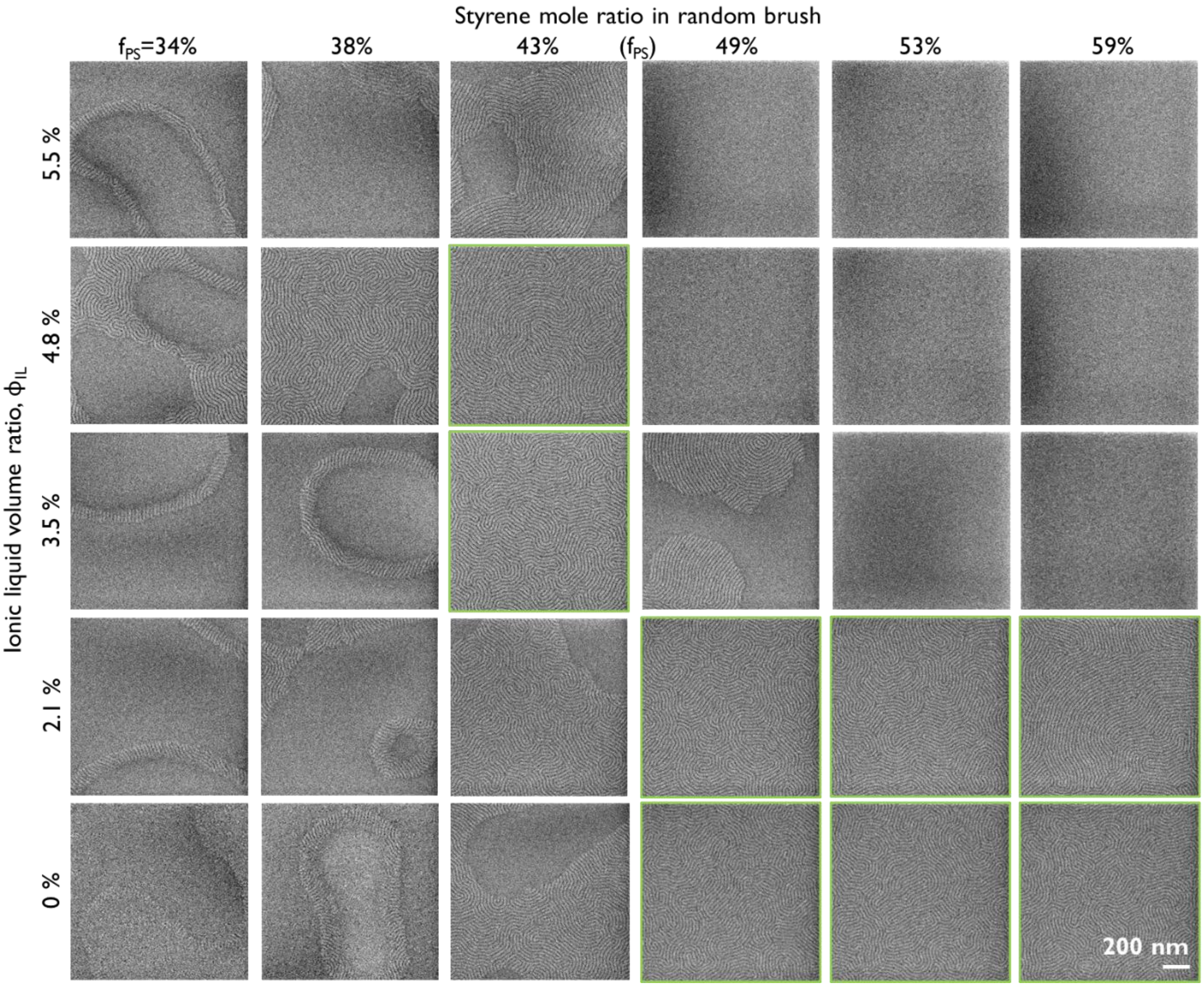

Figure B.2. Top-down SEM images of SM(22.9, 22.9) and [EMIM][TFSI] blends as a function of IL volume ratios, ϕ_{IL}, and PS-r-PMMA random brush compositions, f_{PS} (styrene ratio in mol%).

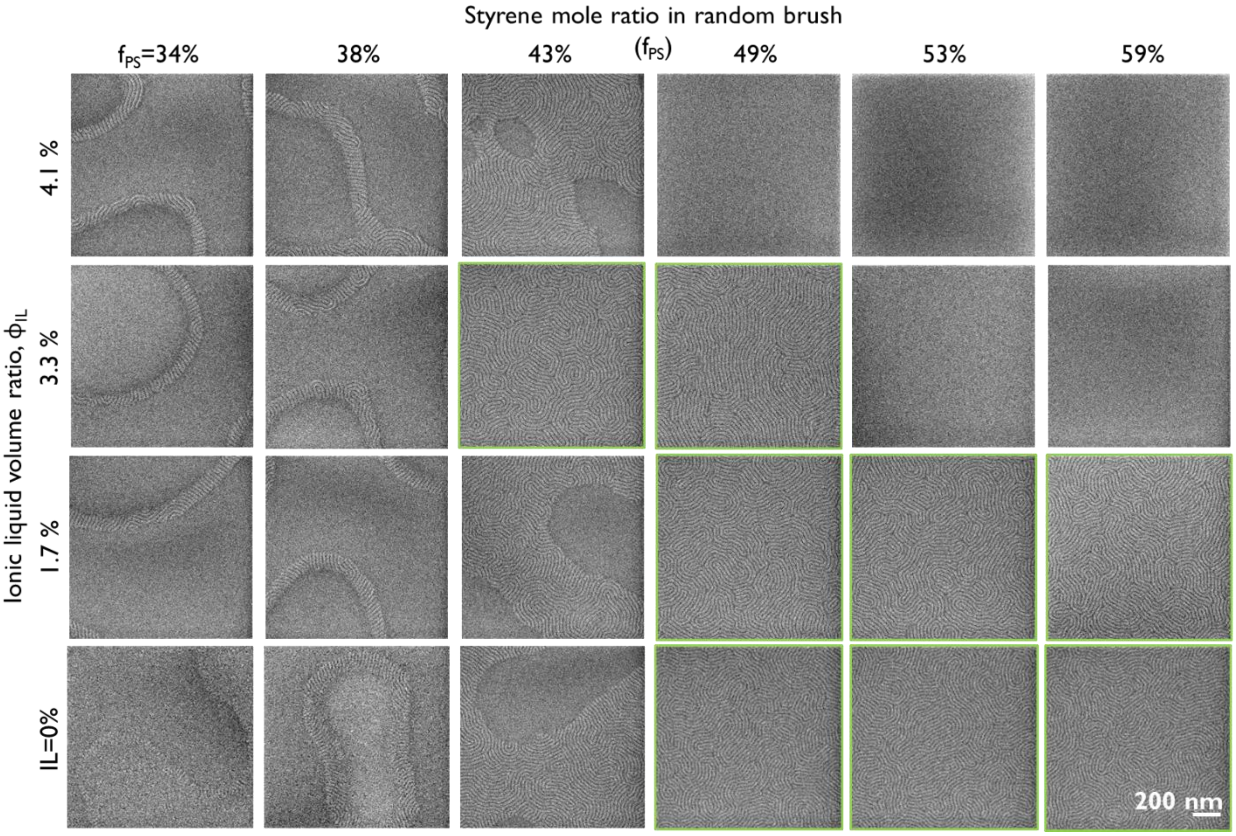

Figure B.3. Top-down SEM images of SM(22.9, 22.9) and [HMIM][PF_6] blends as a function of IL volume ratios, ϕ_{IL}, and PS-r-PMMA random brush compositions, f_{PS} (styrene ratio in mol%).

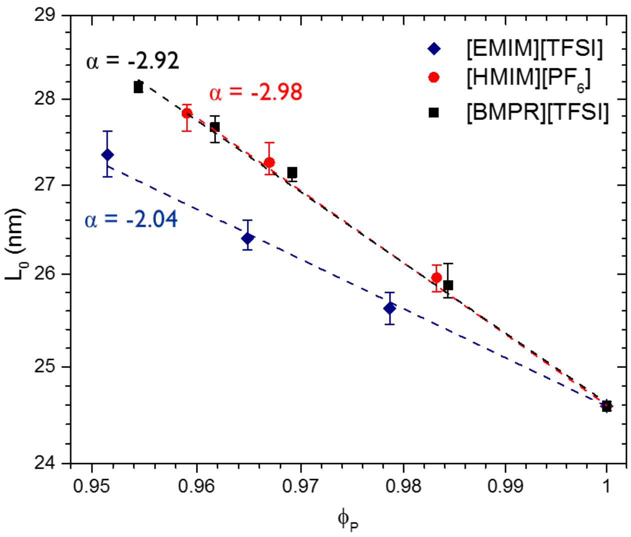

Figure B.4. L_0 of SM (22.9, 22.9) and [BMPR][TFSI] blends plotted as a function of block polymer volume fraction, ϕ_P.

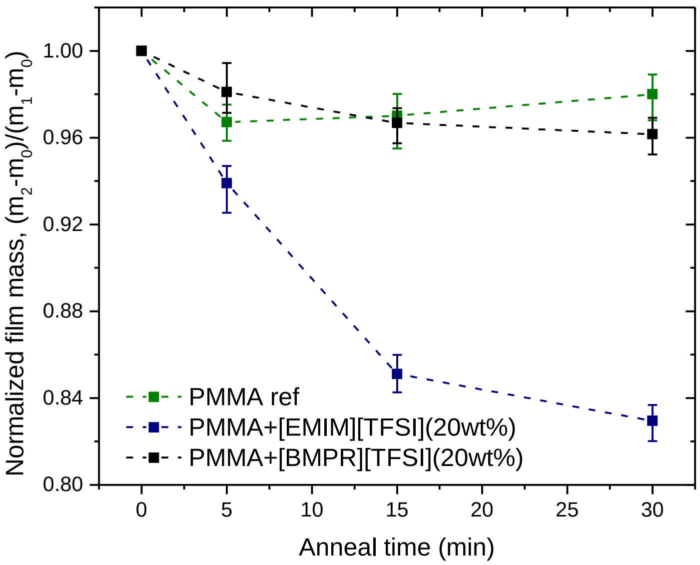

Figure B.5. Normalized mass of PMMA films spin coated on 300 mm Si wafer with no ionic liquid (black), [EMIM][TFSI] (blue) and [BMPR][TFSI] (red) as a function of annealing time. For each 300 mm wafer, the mass was measured for bare wafer (m_0), after spin coating (m_1) and after thermal annealing (m_2). Then the mass of polymer film after annealing ($m_2 - m_0$) was normalized to that after coating ($m_1 - m_0$). All samples were annealed under 215℃° in nitrogen atmosphere.

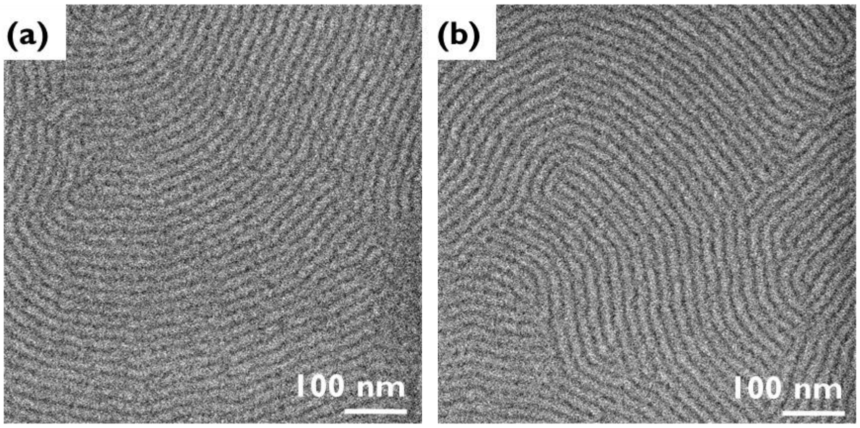

Figure B.6. Top-down SEM images of SM(14.3,13.7) self-assembled into a) lamellas of 19.2 nm with 2.1 vol% [EMIM][TFSI] addition; b) lamellas of 19.4 nm with 1.5 vol% [HMIM][PF6] addition. Sample a and b were annealed at 190°C and 200°C respectively for 5 min.

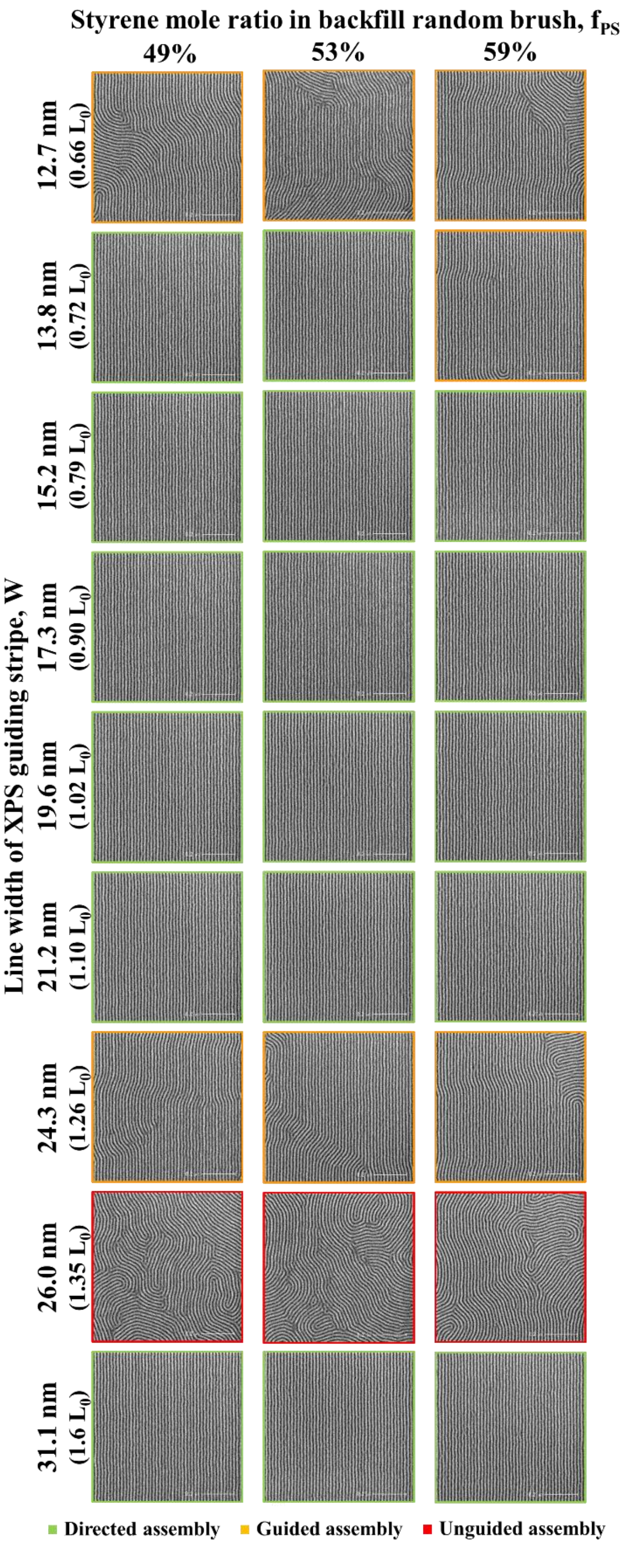

Figure B.7. Top-down SEM images of SM (14.3, 13.7) and [BMPR][TFSI] blends (L_0 ~ 19.3 nm) assembled over a range of XPS guiding widths and backfill brush compositions on line space chemical patterns with 78 nm pitch ($L_S \approx 4\ L_0$). All samples were annealed for 5 min at 200°C in nitrogen.

For PS-b-PMMA, The Flory-Huggins interaction parameter, χ, has the following temperature dependence

$$\chi = 0.028 + \frac{3.9}{T} \quad (1)$$

where T is the absolute temperature. In this study, PS-b-PMMA of three different molecular weights were used, and the blends of each PS-b-PMMA and IL were annealed at different temperatures, which gives slight difference in χ as calculated in Table B.1 below. The χN values calculated here again confirms that SM (14.3, 13.7) and SM (10.3, 9.5) are both in disordered state.

Table B.1. χ, N and χN calculated for PS-b-PMMA used in the study of different molecular weight at corresponding annealing temperature

PS-b-PMMA	**Temperature (°C）**	$\chi_{\text{PS-PMMA}}$	N	χN
SM (22.9, 22.9)	200	0.0362	447.619	16.2
SM (14.3, 13.7)	200	0.0362	274.136	9.9
SM (10.3, 9.5)	125	0.0378	193.781	7.3

As known from Figure 4.4a, IL addition increases the L_0 while strengthening the block interaction of symmetric diblock copolymer in that:

$$L_0 \propto \chi^{\frac{1}{6}} N^{\frac{2}{3}} \quad (2)$$

If the χ value of the blends of BCP and IL is doubled upon IL addition, N could be halved to maintain phase separation with a smaller minimum periodicity, which is 0.7 times that of pure BCP:

$$L_0' \propto (2\chi)^{\frac{1}{6}}\left(\frac{1}{2}N\right)^{\frac{2}{3}} = 0.707\,\chi^{\frac{1}{6}} N^{\frac{2}{3}} \quad (3)$$

By lowering the molecular weight of PS-b-PMMA and increasing the loading ratio of IL in the meantime, we can scale down the periodicity of the resulting blends. We blended PS-b-PMMA of three molecular weights with [BMPR][TFSI] at varying volume ratios, all of which have increasing L_0 as shown in Figure B.8. Considering the scaling relationship of L_0 (eq 2) and the increase in N_{eff} due to the swollen volume of IL ($\phi_{\mathrm{IL}} < 5$ vol%) in PMMA domain, χ_{eff} can be easily calculated from the following equation knowing $\chi_{\mathrm{PS\text{-}PMMA}}$ and the L_0 value before and after adding IL:

$$\chi_{\mathrm{eff}} = \chi_{\mathrm{PS\text{-}PMMA}} \times \left(\frac{L_{0,\phi_{\mathrm{IL}}}}{L_0}\right)^6 \times \left(\frac{N}{N_{\mathrm{eff}}}\right)^4 \tag{4}$$

where L_0 is the intrinsic periodicity of PS-b-PMMA, and $L_{0,\phi_{\mathrm{IL}}}$ is that of PS-b-PMMA and [BMPR][TFSI] blends at the volume ratio of ϕ_{IL}. χ_{eff} of SM (22.9, 22.9) and [BMPR][TFSI] blends plotted in Figure 4.4b were calculated from eq 4 using its intrinsic L_0 of 24.6 nm. On the other hand, "L_0", the intercept where L_0 is extrapolated back to $\phi_{\mathrm{IL}} = 0$ (fitted line in Figure B.8), is defined as the pseudo-periodicity of disordered SM (14.3, 13.7) and SM (10.3, 9.5) if microphase separation could have occurred, which is 18.2 nm and 15.0 nm respectively. IL addition enabled the disordered to ordered transition of SM(14.3, 13.7) and SM(10.3, 9.5) to form lamellas of 19.3 nm and 16.5 nm as shown in Figure 4.6 and Figure 4.9. Based on eq 4 using $\chi_{\mathrm{PS\text{-}PMMA}}$ and N values in Table B.1, $(\chi N)_{\mathrm{eff}}$ of the corresponding blends of disordered PS-b-PMMA and [BMPR][TFSI] is calculated and summarized in Table B.2, both of which are above the critical value of 10.5 and thus in phase separated regime.

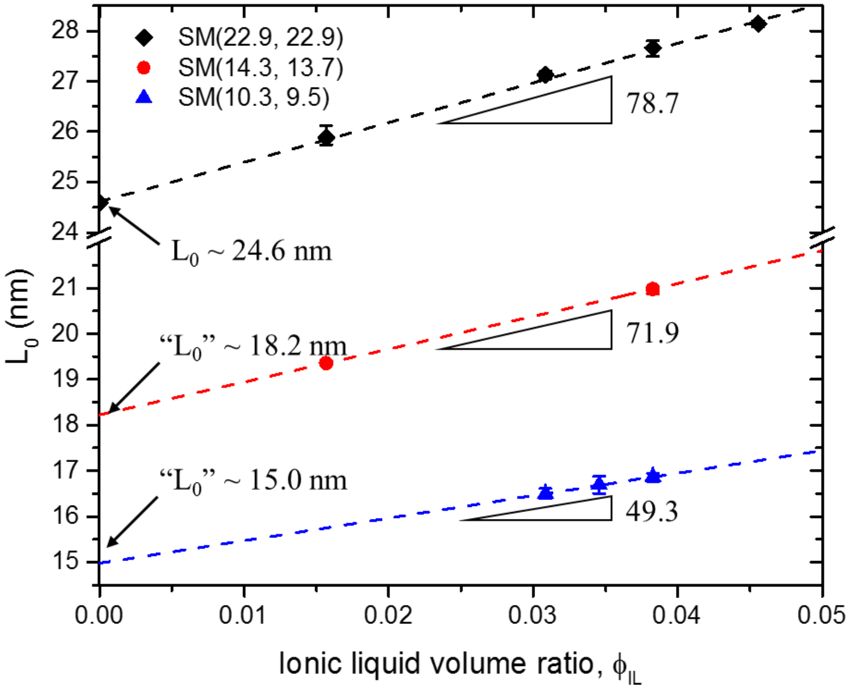

Figure B.8. L_0 of PS-b-PMMA and [BMPR][TFSI] blends plotted as a function of ionic liquid volume fraction, ϕ_{IL}.

Table B.2. χ_{eff} and $(\chi N)_{eff}$ calculated for the blends of disordered PS-b-PMMA and [BMPR][TFSI]

PS-b-PMMA	**IL volume ratio, ϕ_{IL}**	$L_{0,\phi_{IL}}$ **(nm)**	χ_{eff}	$(\chi N)_{eff}$
SM (14.3, 13.7)	1.6%	19.3	0.0512	13.4
SM (10.3, 9.5)	3.1%	16.5	0.0674	11.7

Appendix C

Supplemental information for Chapter 5

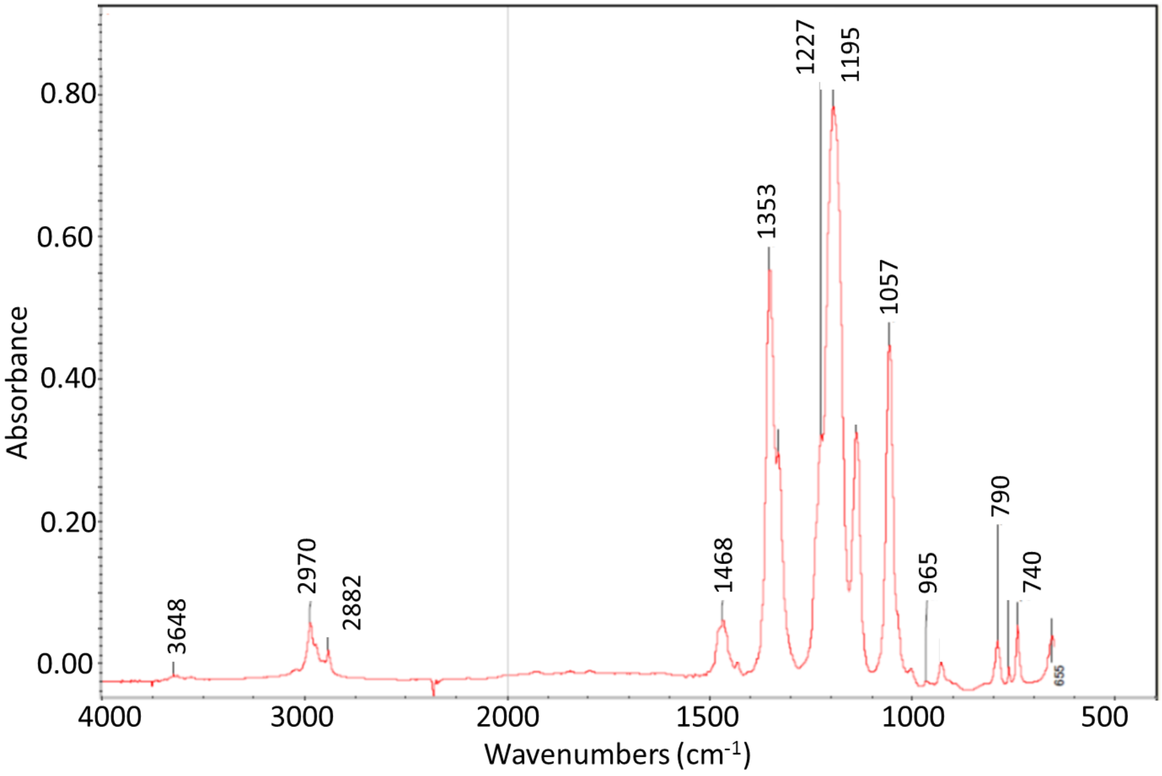

Figure C.1. FTIR spectra of [BMPR][TFSI]

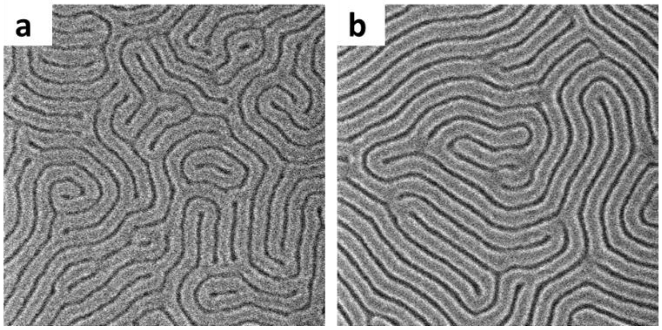

Figure C.2. Top-down SEM images of a) SM (39.5, 37) with a thickness of ~ 34 nm; and b) the blends of SM (39.5, 37) and 7.4 vol% [BMPR][TFSI] with a thickness of ~ 40 nm. Both samples were annealed at 250°C for 5 min.

Table C.1. Summary of average layer thickness and periodicity of RSoXR measurements

m(IL)/m(BCP)	PS thickness (nm)	PMMA thickness (nm)	L_0 (nm)
0	12.3	11.2	23.5
0.04	12.9	11.9	24.8
0.06	13.4	12.7	26.1
0.08	13.7	13.4	27.1
0.10	13.7	13.8	27.5

Table C.2. List of samples for LER analysis and the characterization of each material

Sample	Materials	χN @ 215°C	L_0 (nm)	W (nm)	L_S (nm)
A	SM(22.9, 22.9)	16.1	24.6	18.2 (~ 0.74 L_0)	98 (~ 4 L_0)
B	SM(30.4, 27.4)	20.4	28	20.5 (~ 0.75 L_0)	84 (~ 3 L_0)
C	SM(22.9, 22.9) + [BMPR][TFSI]	27.2	27.3	20.5 (~ 0.73 L_0)	82 (~ 3 L_0)